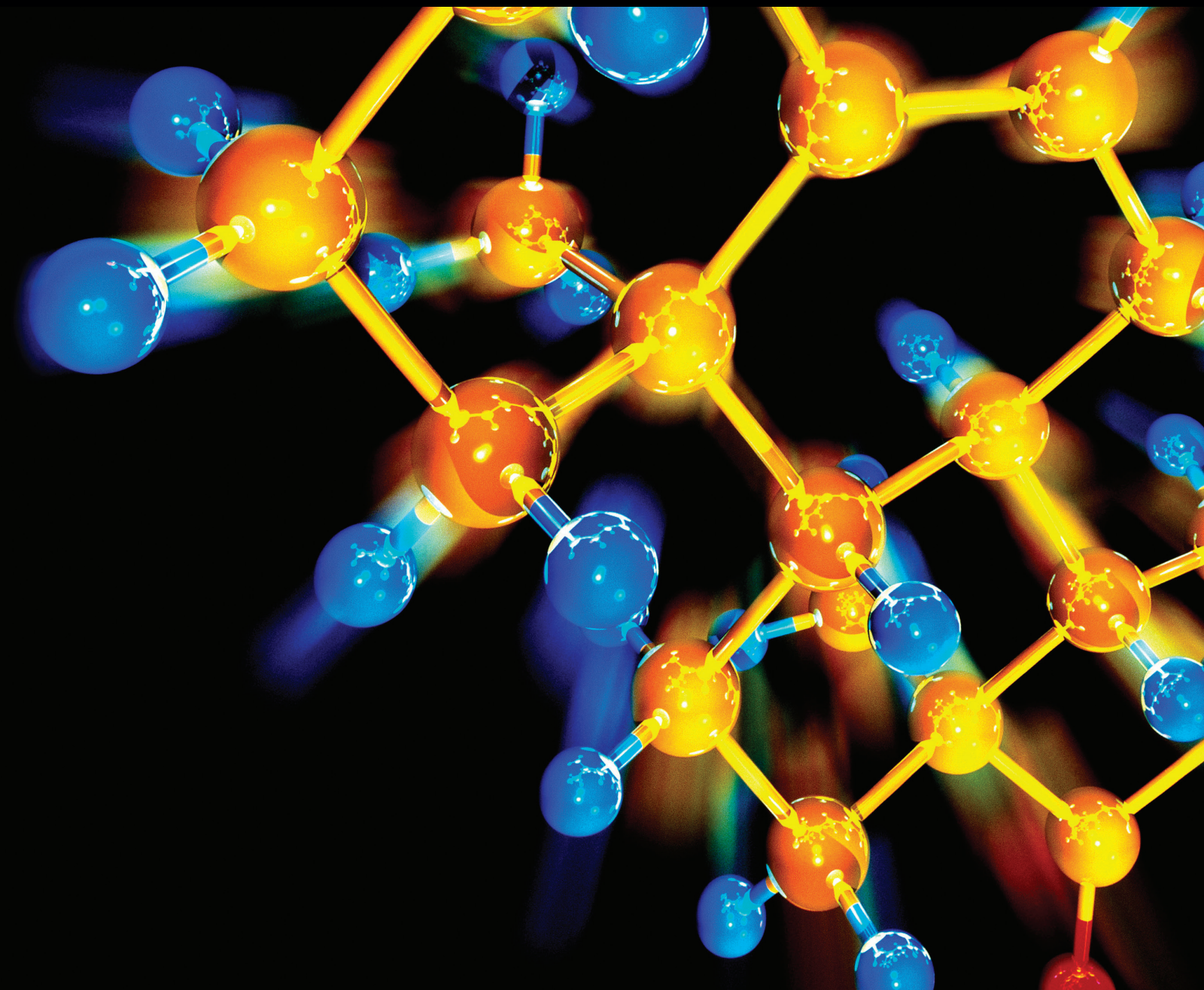


# Production and Application of Petroleum Oil and Its Alternatives on Internal Combustion Engines

Guest Editors: Haifeng Liu, Zheng Chen, Ming Huo, and Chao Jin





---

**Production and Application of Petroleum Oil  
and Its Alternatives on Internal Combustion  
Engines**

**Production and Application of Petroleum Oil  
and Its Alternatives on Internal Combustion  
Engines**

Guest Editors: Haifeng Liu, Zheng Chen, Ming Huo,  
and Chao Jin



---

Copyright © 2015 Hindawi Publishing Corporation. All rights reserved.

This is a special issue published in "Journal of Chemistry." All articles are open access articles distributed under the Creative Commons Attribution License, which permits unrestricted use, distribution, and reproduction in any medium, provided the original work is properly cited.

# Contents

**Production and Application of Petroleum Oil and Its Alternatives on Internal Combustion Engines,**  
Haifeng Liu, Zheng Chen, Ming Huo, and Chao Jin  
Volume 2015, Article ID 532580, 1 page

**Research on Control-Oriented Modeling for Turbocharged SI and DI Gasoline Engines,** Feitie Zhang,  
Shoudao Huang, Xuelong Li, and Fengjin Guan  
Volume 2015, Article ID 765083, 11 pages

**A New Multichelating Acid System for High-Temperature Sandstone Reservoirs,** Nianyin Li, Qian Zhang,  
Yongqing Wang, Pingli Liu, and Liqiang Zhao  
Volume 2015, Article ID 594913, 9 pages

**A Review on Homogeneous Charge Compression Ignition and Low Temperature Combustion by Optical  
Diagnostics,** Chao Jin and Zunqing Zheng  
Volume 2015, Article ID 910348, 23 pages

**Adsorption of Polymeric Additives Based on Vinyl Acetate Copolymers as Wax Dispersant and Its  
Relevance to Polymer Crystallization Mechanisms,** Ayman M. Atta, Rasha A. El-Ghazawy,  
Fatma A. Morsy, Ali M. S. Hebshy, and Abdullah Elmorsy  
Volume 2015, Article ID 683109, 8 pages

**Comparative Study on Particles Formation in a Diesel Engine When Lubricating Oil Involved in Fuel  
Combustion,** Lihui Dong, Weiqiang Han, Xingyu Liang, and Yuesen Wang  
Volume 2015, Article ID 839879, 7 pages

**Experimental Investigation of Injection Strategies on Low Temperature Combustion Fuelled with  
Gasoline in a Compression Ignition Engine,** Binbin Yang, Mingfa Yao, Zunqing Zheng, and Lang Yue  
Volume 2015, Article ID 207248, 10 pages

## *Editorial*

# **Production and Application of Petroleum Oil and Its Alternatives on Internal Combustion Engines**

**Haifeng Liu,<sup>1</sup> Zheng Chen,<sup>2</sup> Ming Huo,<sup>3</sup> and Chao Jin<sup>4</sup>**

<sup>1</sup>*State Key Laboratory of Engines, Tianjin University, Tianjin 300072, China*

<sup>2</sup>*Department of Energy & Power Engineering, Hunan University, Changsha, Hunan 410082, China*

<sup>3</sup>*EcoMotors Inc., Allen Park, MI 48101, USA*

<sup>4</sup>*School of Environmental Science and Engineering, Tianjin University, Tianjin 300072, China*

Correspondence should be addressed to Haifeng Liu; [haifengliu@tju.edu.cn](mailto:haifengliu@tju.edu.cn)

Received 9 June 2015; Accepted 10 June 2015

Copyright © 2015 Haifeng Liu et al. This is an open access article distributed under the Creative Commons Attribution License, which permits unrestricted use, distribution, and reproduction in any medium, provided the original work is properly cited.

Internal combustion engines are widely used in vehicles, ships, construction machinery, and agricultural machinery due to their reliability, durability, and high efficiency. Furthermore, they will be the main powertrains for above powerplant in the next 50 years according to the wide studies. However, the development of engines is faced with some serious challenges in the future, such as the stringent emission regulations, petroleum energy supply, and greenhouse gas emissions. Therefore, we need to develop some advanced combustion technologies to reduce the pollutant emissions. Meanwhile, to prevent global warming, we need to improve the thermal efficiencies of engines and thereby reduce CO<sub>2</sub> emissions and save petroleum oil.

Fuel properties have remarkable effects on engine performance and emissions. High-efficiency and low-emission engines must need the cooperation of high-quality fuels. Meantime, the future advanced engines may need the improved fuel properties which are different from the current gasoline or diesel fuel. In addition, the alternative biofuels have recently gained significant political and scientific interests owing to the concerns about climate change, global energy security, and petroleum supply shortage in the foreseeable future.

In this special issue, firstly, N. Li et al. from State Key Laboratory of Oil and Gas Reservoir Geology and Exploitation, Southwest Petroleum University, present the improvement on production of petroleum oil. Secondly, C. Jin and Z.-Q. Zheng from Tianjin University and B. Yang et al. from

Shandong University of Technology present the need for engine fuel properties for future advanced combustion modes such as homogeneous charge compression ignition and low temperature combustion. Finally, L. Dong et al. from Civil Aviation University of China and F. Zhang et al. from Hunan University present how to achieve high-efficiency and clean combustion based on cooperated control of fuel, oil, and engines.

Finally, we hope this special issue can give you some help to understand the tight relationship between petroleum and engines and to know the future engine combustion technologies and the needs for future engine fuels and oil.

*Haifeng Liu  
Zheng Chen  
Ming Huo  
Chao Jin*

## Research Article

# Research on Control-Oriented Modeling for Turbocharged SI and DI Gasoline Engines

Feitie Zhang,<sup>1</sup> Shoudao Huang,<sup>2</sup> Xuelong Li,<sup>3</sup> and Fengjin Guan<sup>3</sup>

<sup>1</sup>College of Mechanical and Vehicle Engineering, Hunan University, Changsha 410082, China

<sup>2</sup>College of Electrical and Information Engineering, Hunan University, Changsha 410082, China

<sup>3</sup>Lifan Passenger Vehicle Company Limited, Chongqing 401122, China

Correspondence should be addressed to Shoudao Huang; [shoudaohuang@tom.com](mailto:shoudaohuang@tom.com)

Received 9 January 2015; Accepted 26 February 2015

Academic Editor: Ming Huo

Copyright © 2015 Feitie Zhang et al. This is an open access article distributed under the Creative Commons Attribution License, which permits unrestricted use, distribution, and reproduction in any medium, provided the original work is properly cited.

In order to analyze system performance and develop model-based control algorithms for turbocharged spark ignition and direct injection (SIDI) gasoline engines, a control oriented mean value model is developed and validated. The model is constructed based on theoretical analysis for the different components, including the compressor, turbine, air filter, intercooler, throttle, manifold, and combustion chamber. Compressor mass flow and efficiency are modeled as parameterized functions. A standard nozzle model is used to approximate the mass flow through the turbine, and the turbine efficiency is modeled as a function of blade speed ratio (BSR). The air filter is modeled as a tube for capturing its pressure drop feature. The effectiveness number of transfer units (NTU) modeling method is utilized for the intercooler. The throttle model consists of the standard nozzle model with an effective area regressed to throttle position. Manifolds are modeled for their dynamically varying pressure state. For the cylinder, the air mass flow into cylinders, fuel mass, torque, and exhaust temperature are modeled. Compared to the conventional lookup table approach, transient dynamics error can be improved significantly through using the model from this work.

## 1. Introduction

With the development of advanced combustion gasoline engines under Chinese intellectual property, advanced combustion engines are becoming an important research focus [1–3]. The path for improving the engine performance is to utilize advanced technologies such as turbocharging and direct injection and use advanced combustion concepts like stratified combustion and homogenous charge compression ignition (HCCI). With the increasing complexity of engine systems, control of engine is becoming a complex task. Thus, dynamic simulation models and model-based designs are increasingly used for designing and optimizing engine control strategies. The objective of this paper is to develop a mean value engine model which describes properties of spark ignition and direct injection (SIDI) engines.

The reference [4] constructed turbocharger models which focused on compressor flow rate by a curve fitting method. A component based modeling methodology [5] was utilized for developing the models for the compressor efficiency,

compressor flow, and turbine flow. A simple model for the gas exchange process in diesel engine was developed in [6]. Based on thermodynamic analysis of compressor stage, a novel model-based approach was developed to predict the compressor behavior [7] which overcame the sparse nature of available compressor maps and characterized the flow and efficiency outputs of centrifugal compressors. Model predictive control was presented to coordinate throttle and turbocharger wastegate actuation for engine airflow and boost pressure control [8]. The model utilized the mass equation along with an isothermal manifold assumption. In order to design a controller for regulating speed of diesel engine, the nonlinear model was linearized and represented in a state-space form [9]. Reference [10] presented a control-oriented model for predicting major turbine variables in a turbocharged spark ignition engine. In the model, the turbine was simulated as a two-nozzle chamber.

In this paper, a complete mean value model is presented including compressor, turbine, air filter, intercooler, manifold, throttle, and cylinder. The proposed submodels

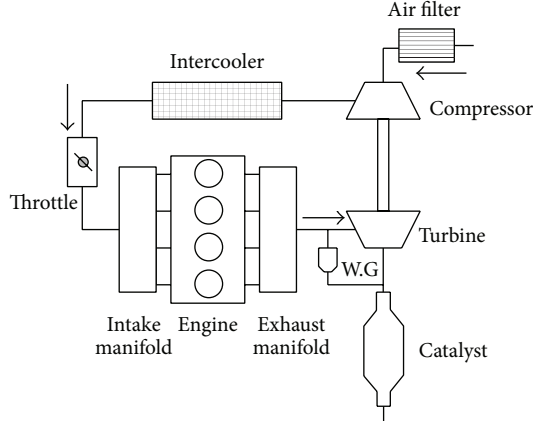


FIGURE 1: Sketch of the turbocharged SIDI engine.

capture key features of their corresponding component. All submodels are verified through the experimental data collected from a four-cylinder SIDI engine. Compressor and turbine models are developed as parameterized functions to describe the performance. The air filter is modeled as a simple pressure drop. The intercooler is modeled for its effect on intake temperature. The throttle is modeled to capture its flow rate. The manifolds are modeled with their pressure dynamics. For the cylinders, air mass flow into cylinders, fuel mass, and torque and exhaust temperature are modeled.

## 2. Engine Overview

The sketch of the turbocharged SIDI engine is displayed in Figure 1. The components to be modeled include compressor, turbine, air filter, intercooler, manifolds, throttle, and cylinders. Ambient air filtered through air filter is boosted by compressor. The boosted air is cooled down by intercooler and then flows into cylinder through throttle and intake manifold. A specified amount of fuel is injected into cylinder according to the mass of air. After combustion, the majority of exhaust gas exits, passing through the turbine and generating power for the compressor. The rest of the exhaust gas flows out through wastegate depending on the wastegate position. After being treated in the catalyst, exhaust gas returns back to the environment.

The specifications of the SIDI engine are shown in Table 1.

## 3. Modeling

**3.1. Compressor.** In order to supply the cylinder with air of high density, compressor pressurizes the air and directs it to the intake manifold. Compressor maps are usually described by corrected compressor mass flow, expansion ratio, modeled efficiency lines, and modeled speed lines. A compressor model should include the features from the map. In this paper, the compressor model consists of two submodels for compressor mass flow and compressor efficiency.

TABLE 1: Engine specifications.

Specification	Value	Unit
Displacement volume	2	Liter
Number of cylinders	4	—
Bore diameter	86	mm
Stroke length	86	mm
Compression ratio	10.75	—
Maximum torque	340@3500 rpm	N·m
Maximum power	178@5500 rpm	Kw

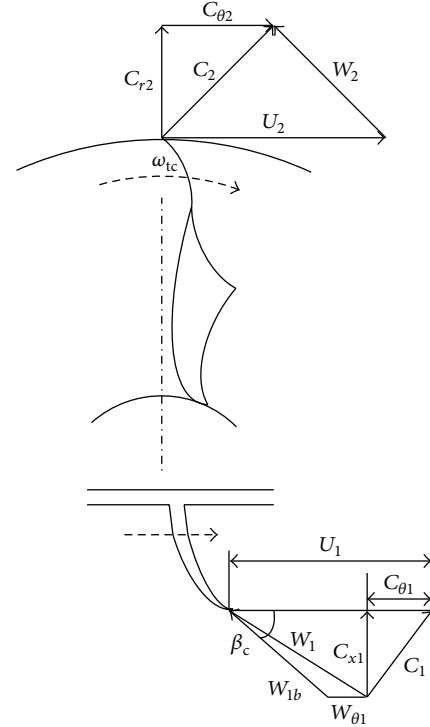


FIGURE 2: Velocity triangles of impeller eye and tip.

Based on analysis of specific energy transfer of compressor [11], Figure 2 shows the velocity triangles at the impeller eye and tip of the compressor with prewhirl:

$C_1$ : absolute velocity of air at impeller eye (inducer),

$C_{x1}$ : axial component of  $C_1$ ,

$C_{\theta 1}$ : tangential component of  $C_1$ ,

$U_1$ : tangential component of blade tip speed,

$W_1$ : air velocity relative to blade (impeller eye),

$W_{1b}$ : optimal value of  $W_1$ ,

$W_{\theta 1}$ : destruction of tangential component of  $W_1$ ,

$\beta_c$ : optimal angle,

$U_2$ : impeller tip speed,

$C_2$ : absolute velocity of air leaving impeller tip,

$C_{r2}$ : radial component of  $C_2$ ,

$C_{\theta 2}$ : tangential component of  $C_2$ ,

$W_2$ : air velocity relative to blade (tip),

$\omega_{tc}$ : turbo revolution speed.

According to geometrical relationships in Figure 2,

$$W_{\theta 1} = U_1 - C_{\theta 1} - \frac{C_{x1}}{\tan \beta_c}. \quad (1)$$

Assuming turbocharger compressors without stationary prewhirl, the air approaching the impeller does not include a tangential component; that is,  $C_{\theta 1} = 0$ .

Thus, (1) is rewritten as

$$W_{\theta 1} = U_1 - \frac{C_{x1}}{\tan \beta_c} = \omega_{tc} r_{c1} - \frac{C_{x1}}{\tan \beta_c} \quad (2)$$

$$C_{x1} = C_1 = \frac{\phi_c}{\rho_c A_c}, \quad (3)$$

where  $\phi_c$  is inlet mass flow,  $A_c$  is the inlet inducer cross-sectional area,  $\rho_c$  is air static density, and  $r_{c1}$  is inlet radius of impeller.

As the air adapts to the blade direction, the kinetic energy associated with the tangential component  $W_{\theta 1}$  is destroyed. Thus, the incidence loss is given by

$$h_{inc} = \frac{W_{\theta 1}^2}{2}. \quad (4)$$

From (2) and (4), (5) is derived:

$$h_{inc} = \frac{1}{2} \left( \omega_{tc} r_{c1} - \frac{\phi_c}{\rho_c A_c \tan \beta_c} \right)^2. \quad (5)$$

According to [11], the loss of useful energy due to friction is given by

$$h_{fric} = \delta_c \phi_c^2, \quad (6)$$

where  $\delta_c$  is an empirical constant.

Applying the Euler turbine equation and assuming  $C_{\theta 1} r_{c1} \ll C_{\theta 2} r_{c2}$ , the change of air angular momentum is given by

$$h_{total} = \omega_{tc} (r_{c2} C_{\theta 2} - r_{c1} C_{\theta 1}) = (\omega_{tc} r_{c2})^2, \quad (7)$$

where  $r_{c2}$  is outlet radius of impeller.

The specific energy for isentropic compression is given by

$$\Delta h_c = h_{total} - h_{inc} - h_{fric}. \quad (8)$$

Substituting (5), (6), and (7) into (8),

$$\Delta h_c = (\omega_{tc} r_{c2})^2 - \frac{1}{2} \left( \omega_{tc} r_{c1} - \frac{\phi_c}{\rho_c A_c \tan \beta_c} \right)^2 - \delta_c \phi_c^2. \quad (9)$$

The amount of energy required by the adiabatic compression process is given by

$$\Delta h_c = C_p T_{cin} \left( \frac{p_{cout}}{p_{cin}} \right)^{1-1/\gamma_c}, \quad (10)$$

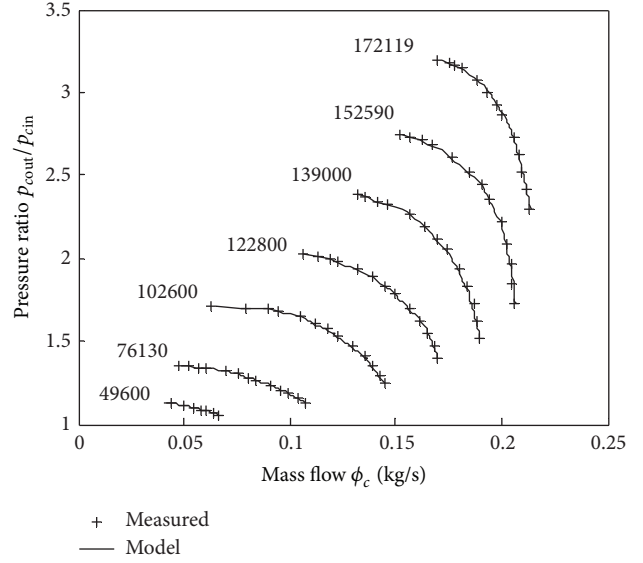


FIGURE 3: Mass flow model for compressor at stationary engine condition (the unit of compressor speed is rpm).

where  $p_{cout}$  and  $p_{cin}$  are the pressure out of compressor and into compressor, respectively,  $T_{cin}$  is the temperature of air into compressor,  $C_p$  is air heat capacity, and  $\gamma_c$  is specific heat capacity ratio.

Combining (9) with (10), the mass flow  $\phi_c$  through the compressor is derived:

$$\Phi_c = k_{n1} \omega_{tc} - k_{n2} \sqrt{k_{n3} \omega_{tc}^2 + k_{n4} \left[ \left( \frac{p_{cout}}{p_{cin}} \right)^{1-1/\gamma_c} - 1 \right]}, \quad (11)$$

where  $k_{n1} = 2\rho_c A_c \gamma_c \tan \beta_c / (2\delta_c (\rho_c A_c \tan \beta_c)^2 - 1)$ ,  $k_{n2} = \rho_c A_c \gamma_c \tan \beta_c / (-2\delta_c (\rho_c A_c \tan \beta_c)^2 - 1)$ ,  $k_{n3} = 2r_{c2}^2 - 2(\rho_c A_c \tan \beta_c)^2 \delta_c r_{c1}^2 + 4(\rho_c A_c \tan \beta_c)^2 \delta_c r_{c2}^2$ , and  $k_{n4} = -2C_p T_{cin} ((\rho_c A_c \tan \beta_c)^2 \delta_c + 1)$ .

For all parameters of (11), only  $\beta_c$  needs to be adjusted. This is different from other models. As shown in Figure 3, measured data of the mass flow agree with model simulation results accurately over the whole operating range. The average error is 0.12%. Figure 4 shows the results of fine-tuned parameter  $\beta_c$ .

The efficiency of the compressor is defined as the ratio of isentropic to the actual total input work:

$$\eta_c = \frac{h_{total} - h_{inc} - h_{fric}}{h_{total}}. \quad (12)$$

Substituting (5), (6), and (7) into (12), the efficiency is rewritten as

$$\eta_c = \frac{k_{c1}}{\omega_{tc}^2} \phi_c^2 + \frac{k_{c2}}{\omega_{tc}} \phi_c + k_{c3}, \quad (13)$$

where  $k_{c1} = (2\delta_c \rho_c A_c \tan \beta_c - 1) / 2(\rho_c A_c \tan \beta_c)^2 r_{c2}^2$  and  $k_{c2} = r_{c2} / r_{c2}^2 \rho_c A_c \tan \beta_c$ ,  $k_{c3} = 1 - (R_{c2}^2 / 2r_{c2}^2)$ .

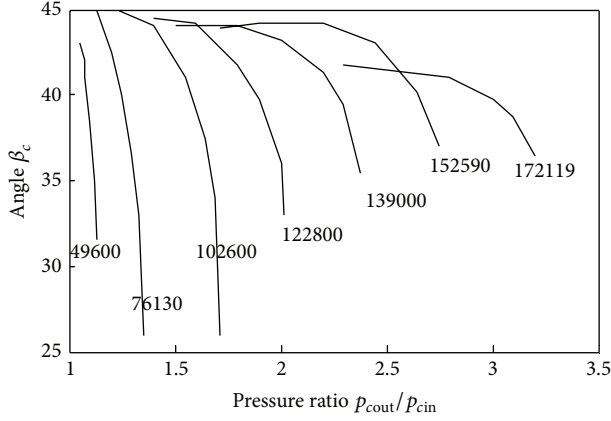


FIGURE 4: Optimal angle as parameter of compressor mass flow model (the unit of compressor speed is rpm).

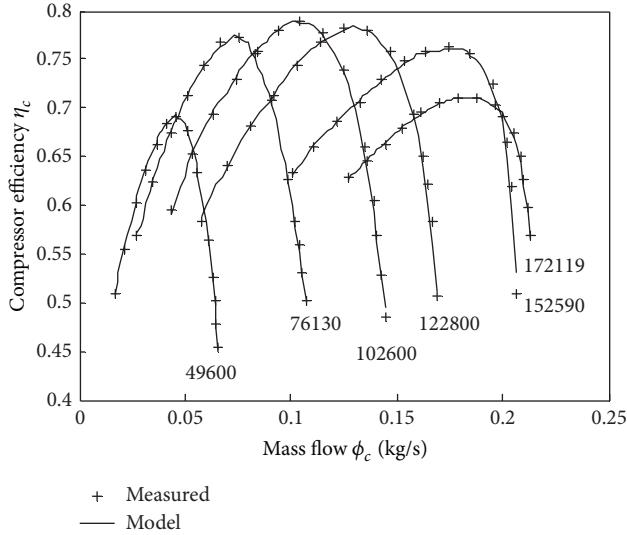


FIGURE 5: Efficiency model for compressor at stationary engine condition.

As shown in Figure 5, with the fine-tuned parameter  $\beta_c$ , measured data of the efficiency agree with model simulation results accurately over the whole operating range. Figure 6 shows the results of parameter  $\beta_c$ .

In addition, based on (13), compressor efficiency can also be modeled as a polynomial function, as shown in

$$\eta_c = f_{(a1,b1,c1,d1)} \left( \frac{\phi_c}{\omega_{tc}} \right)^4 + f_{(a2,b2,c2,d2)} \left( \frac{\phi_c}{\omega_{tc}} \right)^3 + f_{(a3,b3,c3,d3)} \left( \frac{\phi_c}{\omega_{tc}} \right)^2 + f_{(a4,b4,c4,d4)} \frac{\phi_c}{\omega_{tc}} + f_{(a5,b5,c5,d5)}, \quad (14)$$

where  $f_{(a,b,c,d)} = a\omega_{tc}^3 + b\omega_{tc}^2 + c\omega_{tc} + d$ .

The values of coefficients  $a$ ,  $b$ ,  $c$ , and  $d$  are shown in Table 2.

Figures 7, 8, and 9 show the simulation and measured results. The maximum relative error is about 7% which

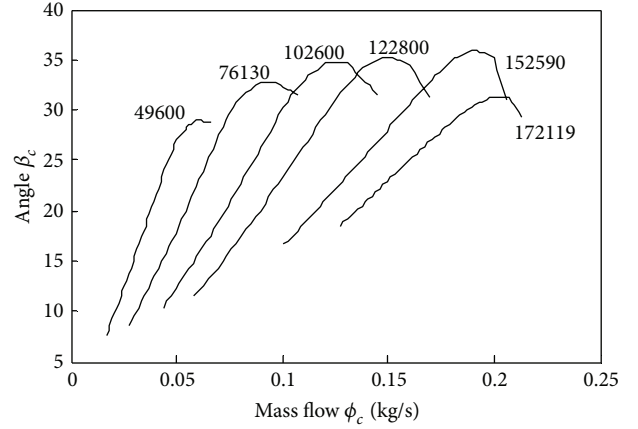


FIGURE 6: Optimal angle as parameter of compressor efficiency model.

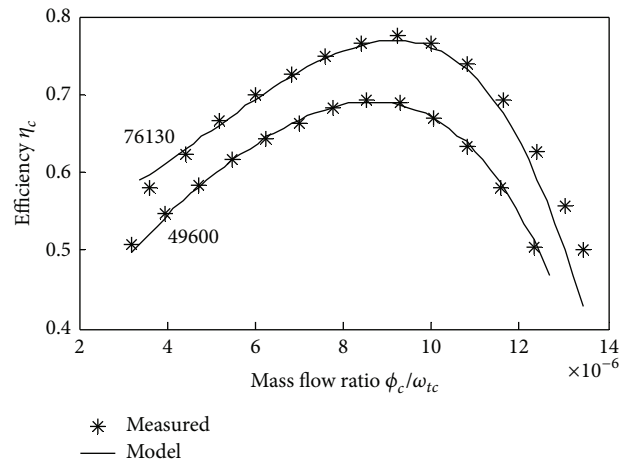


FIGURE 7: Efficiency model in polynomial form at stationary engine conditions (turbo speeds: 76130 rpm and 49600 rpm).

TABLE 2: Coefficient values of function  $f_{(a,b,c,d)}$ .

	$a$	$b$	$c$	$d$
$f_{(a1,b1,c1,d1)}$	$-1.49 * 10^6$	$2.66 * 10^{11}$	$-1.58 * 10^{16}$	$2.56 * 10^{20}$
$f_{(a2,b2,c2,d2)}$	50.71	$-8.53 * 10^6$	$4.56 * 10^{11}$	$-6.82 * 10^{15}$
$f_{(a3,b3,c3,d3)}$	$-6.75 * 10^{-4}$	111.88	$-5.64 * 10^6$	$7.52 * 10^{10}$
$f_{(a4,b4,c4,d4)}$	$4.15 * 10^{-9}$	$-7.06 * 10^{-4}$	36.22	$-4.52 * 10^5$
$f_{(a5,b5,c5,d5)}$	$-9.62 * 10^{-15}$	$1.67 * 10^{-9}$	$-8.62 * 10^{-5}$	1.55

occurs at speeds of 172119 rpm and 102600 rpm. For other compressor speeds, the relative error is less than 0.4%.

**3.2. Turbine.** Turbine is driven by the exhaust gas to provide power for compressor. The turbine model consists of sub-models for the turbine mass flow and the turbine efficiency.

Turbine mass flow is modeled as exhaust gas flowing through a nozzle [11, 12]. In particular, the pressure ratio at chock  $pr_{crit}$  of turbine is much higher than that of an adiabatic nozzle. The choke pressure ratio of turbine is measured

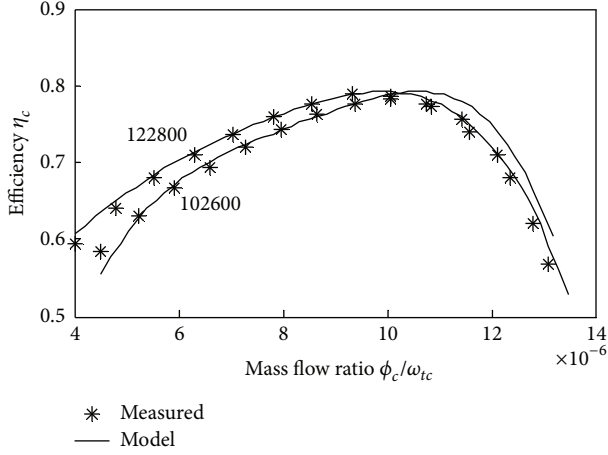


FIGURE 8: Efficiency model in polynomial form at stationary engine conditions (turbo speeds, 122800 rpm and 102600 rpm).

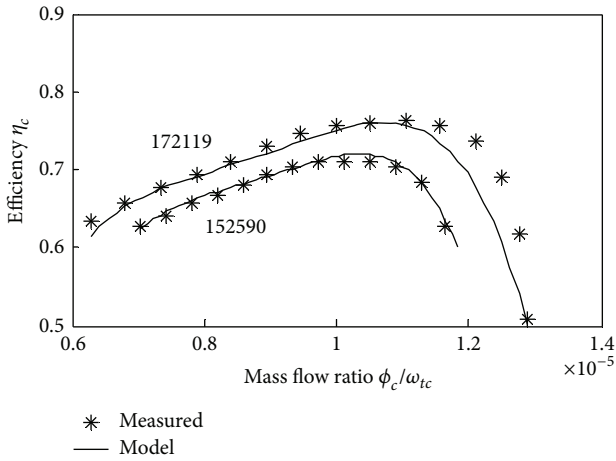


FIGURE 9: Efficiency model in polynomial form at stationary engine conditions (turbo speeds: 172119 rpm and 152590 rpm).

through experiments. At the condition in which  $p_{tout}/p_{tin} < pr_{crit}$ , choke occurs, and the calculation formula of turbine mass flow is shown in (15). When  $p_{tout}/p_{tin} > pr_{crit}$ , the calculation formula is shown in (16). In addition, turbine mass flow has a significant speed dependence, which is shown in Figure 10. Consider

$$\phi_{tb} = \frac{p_{ic}}{\sqrt{RT_{tin}}} A_t \sqrt{\frac{2\gamma}{\gamma-1} \left[ (pr_{crit})^{2/(\gamma-1)} - (pr_{crit})^{(\gamma+1)/(\gamma-1)} \right]} \quad (15)$$

$$\phi_{tb} = \frac{p_{tin}}{\sqrt{RT_{tin}}} A_t \sqrt{\frac{2\gamma}{\gamma-1} \left[ \left( \frac{p_{tout}}{p_{tin}} \right)^{2/\gamma} - \left( \frac{p_{tout}}{p_{tin}} \right)^{(\gamma+1)/\gamma} \right]}, \quad (16)$$

where  $p_{tin}$  is the turbine entry pressure,  $p_{tout}$  is the turbine exit pressure,  $T_{tin}$  is the entry temperature of air,  $\gamma = 1.4$  is the specific heat capacity ratio, and  $A_t$  is the effective

TABLE 3: Coefficient values of function  $A_t$ .

Coefficient	Value
$a_{tm1}$	$3.32 * 10^{-13}$
$b_{tm1}$	$-1.07 * 10^{-7}$
$c_{tm1}$	0.0101
$a_{tm2}$	$-2.69 * 10^{-13}$
$b_{tm2}$	$9.93 * 10^{-8}$
$c_{tm2}$	-0.0044

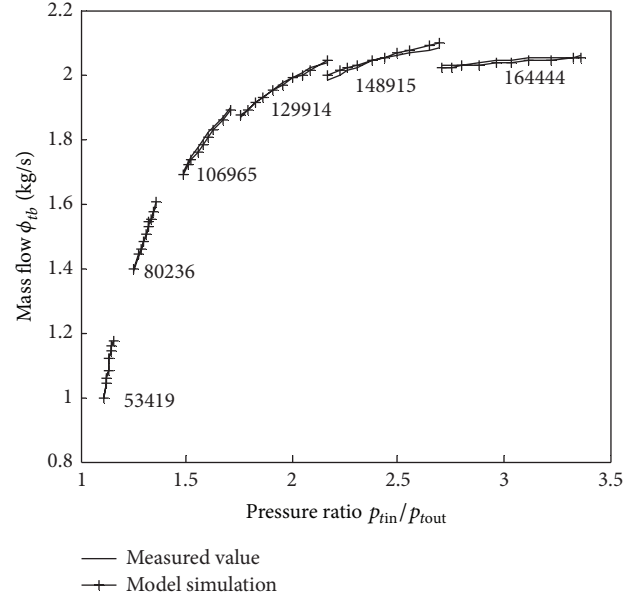


FIGURE 10: Turbine mass flow model.

cross-sectional area of turbine which varies with tangential component of velocity.  $A_t$  is given by

$$A_t = \left( a_{tm1} n_{tc}^2 + b_{tm1} n_{tc} + c_{tm1} \right) \frac{p_{tin}}{p_{tout}} + \left( a_{tm2} n_{tc}^2 + b_{tm2} n_{tc} + c_{tm2} \right), \quad (17)$$

where  $n_{tc}$  is the turbine revolution speed (in units of revolutions per minute) and  $a_{tm1}$ ,  $b_{tm1}$ ,  $c_{tm1}$ ,  $a_{tm2}$ ,  $b_{tm2}$ , and  $c_{tm2}$  are coefficients, whose values are shown in Table 3.

Measured and model simulation values of turbine mass flow for different speed are shown in Figure 10. The average error is 0.16%.

Blade speed ratio (BSR) [11] is defined as the ratio of speed at the mean blade height ( $U_t$ ) to the velocity. The velocity is calculated assuming isentropic expansion from the inlet conditions to the pressure at the exit from the turbine (total to static). The function is given by

$$BSR = \frac{U_t}{\sqrt{2c_p T_{tin} \left[ 1 - (p_{tout}/p_{tin})^{(\gamma-1)/\gamma} \right]}}. \quad (18)$$

TABLE 4: Coefficient values of function  $\eta_{tb}$ .

Coefficient	Value
$a_{te1}$	$-1.74 * 10^{-14}$
$b_{te1}$	$4.16 * 10^{-9}$
$c_{te1}$	$-2.64 * 10^{-4}$
$d_{te1}$	-1.9538
$a_{te2}$	$2.99 * 10^{-14}$
$b_{te2}$	$-7.33 * 10^{-9}$
$c_{te2}$	$4.97 * 10^{-4}$
$d_{te2}$	0.2828
$a_{te3}$	$-1.32 * 10^{-14}$
$b_{te3}$	$3.33 * 10^{-9}$
$c_{te3}$	$-2.43 * 10^{-4}$
$d_{te3}$	2.1765

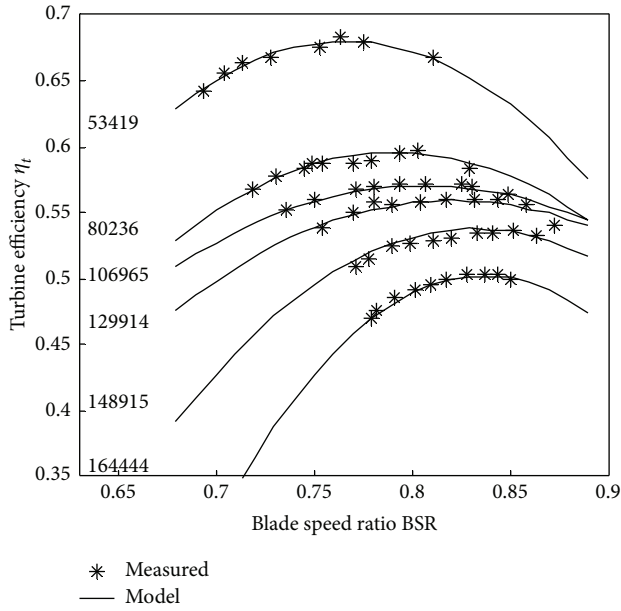


FIGURE 11: Turbine efficiency model.

Turbine efficiency is modeled as a polynomial function:

$$\begin{aligned} \eta_{tb} = & (a_{te1}n_{tc}^3 + b_{te1}n_{tc}^2 + c_{te1}n_{tc} + d_{te1})BSR^2 \\ & + (a_{te2}n_{tc}^3 + b_{te2}n_{tc}^2 + c_{te2}n_{tc} + d_{te2})BSR \\ & + (a_{te3}n_{tc}^3 + b_{te3}n_{tc}^2 + c_{te3}n_{tc} + d_{te3}), \end{aligned} \quad (19)$$

where  $a_i$ ,  $b_i$ ,  $c_i$ , and  $d_i$  ( $i = te1, te2, te3$ ) are coefficients, whose values are shown in Table 4.

The measured and simulation results are shown in Figure 11. The average error is 1.2%.

**3.3. Air Filter.** The most important feature of the air filter is the pressure drop that it causes. Air filter is modeled as a simple tube. According to pressure drop calculation for a tube

[13], air filter model can be described by (20). This model for pressure drop is also utilized by [5]:

$$\Delta P_{af} = C_{af} \frac{T_{af} \phi_{af}^2}{P_{af}}, \quad (20)$$

where  $\Delta P_{af}$  is pressure drop,  $C_{af}$  is a coefficient which depends on Reynolds number  $R_e$ , length and diameter of air filter, and gas constant  $R$ , and  $T_{af}$ ,  $P_{af}$ , and  $\phi_{af}$  are upstream temperature, pressure, and mass flow of incoming air, respectively.

**3.4. Intercooler.** In order to cool down the compressed intake air, increase its density, and decrease knock probability, an intercooler is used in the air path of the engine.

Cengel [13] described a method called the effectiveness number of transfer units (NTU) method for intercooler heat exchanger analysis. The method is based on a dimensionless parameter called the heat transfer effectiveness  $\varepsilon$ , defined as

$$\varepsilon = \frac{T_{ic,in} - T_{ic,out}}{T_{ic,in} - T_{cool}}, \quad (21)$$

where  $T_{ic,in}$  is the temperature of hot air that enters into intercooler,  $T_{ic,out}$  is the temperature of cooled air that outflows intercooler, and  $T_{cool}$  is the temperature of ambient air that blows towards intercooler. According to (21), the temperature of cooled air  $T_{ic,out}$  that flows out of intercooler is given by

$$T_{ic,out} = T_{ic,in} - \varepsilon(T_{ic,in} - T_{cool}). \quad (22)$$

A detailed derivation for calculating the heat transfer effectiveness  $\varepsilon$  is presented in [13]. The final equations are shown below:

$$\varepsilon = 1 - \exp \left\{ \frac{NTU^{0.22}}{c} [\exp(-c \cdot NTU^{0.78}) - 1] \right\},$$

$$NTU = \frac{U \cdot A_s}{C_p \phi_{ic}}, \quad (23)$$

$$c = \frac{\phi_{ic}}{\phi_{cool}},$$

where  $U$  is the overall heat transfer coefficient,  $A_s$  is the intercooler surface area,  $C_p$  is air heat capacity,  $\phi_{ic}$  is the mass of compressed air from compressor, and  $\phi_{cool}$  is the mass of ambient air.

The advantage of NTU is that the model includes heat transfer physics. However, it is not accurate enough and the calculation of  $\varepsilon$  is complex. Based on measured data, Eriksson [14] developed a regression model for the calculation of  $\varepsilon$

$$\varepsilon = a_0 + a_1 \left( \frac{T_{ic,in} + T_{cool}}{2} \right) + a_2 \phi_{ic} + a_3 \frac{\phi_{ic}}{\phi_{cool}}. \quad (24)$$

It is assumed that there is no pressure loss for intercooler, which gives the following equation:

$$P_{ic,out} = P_{ic,in}. \quad (25)$$

TABLE 5: Coefficient values of the effective opening area.

Coefficient	$a_{th2}$	$a_{th1}$	$a_{th0}$
Value	-0.1514	0.7816	0.1635

**3.5. Throttle.** The throttle controls the amount of air flowing into cylinders in SI engine at part load. The butterfly type throttle is regarded as a nozzle with compressible gas flow. Heywood [15] described the model for the nozzle and [14, 16] used this method to develop the throttle model. Formulae are presented below.

When the gas velocity flowing through the throat of throttle is equal to or larger than the velocity of sound, that is,  $p_{imf}/p_{ic} < (2/(\gamma + 1))^{\gamma/(\gamma-1)}$ , the maximum mass flow occurs. The formula of calculating mass flow  $\phi_{th}$  is shown in

$$\phi_{th} = C_d A_{th} \frac{p_{ic}}{\sqrt{RT_{ic,out}}} \cdot \sqrt{\frac{2\gamma}{\gamma-1} \left[ \left( \frac{2}{\gamma+1} \right)^{2/(\gamma-1)} - \left( \frac{2}{\gamma+1} \right)^{(\gamma+1)/(\gamma-1)} \right]} \quad (26)$$

When the gas velocity is less than the velocity of sound, the formula of calculating mass flow is shown in

$$\phi_{th} = C_d A_{th} \frac{p_{ic}}{\sqrt{RT_{ic,out}}} \sqrt{\frac{2\gamma}{\gamma-1} \left[ \left( \frac{p_{imf}}{p_{ic}} \right)^{2/\gamma} - \left( \frac{p_{imf}}{p_{ic}} \right)^{(\gamma+1)/\gamma} \right]} \quad (27)$$

where  $A_{th}$  is the throttle plate opening area,  $C_d$  is the discharge coefficient,  $p_{imf}$  is the air pressure in intake manifold, and  $\gamma = 1.4$  is the specific heat capacity ratio. The effective opening area  $C_d A_{th}$  is a function of throttle opening angle  $\alpha$ . The function is shown below:

$$C_d A_{th} = A_1 (1 - \cos(a_{th2}\alpha^2 + a_{th1}\alpha + a_{th0})) + A_0, \quad (28)$$

where  $A_1$  is the throttle bore area,  $A_0$  is leakage area, and  $a_{th2}$ ,  $a_{th1}$ , and  $a_{th0}$  are fit coefficients based on measured data, whose values are shown in Table 5.

Model simulation results versus measured values of effective area are shown in Figure 12 and results of mass flow through throttle are shown in Figure 13. The models capture the main characters of effective area and mass flow through throttle.

**3.6. Manifold.** For the intake and exhaust manifolds, pressure in manifold depends on the change rate of the total air mass, which is equal to the sum of the air mass flows into and out of the manifold. Manifold models can be created according to

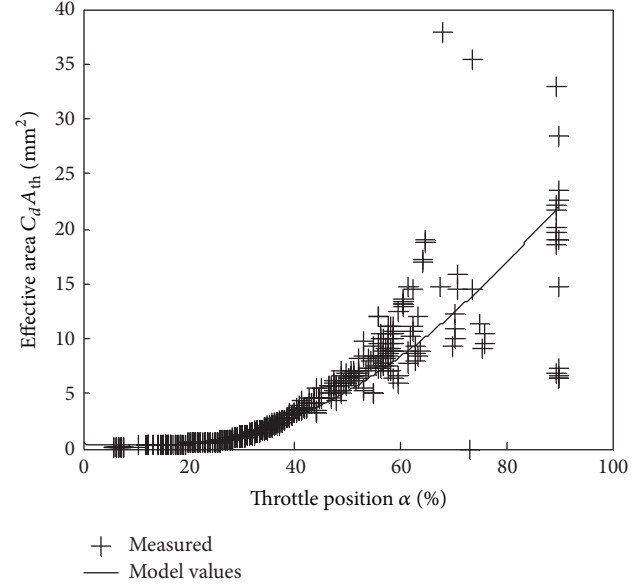


FIGURE 12: Effective area of throttle.

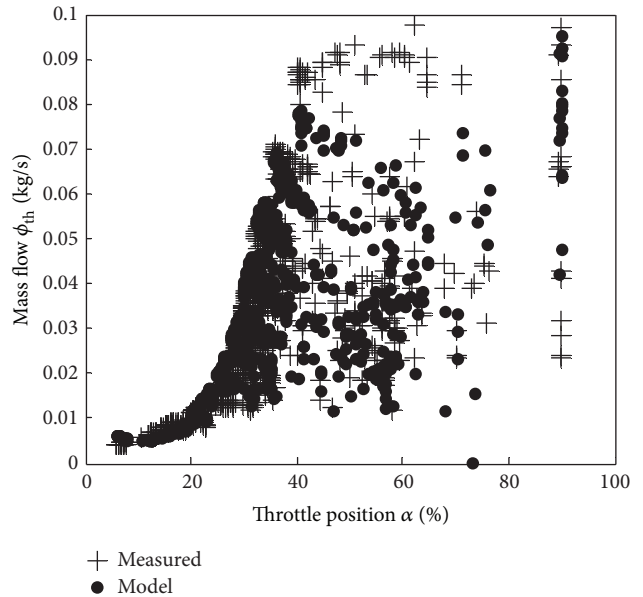


FIGURE 13: Air mass flow through throttle.

isothermal model [15, 17]. The intake and exhaust manifolds are modeled as follows:

$$\begin{aligned} \frac{dp_{imf}}{dt} &= \frac{R_a T_{imf}}{V_{imf}} (\phi_{th} - \phi_{ein}) \\ \frac{dp_{emf}}{dt} &= \frac{RT_{emf}}{V_{emf}} (\phi_{eout} - \phi_{tb}), \end{aligned} \quad (29)$$

where  $p_{imf}$  and  $p_{emf}$  are the pressure of intake and exhaust manifolds, respectively,  $T_{imf}$  is the temperature of air flowing into intake manifold, which is assumed to be equal to the temperature of cooled air that exits intercooler,  $T_{emf}$  is the temperature of exhaust manifold,  $V_{imf}$  and  $V_{emf}$  are volumes

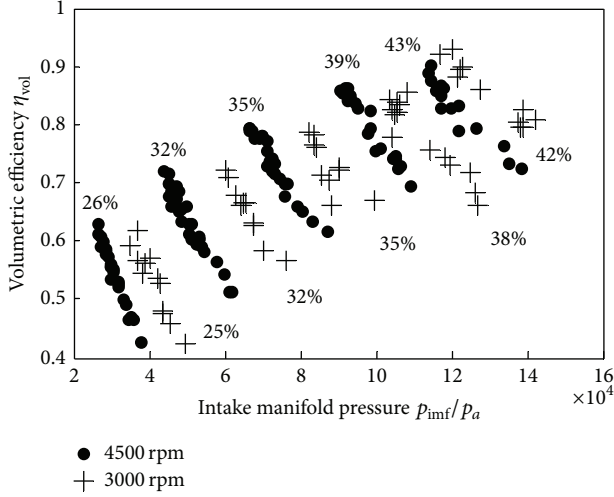


FIGURE 14: Volumetric efficiency for engine speeds 4500 rpm and 3000 rpm.

of intake and exhaust manifolds,  $\phi_{\text{ein}}$  is the mass flow from the intake manifold into the cylinders, and  $\phi_{\text{eout}}$  is the total mass flow out from cylinder. The ideal gas constant  $R_a$  of intake manifold and ideal gas constant  $R$  of exhaust manifold are different because  $T_{\text{emf}}$  is much higher than  $T_{\text{imf}}$ .

3.7. *Cylinder.* The total mass flow  $\phi_{ei}$  into the cylinder is modeled using the standard model based on volumetric efficiency:

$$\phi_{ei} = \frac{\eta_{\text{vol}}(p_{\text{imf}}, n_e, \alpha) p_{\text{imf}} n_e V_d}{120 R_a T_{\text{imf}}}, \quad (30)$$

where  $p_{\text{imf}}$  is the air pressure in the intake manifold.  $T_{\text{imf}}$  is the air temperature in the intake manifold,  $n_e$  is engine speed,  $V_d$  is displacement volume, and  $\eta_{\text{vol}}$  is volumetric efficiency which is a function of  $p_{\text{imf}}$ ,  $n_e$ , and throttle opening angle  $\alpha$ .  $\eta_{\text{vol}}$  is a function of engine speed, throttle position, and intake manifold pressure and the results are shown in Figures 14 and 15. For a given engine and throttle position, volumetric efficiency varies with intake manifold pressure as the cylinder intake and exhaust valve timings are changed. For example, in Figure 14, at the condition in which engine speed is equal to 4500 rpm and throttle position is equal to 26%, the volumetric efficiency varies from 0.63 to 0.42.

The fuel mass flow  $\phi_{ef}$  injected into cylinder varies with air fuel ratio. The fuel mass flow can be modeled [7] with fuel mass flow variable  $\mu_\delta$  which has units of milligrams, engine speed  $n_e$ , and the number of cylinder  $n_{\text{cyl}}$ :

$$\phi_{ef} = \frac{10^{-6}}{120} \mu_\delta n_e n_{\text{cyl}}. \quad (31)$$

The mass flow out from the cylinder is the sum of the total mass flow into cylinders  $\phi_{ei}$  and the fuel mass injected into cylinders  $\phi_{ef}$ .

For the engine torque  $M_e$ , based on the engine friction definition in reference [15], it can be calculated from gross

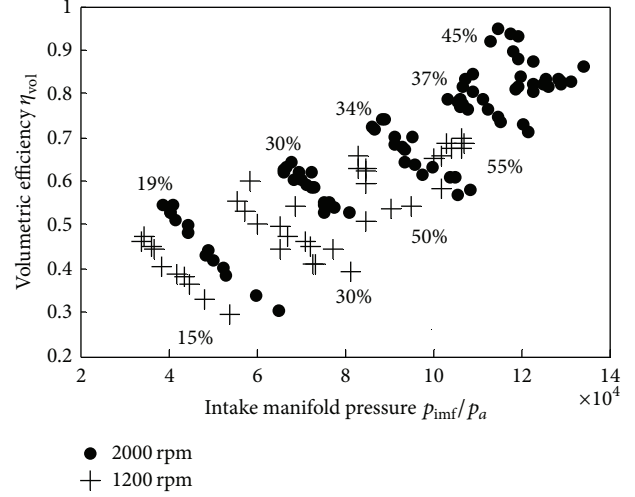


FIGURE 15: Volumetric efficiency for engine speeds 2000 rpm and 1200 rpm.

indicated torque  $M_{ig}$  and total friction torque  $M_{tf}$ . The total friction torque includes friction torques produced by pumping work, rubbing friction work, and accessory work. The engine torque is then

$$M_e = M_{ig} - M_{tf}. \quad (32)$$

The gross indicated torque is calculated from fuel consumption:

$$M_{ig} = \frac{30 \phi_{ef} Q_{\text{HV}} \eta_{ig}}{\pi n_e}, \quad (33)$$

where  $\eta_{ig} = 1 - (1/r_c^{\gamma-1})$  (this assumes instantaneous adiabatic combustion at top dead center), where  $r_c$  is the compression ratio and  $\gamma$  is the specific heat capacity ratio, and  $Q_{\text{HV}}$  is the fuel heating value.

The total friction torque of SI engine is modeled as a function of engine speed:

$$M_{tf} = \frac{V_d 10^5}{4\pi} \left( C_{f1} + C_{f2} \frac{n_e}{1000} + C_{f3} \left( \frac{n_e}{1000} \right)^2 \right). \quad (34)$$

Exhaust temperature  $T_{\text{exh}}$  is important to model turbocharged engines. Models for exhaust temperature in reference [17] have two components, which are an exhaust manifold temperature and a temperature drop in a straight pipe.

The exhaust manifold temperature is modeled as

$$T_{\text{cyl}} = e^{a_{\text{cy}} + (b_{\text{cy}}/\phi_{\text{exh}})}, \quad (35)$$

where  $T_{\text{cyl}}$  is temperature of the fluid delivered by the cylinder to the exhaust manifold,  $\phi_{\text{exh}}$  is the exhaust mass flow, and  $a_{\text{cy}}$  and  $b_{\text{cy}}$  are tuning parameters, whose values are 7.239 and -0.005, respectively.

The temperature at the turbine inlet is modeled as (36), which is based on temperature drop in a straight pipe:

$$T_{\text{exh}} = T_{\text{amb}} + (T_{\text{cyl}} - T_{\text{amb}}) e^{-h_{\text{cv}} \pi d_{\text{pipe}} l_{\text{pipe}} / \phi_{\text{exh}} C_p}, \quad (36)$$

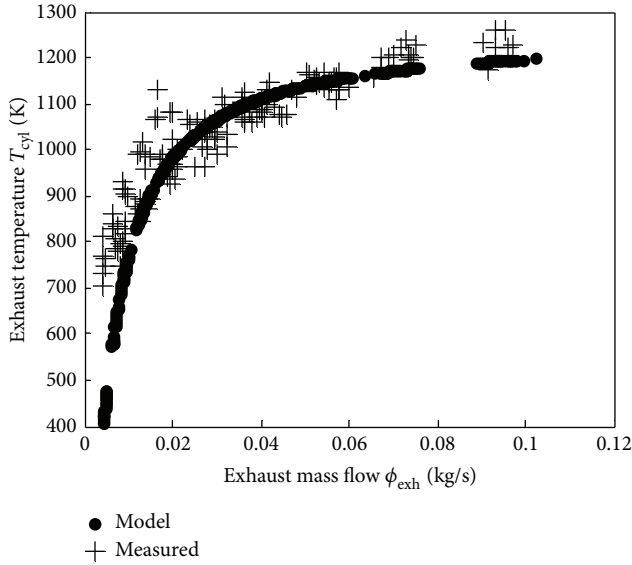


FIGURE 16: Model of the temperature at the turbine inlet.

where  $T_{amb}$  is the pipe wall temperature which is equal to ambient temperature,  $h_{cv}$  is the total transfer coefficient,  $d_{pipe}$  and  $l_{pipe}$  are the diameter and length of exhaust pipe, respectively, and  $C_p$  is the heat capacity. The model validated results are shown in Figure 16.  $T_{cyl}$  is predicted utilizing (35) and the parameters of  $T_{cyl}$  are tuned.

### 4. Experiment and Simulation

All engine models above are parameterized to experimental data that are collected on a 2.0 L four-cylinder turbocharged SIDI engine at steady state conditions. Sensors like in-cylinder pressure sensors, k-type thermocouples, and air flow meter are equipped on the test bench. The models are validated at engine speeds from 1000 RPM up to 4500 RPM.

The whole simulation models are implemented in Simulink according to the physical engine system, as shown in Figure 17. The parameters and coefficients of the models are listed in Section 3. The completed model includes inter-cooler, throttle, intake manifold, cylinder, air filter, compressor, turbo, turbine, and exhaust manifold.

The engine was operated at around 2200 r/min with gasoline 97#. Figures 18 and 19 show the other engines' working conditions. The throttle position was stepped from 33.7% open to 45.5% open, after holding for 35 seconds, and then fell back to 38.4% open. The varying tendency of injection duration is almost the same.

In Figures 20–23, the simulated results are compared to the experimental measurements. The model is able to capture the transient dynamics and estimate the outputs with desirable accuracy. In Figure 20, the modeled intake mass flow results are a little ahead of experimental measurements at the rising phase. After that, the model retains its good tracking performance. The transient error is a result of the response time of the air mass flow transducer. In Figure 21, the model tracks the transient dynamics well at the rising

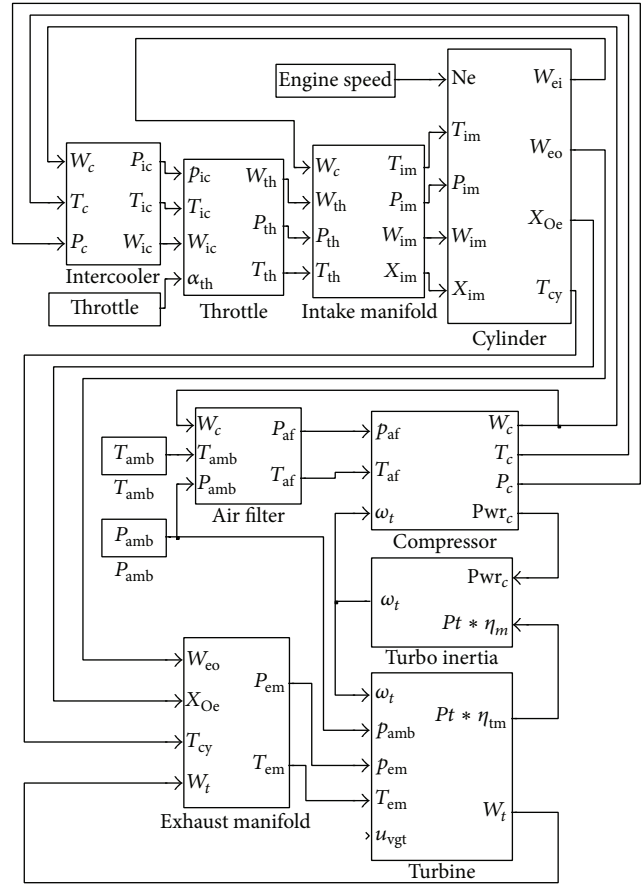


FIGURE 17: Complete control-oriented model.

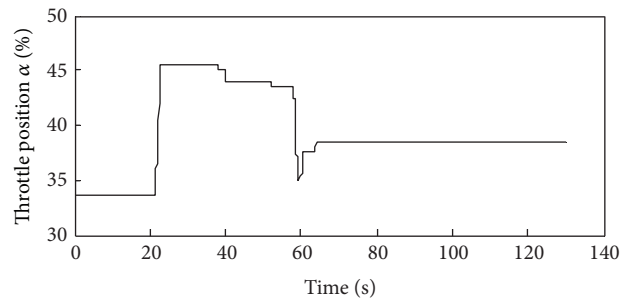


FIGURE 18: Throttle position of engine operation conditions.

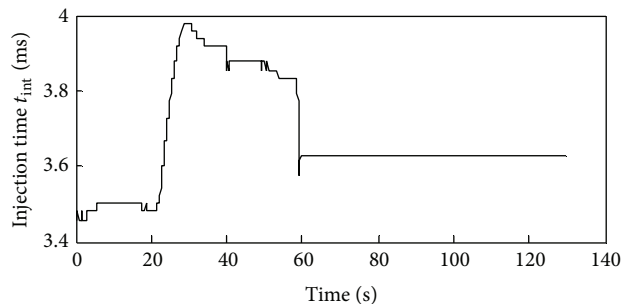


FIGURE 19: Injection duration of engine operation conditions.

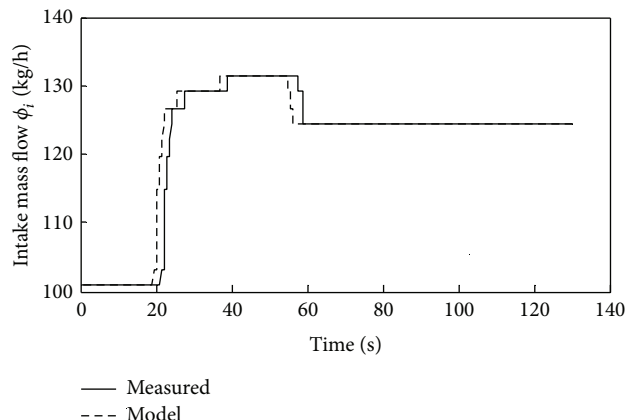


FIGURE 20: Measured and modeled results of intake air mass flow.

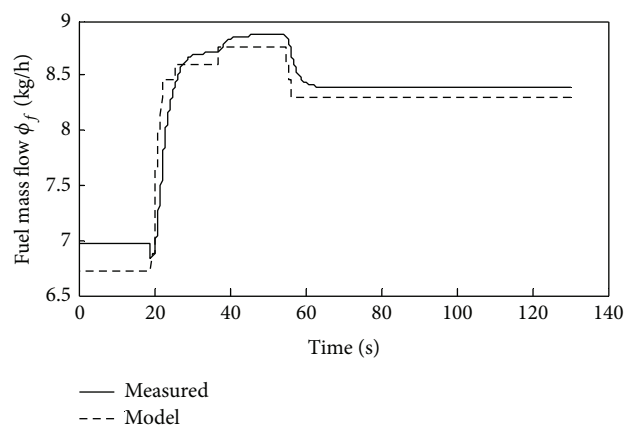


FIGURE 21: Measured and modeled results of fuel mass flow.

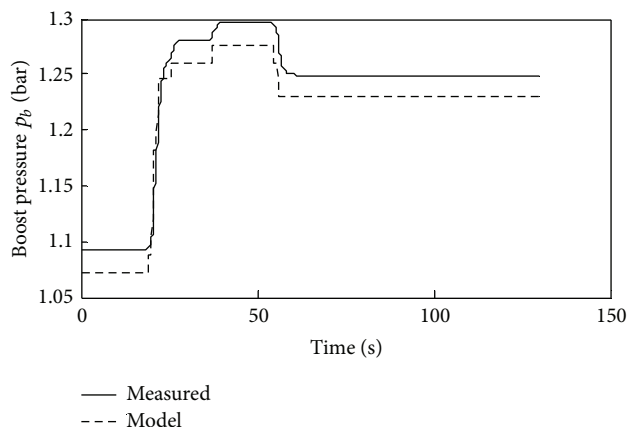


FIGURE 22: Measured and modeled results of boost pressure.

phase, but, in stable phase, the estimation error is 0.11, about 1.3%. The boost pressure and intake manifold pressure results shown in Figures 22 and 23 have the same characteristics with fuel mass flow.

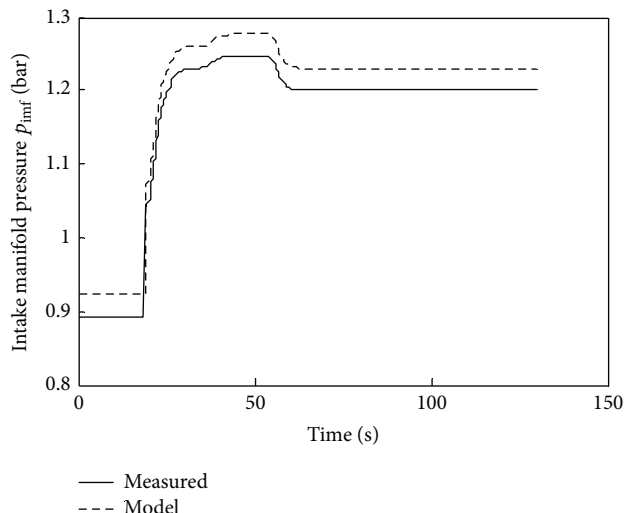


FIGURE 23: Measured and modeled results of intake manifold pressure.

## 5. Conclusions

A complete mean value model based on component sub-models has been developed and validated. The intended applications of the models are developments of model-based control strategies and system analysis. Several submodels were described and novel models for compressor flow and compressor efficiency were developed. The accuracy of the new compressor model has an average error of 0.12%, which is a significant improvement over conventional mapping approaches. The experimental results confirm that the developed model is capable of tracking transient dynamics. Compared to the conventional lookup table approach, our validation results show that transient dynamics error can be improved significantly through using the model from this work.

## Conflict of Interests

The authors declare that there is no conflict of interests regarding the publication of this paper.

## Acknowledgments

The authors would like to acknowledge Dr. Patrick Gorzelic of the University of Michigan (Ann Arbor) for the discussions and suggestions about the models. This project is supported by National Natural Science Foundation of China (no. 51475151), China Scholarship Council Foundation (no. 2012-3022), and Hunan University Young Teachers Sponsor Project.

## References

- [1] G. A. Lavoie, J. Martz, M. Wooldridge, and D. Assanis, "A multi-mode combustion diagram for spark assisted compression

- ignition,” *Combustion and Flame*, vol. 157, no. 6, pp. 1106–1110, 2010.
- [2] P. Gorzelic, P. Shingne, J. Martz, and G. A. Stefanopoulou, “A low-order HCCI model extended to capture SI-HCCI mode transition data with two-stage cam switching,” in *Proceedings of the ASME Dynamic Systems and Control Conference*, San Antonio, Tex, USA, October 2014.
- [3] E. Hellstrom, J. Larimore, S. Jade, A. G. Stefanopoulou, and L. Jiang, “Reducing cyclic variability while regulating combustion phasing in a four-cylinder HCCI engine,” *IEEE Transactions on Control Systems Technology*, vol. 22, no. 3, pp. 1190–1197, 2014.
- [4] P. Moraal and I. Kolmanovsky, “Turbocharger modeling for automotive control applications,” in *Proceedings of the SAE World Congress & Exhibition*, Detroit, Mich, USA, March 1999.
- [5] L. Eriksson, “Modeling and control of turbocharged SI and DI engines,” *Oil & Gas Science and Technology*, vol. 62, no. 4, pp. 523–538, 2007.
- [6] L. Kocher, E. Koeberlein, K. Stricker, D. G. van Alstine, B. Biller, and G. M. Shaver, “Control-oriented modeling of diesel engine gas exchange,” in *Proceedings of the American Control Conference (ACC '11)*, pp. 1555–1560, San Francisco, Calif, USA, June–July 2011.
- [7] M. Taburri, F. Chiara, M. Canova, and Y.-Y. Wang, “A model-based methodology to predict the compressor behaviour for the simulation of turbocharged engines,” *Proceedings of the Institution of Mechanical Engineers, Part D: Journal of Automobile Engineering*, vol. 226, no. 4, pp. 560–574, 2012.
- [8] M. Santillo and A. Karnik, “Model Predictive Controller design for throttle and wastegate control of a turbocharged engine,” in *Proceedings of the American Control Conference (ACC '13)*, pp. 2183–2188, IEEE, Washington, DC, USA, June 2013.
- [9] D. Malkhede and B. Seth, “State feedback speed controller for turbocharged diesel engine and its robustness,” *World Academy of Science, Engineering and Technology*, vol. 75, pp. 119–125, 2013.
- [10] R. Salehi, M. Shahbakhti, A. Alasty, and G. R. Vossoughi, “Control oriented modeling of a radial turbine for a turbocharged gasoline engine,” in *Proceedings of the American Control Conference (ACC '13)*, pp. 5207–5212, Washington, DC, USA, June 2013.
- [11] N. Watson and M. S. Janota, *Turbocharging the Internal Combustion Engine*, Macmillan, Basingstoke, UK, 1982.
- [12] P. Moraal and I. Kolmanovsky, “Turbocharger modeling for automotive control applications,” in *Proceedings of the SAE International Congress & Exposition*, Paper no. 1999-01-0908, pp. 1–14, Detroit, Mich, USA, March 1999.
- [13] Y. A. Cengel, *Heat Transfer: A Practical Approach*, McGraw-Hill, New York, NY, USA, 2002.
- [14] L. Eriksson, L. Nielsen, J. Brugård, J. Bergström, F. Pettersson, and P. Andersson, “Modeling of a turbocharged SI engine,” *Annual Reviews in Control*, vol. 26, no. 1, pp. 129–137, 2002.
- [15] J. B. Heywood, *Internal Combustion Engine Fundamentals*, McGraw-Hill, New York, NY, USA, 1988.
- [16] M. Nyberg and L. Nielsen, “Model based diagnosis for the air intake system of the SI-engine,” in *Proceedings of the SAE International Congress & Exposition*, Paper no. 970209, Detroit, Mich, USA, February 1997.
- [17] L. Eriksson, “Mean value models for exhaust system temperature,” in *Proceedings of the SAE World Congress & Exhibition*, Paper no. 2002-01-0374, Detroit, Mich, USA, March 2002.

## Research Article

# A New Multichelating Acid System for High-Temperature Sandstone Reservoirs

Nianyin Li, Qian Zhang, Yongqing Wang, Pingli Liu, and Liqiang Zhao

State Key Lab of Oil and Gas Reservoir Geology and Exploitation, South West Petroleum University, Chengdu, Sichuan 610500, China

Correspondence should be addressed to Nianyin Li; [linianyin@swpu.edu.cn](mailto:linianyin@swpu.edu.cn)

Received 2 November 2014; Accepted 2 January 2015

Academic Editor: Ming Huo

Copyright © 2015 Nianyin Li et al. This is an open access article distributed under the Creative Commons Attribution License, which permits unrestricted use, distribution, and reproduction in any medium, provided the original work is properly cited.

Sandstone reservoir acidizing is a complex and heterogeneous acid-rock reaction process. If improper acid treatment is implemented, further damage can be induced instead of removing the initial plug, particularly in high-temperature sandstone reservoirs. An efficient acid system is the key to successful acid treatment. High-temperature sandstone treatment with conventional mud acid system faces problems including high acid-rock reaction rate, short acid effective distance, susceptibility to secondary damage, and serious corrosion to pipelines. In this paper, a new multichelating acid system has been developed to overcome these shortcomings. The acid system is composed of ternary weak acid, organic phosphonic chelating agent, anionic polycarboxylic acid chelating dispersant, fluoride, and other assisted additives. Hydrogen ion slowly released by multistage ionization in ternary weak acid and organic phosphonic within the system decreases the concentration of HF to achieve retardation. Chelating agent and chelating dispersant within the system inhibited anodic and cathodic reaction, respectively, to protect the metal from corrosion, while chelating dispersant has great chelating ability on iron ions, restricting the depolarization reaction of ferric ion and metal. The synergic effect of chelating agent and chelating dispersant removes sulfate scale precipitation and inhibits or decreases potential precipitation such as  $\text{CaF}_2$ , silica gel, and fluosilicate. Mechanisms of retardation, corrosion-inhibition, and scale-removing features have been discussed and evaluated with laboratory tests. Test results indicate that this novel acid system has good overall performance, addressing the technical problems and improving the acidizing effect as well for high-temperature sandstone.

## 1. Introduction

Sandstone matrix acidizing is one of the essential technical strategies to maintain or increase the productivity of hydrocarbon wells or the injectivity of water injectors. With the flow and reaction of acid in intergranular porosity and cavity, the near wellbore region damaged by drilling, completion, workover, or injection of water can be removed to recover or increase the production. The acid-rock reaction in sandstone matrix is a fairly complex process, including the chemical reaction between a variety of minerals and hydrofluoric acid, which happens most in porous media, and is considered as multiphase “heterogeneity” reaction. Since there are different minerals reaction rate with acids and difficulty in measurement, the reaction process is beyond accurate prediction. Therefore, improper acidizing treatment not only cannot remove the original plugs, but also bring further damage to reservoir [1–5].

Stimulation effect is highly dependent on acid systems. To implement a successful acid treatment, an optimized acid system considering the formation characteristics and the function and performance of both acids and additives should be applied to meet requirements of the treatment.

In high temperature conditions, regular mud acid reacts rapidly, with limited effective distance, and untouched to the deep reservoir. Moreover, regular mud acid could induce massive secondary precipitation and heavy corrosion on downhole tubulars and devices. Corrosion inhibitors have been used with acids for decades but their function is limited in some extreme conditions, especially under high temperature circumstances. Corrosion inhibitors can be classified into 5 categories: amino polycarboxylic type, hydroxy carboxylic type, amino type, organic phosphate type, and polycarboxylic type. The first use of chelating agent was to dissolve carbonate in 1973 [6]. And in 1985, Tyler et al. first used EDTA in sandstone reservoir [7]. Several of researches

have proved the great advantage of chelating agent in acid treatment of sandstone reservoir, leading to wide use like EDTA, HEDTA, NTA, and so forth [8]. Al-Harbi et al. introduced the application of chelating agents to sandstone acid systems in 2013 [9]. For acidizing treatment in high-temperature sandstone reservoir, chelating agents use is the future for improving treatment effectively [10–17]. Due to the limitations of pros and cons of single chelating agent usage, this paper introduces a synergic affected optimized mixture of chelating agent and dispersant, a high-temperature multichelating acid system with satisfactory effect on retardation, corrosion inhibition, scale inhibition, and scale removing through careful designs and detailed characteristic evaluation.

## 2. Design of High Temperature Multichelating Acid System

The multichelating acid system consists of  $H_3PO_4$ , SAV-1, SAV-2,  $NH_4F$ , and additives, with the organic phosphonic chelating agent SAV-1 and the anionic poly carboxylic acid chelating dispersant SAV-2. Using the weak acid to slow the releasing rate of hydrogen ion can decrease the HF concentration for retardation. Chelating agents and dispersants are utilized to prevent or decrease the generation of secondary precipitation. Even though floating particles and partial insoluble precipitation are formed, dispersant agent could distribute them in the reacted acid steadily, reducing the possibility of precipitating and plugging (the particular feature also possesses fine rate of metallic corrosion). pH value can be controlled within a certain range by using buffer solution, thus decreasing the amount of secondary precipitation.

The molecular structure of SAV-1 is as shown in Figure 1.

The molecular structure of SAV-2 is as shown in Figure 2.

## 3. Evaluation on Overall Performance of Multichelating Acid

### 3.1. Retardation Mechanism and Performance Evaluation

**3.1.1. Retardation Mechanism.** (1) The main function body of hydrofluoric acid is to unionize HF molecule instead of ionized  $F^-$  or  $HF^{2-}$ , and surface reaction is the affinity chemisorption of unionized HF molecule and aluminum silicate mineral lattice bond, rather than simply the substitution or generation of hydrogen bond [18, 19].

The consumption of hydrogen ions is fast, leading to a sharp rise of pH value, which results in hydrofluoric acid affected near borehole area only without further displacement into the formation. SAV-1 and SAV-2 in this claimed system gradually ionize hydrogen ions, and the post production can form a buffer solution to control pH value within a certain range to achieve retardation.

(2) Regular acid would be mostly consumed on clay surface for it is larger than other minerals, which causes ineffectively utilization of acid as well as destruction of rock framework.

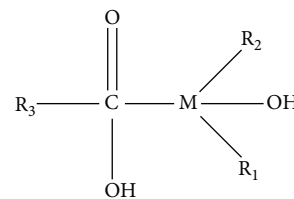


FIGURE 1: Molecular structure of SAV-1.

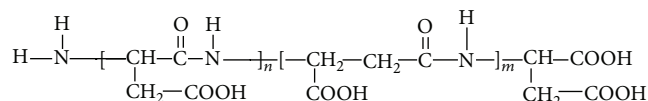


FIGURE 2: Molecular structure of SAV-2.

Due to the physical and chemical absorption effects of the multichelating acid, SAV-1 reacts easily with clay and fillers with higher calcium, iron, aluminum component, forming a thin film on clay surface, which can not only promote deeper acidizing but also maintain the integrity of rock framework. The thin film is less than  $1\ \mu\text{m}$  under SEM observation, with low solubility in weak acid and water but high dissolving rate in HCl, and it can retard the rapid reaction of clay and acid.

Figure 3 is the SEM comparison between montmorillonites before and after pictures with mud acid and multichelating acid. The results indicate that when reacted with multichelating acid for 5 minutes, a thin film was formed on the clay surface, which phenomena had not been seen from the mud acid experiment with montmorillonites.

(3) The addition organic phosphonic acid is an anionic phosphonate with a prominent feature of strong water-wettability. This feature may catalyze the reaction between fluorinated acid and quartz, making the initial low dissolving rate of quartz increased high as time extends, which is helpful to radial permeability improvement of deep formation. Researches demonstrate that this above acid treated clay mineral is agglomerated in toluene and easily dispersed in methanol, which indicates that the water-wet surface will not have bad effect on the reservoir and production of oil and gas development.

**3.1.2. Evaluation on Retardation Performance.** Mud acid ( $9\%HCl + 1.5\%HF$ ) and multichelating acid ( $5\%H_3PO_4 + 4\%SAV-1 + 1\%SAV-2 + 1.5\% NH_4F$ ) were used to react with sandstone minerals, whose composition was 35% quartz, 14% potassium feldspar, 13% albite, 6% dolomite, 2% kaolinite, 9.5% chlorite, 1% Illite, and 1.5% montmorillonite. Experiment temperature was  $95^\circ\text{C}$ , with 1g/10 mL solid-liquid ratio. The experiment results showed that the multichelating acid dissolving rate was far lower than that of mud acid in the early stage, while the dissolution rate of mud acid slightly changed and that of multichelating acid was gradually increased as time went on. After 4 hours of reaction, the dissolution rate of the multichelating acid was nearly equal to that of mud acid, which indicated the better retardation ability of multichelating acid. Therefore, the good retardation performance of multichelating acid prolongs the acid active

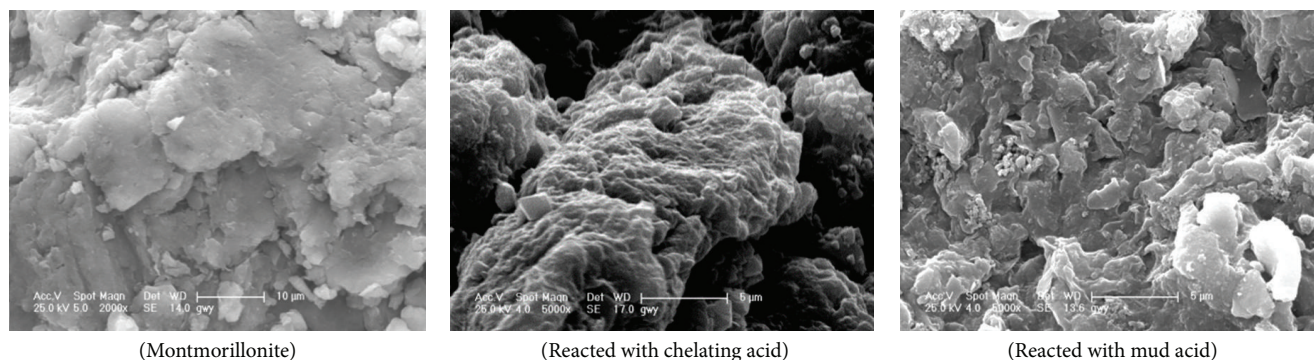


FIGURE 3: SEM of montmorillonite after the reaction with acid.

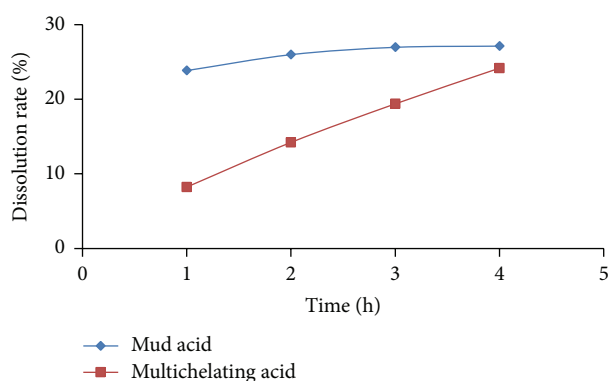


FIGURE 4: Rock-powder dissolving rate with mud acid and multichelating acid.

reaction time and extends the effective distance of acidizing. The results are shown in Figure 4.

**3.2. Corrosion Inhibition Mechanism and Performance Evaluation.** Under high temperature condition, the corrosion rate of acid directly affects the safety of acidizing treatment. The hydroxyl of SAV-1 molecule, where oxygen atom can form coordinate bond with iron ion or partially positive-charged iron atom on the iron surface because of unshared electron pair, thus forms an absorption precipitation layer. The layer covers the iron surface, preventing the diffusion of dissolved oxygen to the metal. Since precipitation membrane is more likely to form in alkaline environment, it inhibits the electrochemical corrosion of the cathodic reaction for  $\text{OH}^-$  ion generated faster on local cathode area of the precipitation membrane [20, 21]. Additionally, the extended methyl in SAV-1 to the outside of the membrane prevents the diffusion of dissolved oxygen to the metal and protects the metal from corrosion more effectively.

SAV-2 is a water-soluble polypeptide chain, elongated by peptide bond ( $-\text{CO}-\text{NH}-$ ). There are quite many polar groups, including carboxyl, carbon, and amino. The oxygen and nitrogen atoms in peptide contain plenty of lone pair electrons. The oxygen atoms in peptide involve  $\pi$  bond, absorbing with d atomic orbital and resulting in directional

arrangement of these polar groups on metal surface. However, the nonpolar groups produce great steric hindrance and impede the reduction reaction on cathode by diffusion of  $\text{O}_2$  and hence restrict the corrosion of anodic metal. Besides, SAV-2 has a strong chelating ability over many metal ions including ferric ion, decreasing the corrosion caused by depolarization reaction.

Table 1 lists the corrosion rate of steel, without corrosion inhibition agent, of multichelating acid and regular mud acid. The result shows that corrosion rate of mud acid is approximately 10 times of that with multichelating acid, which demonstrating the latter has better corrosion inhibition ability, decreasing the risk of treatment in high-temperature reservoir and lowering the demand for corrosion inhibition agent.

### 3.3. Scale Removing Mechanism and Performance Evaluation

**3.3.1. Sulfate Scales Inhibiting/Removing Mechanism and Performance Evaluation of Multichelating Acid System.** Carbonate scale can be easily removed by HCl, leaving sulfate scale to be the key technical problem. There are three steps during the growth and sedimentation of  $\text{CaSO}_4$  crystal, the process of forming oversaturated solutions: the generating of crystal nucleus, the growing of crystal nucleus, and the forming of crystal. Once any step is broken, the forming of scale would be inhibited or slowed down. The function of inhibitor is to control one or several steps to prevent precipitation. Compared with other acids, multichelating acid has advantage in precipitation inhibiting and removing ability.

**(1) Lattice Distortion.** In the growth of crystal, there exists vacancy, dislocation, and other lattice defect, or embedded structure distortion with the changing of external condition [22]. Each crystal plane develops unevenly in a single lattice. The spatial difference in crystal makes the crystal unstable and easy to break when the environment changes. The external reason can be mechanical failure and variation of oversaturation, but most importantly the change of chemical environment.  $\text{CaSO}_4$  contains ionic lattice, whose growth follows strict sequence. Only when a positive  $\text{Ca}^{2+}$  collides with negative  $\text{SO}_4^{2-}$  from another atom, the combination could happen. Therefore,  $\text{CaSO}_4$  scale is hard scale with

TABLE 1: Comparison of corrosion rate of multichelating acid and conventional mud acid.

	9% HCl + 1.5% HF	5% H <sub>3</sub> PO <sub>4</sub> + 4% SAV-1 + 1% SAV-2 + 1.5% NH <sub>4</sub> F
Before corrosion		
After corrosion		
Corrosion rate (g/m <sup>2</sup> ·h)	586.75	53.92
Conditions	Temperature: 120°C; time: 4 h	

certain direction and strictly sequential arrangement. Scale-inhibitor is absorbed on crystal, adulterating inside cell lattice, occupying the active point in polymer, which leads to a more serious distortion in the crystal further growth. Or inner stress raises, and large and irregular amorphous particle is formed, thus making the crystal easy to break, and growth is obstructed.

By comparing the SEM photos before and after the addition of SAV-1/SAV-2, an apparent shape change in crystal can be observed. Before adding SAV-1/SAV-2, the CaSO<sub>4</sub> crystal had sharp edges in regular form with smooth surface, where thin bands of crystal were arranged in a tight and ordered way (as shown in Figure 5). After adding SAV-1/SAV-2, the crystal form changed significantly, which had irregular form with shorter length, rough surface, and loose and disorderly arrangement; in addition, minor cracks appeared. The crystal experienced a serious distortion (as shown in Figure 6).

(2) *Chelating Solubility*. Crystallization is a phase transition process developed in the system microdomain. Besides electrostatic force, oversaturation of crystal material exists as reaction force. Crystallization can be divided into two steps: generation and growth of crystal nucleus. And the addition of inhibitor affects both processes.

SAV-2 structure formula mainly contains -COOH and -NHCO- functional groups, a liner polymeric scale inhibitor with concentration and anion characteristics. SAV-2 can form a stable chelate with Ca<sup>2+</sup> in water, thus lowering the oversaturation level of CaSO<sub>4</sub> and inhibiting formation of scale. Figure 7 is the sketch of this reaction.

SAV-1 dissociates H<sup>+</sup> and negatively charged phosphate group, -PO(OH)<sub>2</sub>, from water, and the latter group provides coordinate electron for Ca<sup>2+</sup> on CaSO<sub>4</sub> surface lattice, constituting chelate with a hexatomic ring. The chelate product has better solubility than that of calcium and magnesium salt; thus calcium and magnesium ions are stabilized in high concentrated chelate-bearing water, inhibiting scale deposition. The hexatomic ring structure formed by SAV-1 and Ca<sup>2+</sup> is shown in Figure 8.

Also, the acid radical negative anion can react with the Ca<sup>2+</sup> in formed crystals, making CaSO<sub>4</sub> microcrystals hard to arrange in strict lattice orders during collision process;

therefore large crystal is uneasy to form. Since solubility is improved for the remaining small grain range of crystals, the multichelating acid also inhibits CaF<sub>2</sub> secondary precipitation effectively based on the same mechanism.

(3) *Electrostatic Interaction*. SAV-1/SAV-1 dissociates polyaspartic ion, organic phosphonic ion, and hydrogen ion from water, the nitrogen atoms in these acid radical anion and molecule, plus the oxygen atom in carboxyl and phosphine group, resulting in gathered potential scaling microcrystals and repulsed to each other due to the same negative charge (as shown in Figure 9). Therefore, the collision among, the formation of large crystals, the conduction between microcrystals and metal transmission surface and the formation and growth of scale have all been hindered.

X-ray diffraction (XRD) is another effective way to study the growth of crystal. When electron rays beams illuminate on a sample, the components trigger multiple X-rays with corresponding features. Among these emitted rays, angles exist between the X-rays and crystal surface satisfying the Prague diffraction condition. The comparison of the diffraction intensity, variation of diffraction angle, crystal axis and other parameters of the scaling samples' X-ray diffraction diagrams, indicating the variations in the degree of fragment, degree of distortion and crystal system with or without scaling inhibitor [23, 24]. Figures 10 and 11 show the XRD diagrams before and after adding SAV-1/SAV-2 into the CaSO<sub>4</sub> scale.

Generally, there are three forms of CaSO<sub>4</sub> scale: gypsum (calcium sulfate carrying two crystalline water particles), calcium sulfate hemihydrate, and anhydrous calcium sulfate. Comparing Figures 10 and 11 with standard XRD diagram, it is certain that crystal type of both samples is gypsum, which belongs to monoclinic system.

It can be spotted from the figures that the diffraction angles before and after adding SAV-1/SAV-2 are almost the same (shown in Table 2), but at some certain diffraction angles the X-rays' relative intensity has changed. After adding SAV-1/SAV-2, the unit cell constant has ascended compared with the straight calcium sulfate (shown in Table 3). The enlargement of unit cell size also demonstrates the entre of SAV-1/SAV-2 or absorption on the crystal surface in crystallization of calcium sulfate, which makes the unit cells

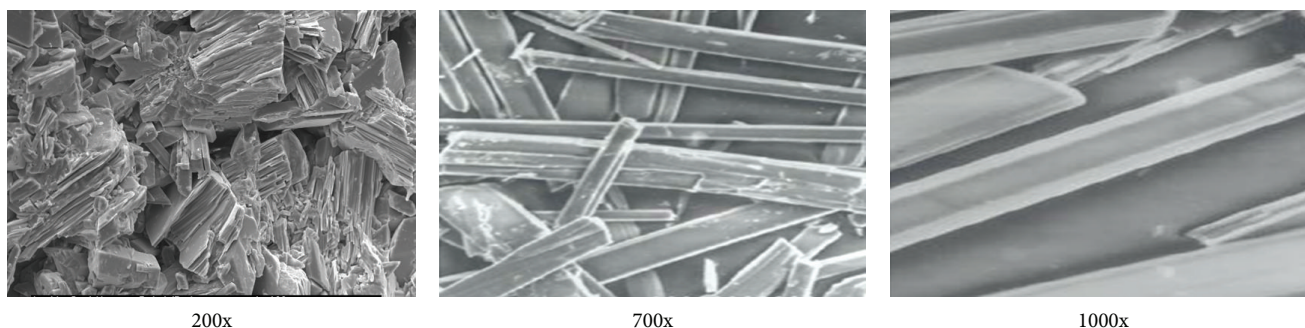


FIGURE 5: Plank and pillar-like gypsum crystal before SAV-1/SAV-2 treatment. \* Annotation: 200x, 700x, and 1000x are the magnification under observation.



FIGURE 6: Plank and pillar-like gypsum crystal after SAV-1/SAV-2 treatment.

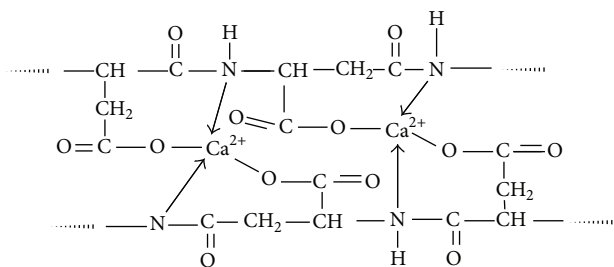


FIGURE 7: Chelating reaction of SAV-2 and  $\text{Ca}^{2+}$ .

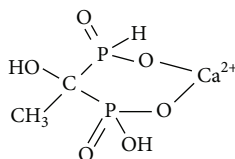


FIGURE 8: Chelating reaction of SAV-1 and  $\text{Ca}^{2+}$ .

of calcium sulfate accumulate in an irregular way; thus different forms are observed.

Based on crystallization spiral dislocation theory [25], the points of increasing activity are limited, and when dislocation occurs after active points react with scale-inhibiting agent, continuous growth is obstructed. Hence, even a low concentration of scale-inhibiting agent can inhibit the generating of crystal, thus inhibiting the formation of  $\text{CaSO}_4$ .

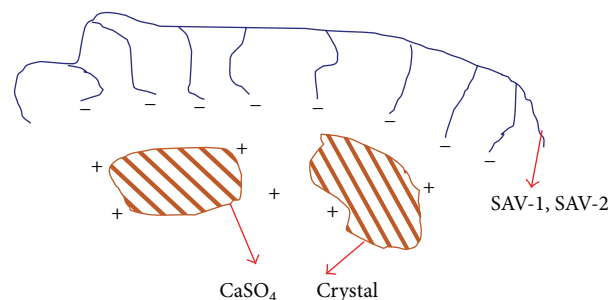


FIGURE 9: Intercrystalline electrostatic repelling effect.

### 3.3.2. Silica Gel Precipitation Inhibition Mechanism and Performance Evaluation

#### (1) Mechanism of Inhibiting Silica Gel Precipitation

(a) *Effects on Surface Properties of Silicon Polymers.* Due to physical or chemical effects, scale inhibiting dispersing agent after ionization into anionic will obtain strong absorptive capability. The anions are absorbed on the surface of silicon polymers, changing the physical and chemical properties of silicon polymers' surface, making them acquire same negative charges and causing mutual electrostatic repulsion between particles. These reactions avoid accumulated growth of silicon polymers, suspend disperse particles in water, and

TABLE 2: Comparisons of diffraction data of  $\text{CaSO}_4 \cdot 2\text{H}_2\text{O}$ .

	Peak number	$D$ ( $10^{-10}$ m)	$2\theta$	$h$	$l$	$k$
Straight crystal	1	7.58121	11.6731	0	2	0
	2	4.2811	20.7488	1	2	1
	4	3.06593	29.127	0	0	2
After treatment of SAV-1/SAV-2	1	7.61214	11.6762	0	2	0
	2	4.32105	20.7504	1	2	1
	4	3.13434	29.1294	0	0	2

TABLE 3: Unit cell constant of  $\text{CaSO}_4 \cdot 2\text{H}_2\text{O}$ .

Samples	$a$ ( $10^{-10}$ m)	$b$ ( $10^{-10}$ m)	$c$ ( $10^{-10}$ m)
Standard	5.68	15.18	6.51
Straight	5.67	15.13	6.51
After treatment of SAV-1/SAV-2	5.71	15.27	6.54

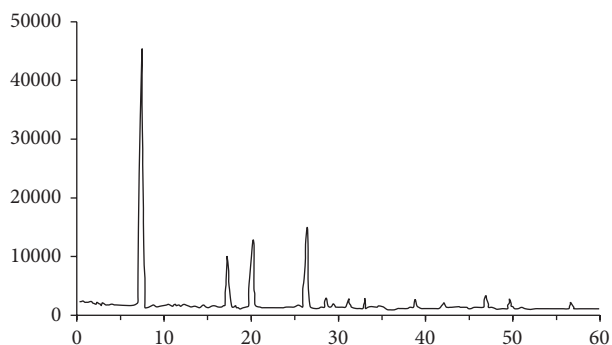


FIGURE 10: XRD diagram before adding SAV-1/SAV-2.

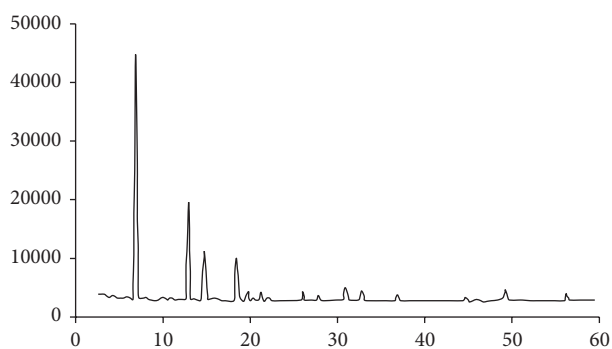


FIGURE 11: XRD diagram after adding SAV-1/SAV-2.

block the silicon polymerization from single to dimer or multimer [26]. Meanwhile, with the negatively charged inhibiting dispersant scale agent absorbed on silicon polymers surface, silicon polymers are unlikely to form silicate scales by losing water with the enhanced hydrophilic.

(b) *Dispersion Effects on Silicon Polymers.* When an anion of scale inhibitor dispersing agent absorbs one or more silicon polymers, same electronic charge as the anion is with electrostatic repulsion, which prevents collision and the formation of polymers. It is known as flocculation of polymer anion and

crystalloid particles, which makes crystalloid be absorbed on polymer chains and also gathers the potential scaling crystalloids to a certain extent [27]. When the products of absorption meet other copolymer molecules or diffuse to a relatively high concentration of polymers area, they offer the absorbed particles to other polymer molecules and finally form a state of balance. This is the dispersion effect on flocculated crystalloids by polymer anion. By such effect of flocculation and dispersion, silicon polymers could keep suspension in aqueous solution stably.

(2) *Evaluation of Scale Inhibition Capability.* Using  $\text{Na}_2\text{SiO}_3 \cdot 9\text{H}_2\text{O}$  to prepare 2 kinds of solution during the experiments as comparison (Solution 1, the concentration of silicon ion is 4000 mg/L, containing 1.5 mL SAV-1 and 0.5 mL SAV-2; Solution 2, the concentration of silicon ion is 2000 mg/L without chelating agent), volumes of both solutions are 50 mL, with 2.5 pH value. These two kinds of solutions were heated in water bath under 95°C; after cooling down and filtering, molybdenum blue photometric method was used to measure the content of silicon ion and weight method was used to measure the amount of silica gel precipitate. The results are shown in Table 4.

The results in Table 4 demonstrate the great inhibiting capability of chelating agent of the formation of silica gel precipitate. Moreover, by comparing the standard silicon ion solution before and after chelating agent addition (as shown in Figure 12), observation shows that the sample precipitates a lot after 30 minutes of heating without chelating agent, and the amount of precipitation increases with the heating time. However, though the sample with chelating agent has a high concentration of silicon ion, the solution still remains transparent after 90 minutes of heating. Precipitate appears after heating for 120 minutes and becomes turbid.

3.3.3. *Mechanism of Inhibiting Fluosilicate Precipitation.* When sandstone reservoir is treated by HF acid system or other acid systems where HF is produced during the process, the primary reaction between HF and aluminosilicate produces fluosilicic acid, whose reaction with  $\text{Na}^+$ ,  $\text{K}^+$ ,  $\text{Ca}^{2+}$

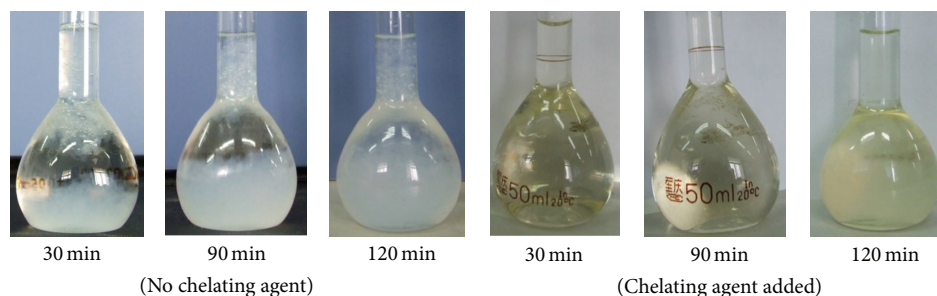


FIGURE 12: Comparison of chelating agent added before and after in Si ion standard solution.

TABLE 4: Chelating agent's effect on silica gel precipitate.

Sample	30 min		90 min		120 min	
	Concentration of Si (mg/L)	Amount of silica gel precipitate (mg)	Concentration of Si (mg/L)	Amount of silica gel precipitate (mg)	Concentration of Si (mg/L)	Amount of silica gel precipitate (mg)
No chelating agent (2000 mg/L)	1243.12	129.48	765.29	211.22	586.44	241.82
Chelating agent added (4000 mg/L)	3810.63	32.39	3613.13	66.18	3020.63	167.54

in formation water caused reservoir damage by generated silicofluoride precipitation. The mechanism of silicofluoride precipitation inhibition by multichelating agent is basically the same as that of silica gel precipitation inhibition. Generally speaking, organic phosphonic acid has better absorption capability than polycarboxylate acid on crystalloid surface, with a relatively poor dispersion capability. Therefore, by combining chelating agent and chelating dispersant, the inhibition effect on potassium (or sodium) fluorosilicate crystallization can be enhanced, improving scale inhibiting effect [28, 29].

To evaluate the effect of acid on silicofluoride precipitation inhibition, scale inhibiting effect evaluation experiments were conducted [30].

Four kinds of solutions were prepared for comparison experiments: Solution 1: concentration of  $\text{Na}^+$  is 0.25 mol/L (or concentration of  $\text{K}^+$  is 0.25 mol/L), and concentration of fluosilicic acid is 0.25 mol/L, no scale inhibitor contained. Solution 2: concentration of  $\text{Na}^+$  is 0.25 mol/L (or concentration of  $\text{K}^+$  is 0.25 mol/L), and concentration of fluosilicic acid is 0.25 mol/L, containing 12.5 mL inhibitor SAV-1 (10 mg/mL). Solution 3: concentration of  $\text{Na}^+$  is 0.25 mol/L (or concentration of  $\text{K}^+$  is 0.25 mol/L), and concentration of fluosilicic acid is 0.25 mol/L, containing 12.5 mL inhibitor SAV-2 (10 mg/mL). Solution 4: concentration of  $\text{Na}^+$  is 0.25 mol/L (or concentration of  $\text{K}^+$  is 0.25 mol/L), and concentration of fluosilicic acid is 0.25 mol/L, containing 12.5 mL mixed inhibitor of SAV-1 (5 mg/mL) and SAV-2 (5 mg/mL).

Stainless steel pieces were immersed in beakers filled with 1000 mL of the four solutions separately. After 12 hours of heating in water bath at 50°C, those pieces were taken out, dried, and weighted.

TABLE 5: Experimental results of scale inhibitor on the inhibition of sodium fluosilicate precipitation.

Scale inhibitor	Scale weight (g)	Scale inhibition ratio (%)
Comparing sample	0.1742	—
SAV-1	0.1536	11.81
SAV-2	0.0582	67.57
SAV-1 + SAV-2 (1:1)	0.0632	63.74

Formulation of the scale inhibition ratio is as follows:

$$\eta = \frac{G_1 - G_2}{G_1} \times 100\% \quad (1)$$

In this formulation,  $G_1$  is the weight of stainless steel piece without scale inhibitor addition (g);  $G_2$  is the weight of stainless steel piece with scale inhibitor addition (g);  $\eta$  is the scale inhibition ratio (%).

Table 5 indicates that SAV-2 or the mixture of SAV-1 and SAV-2 has relatively strong inhibiting capability to fluosilicate precipitation.

#### 4. Conclusion

(1) The concentration of unionized HF could be reduced to achieve retardation by decreasing the concentration of  $\text{H}^+$  in acid; the use of synergic method of chelation and dispersion could prevent/reduce the generation of secondary precipitation; pH value controlled at a certain range with

buffer solution could partially decrease secondary precipitation; therefore a new acid system is devised:  $\text{H}_3\text{PO}_4 + \text{SAV-1} + \text{SAV-2} + \text{NH}_4\text{F}$ .

(2) Experiments indicate that chelating acid has good performance on retardation and dissolution capability.  $\text{H}_3\text{PO}_4$  and SAV-1 can slowly ionize  $\text{H}^+$ ; meanwhile the reactant of SAH and SAV-1 can function as buffer solution, which controls pH value and HF concentration within a certain range to achieve retardation. SAV-1 in acid slows the reaction rate by chemical and physical absorption.

(3) It has been verified that high temperature multichelating acid shows great corrosion inhibition performance, and a few corrosion inhibitors could meet the requirement of acidizing treatment. SAV-1 is a cathodic corrosion inhibitor, mainly focusing on inhibiting cathodic corrosion, while SAV-2 is able to impede the anodic corrosion, and there exists associated corrosion inhibition effect of these two.

(4) The chelating agents SAV-1 and chelating dispersant SAV-2 of high temperature multichelating acid could eliminate sulfate scale, whose mechanisms are lattice distortion, chelating solubilization, and electrostatic interaction.

(5) Multichelating acid effectively inhibits the formation of secondary precipitation of fluosilicate, silica gel, and so forth, whose mechanisms are the surface properties' change and dispersion effect on silicon polymers by the effect of SAV-2 and SAV-1. Since the chelating solubilization of multichelating acid system can inhibit the precipitation of  $\text{CaF}_2$ , potential secondary damage can be eliminated effectively during acid treatment.

## Conflict of Interests

The authors declare that there is no conflict of interests regarding the publication of this paper.

## Acknowledgments

The authors wish to thank the management of Southwest Petroleum University and PetroChina Changqing Oilfield Company, for their permission to publish this paper and their assistance in applying these new techniques. Thanks are also to Lu Zhang and Zhi Li for their help with paper.

## References

- [1] E. P. da Motta, B. Plavnik, R. S. Schechter, and A. D. Hill, "Accounting for silica precipitation in the design of sandstone acidizing," *SPE Production and Facilities*, vol. 8, no. 2, pp. 138–144, 1993.
- [2] E. C. Shuchart and R. D. Gdanski, "Reducing aluminum compound precipitation following subterranean formation acidizing," U.S. Patent no. 6,531,427, 2003.
- [3] R. L. Thomas, H. A. Nasr-El-Din, J. D. Lynn, and S. Mehta, "Precipitation during the acidizing of a HT/HP illitic sandstone reservoir in eastern Saudi Arabia: a laboratory study," in *Proceedings of the SPE Annual Technical Conference and Exhibition*, Society of Petroleum Engineers, pp. 3239–3254, October 2001.
- [4] S. A. Ali, C. W. Pardo, Z. Xiao et al., "Effective stimulation of high-temperature sandstone formations in East Venezuela with a new sandstone acidizing system," in *Proceedings of the SPE International Symposium and Exhibition on Formation Damage Control*, Society of Petroleum Engineers, 2006.
- [5] N. Kume and R. van Melsen, "New HF acid system improves sandstone matrix acidizing success ratio by 400% over conventional mud acid system in Niger Delta Basin," in *Proceedings of the SPE Annual Technical Conference and Exhibition*, SPE 56527, 1999.
- [6] M. W. Bodine Jr. and T. H. Fernald, "Edta dissolution of gypsum, anhydrite, and Ca-Mg carbonates," *Journal of Sedimentary Research*, vol. 43, no. 4, pp. 1152–1156, 1973.
- [7] T. N. Tyler, R. R. Metzger, and L. R. Twyford, "Analysis and treatment of formation damage at Prudhoe Bay, Alaska," *Journal of Petroleum Technology*, vol. 37, no. 7, pp. 1010–1018, 1985.
- [8] M. A. Sayed, H. A. Nasr-Ei-din, and C. A. de Wolf, "Emulsified chelating agent: evaluation of an innovative technique for high temperature stimulation treatments," in *Proceedings of the SPE European Formation Damage Conference and Exhibition*, pp. 385–404, Society of Petroleum Engineers, June 2013.
- [9] B. G. Al-Harbi, N. M. Al-Dahlan, and M. H. Al-Khaldi, "Evaluation of chelating-hydrofluoric systems," in *Proceedings of the International Petroleum Technology Conference (IPTC '13)*, 2013.
- [10] G. D. Dean, C. A. Nelson, S. Metcalf, R. Harris, and T. Barber, "New acid system minimizes post acid stimulation decline rate in the Wilmington Field, Los Angeles County, California," in *Proceedings of the SPE Western Regional Meeting*, SPE-46201-MS, Bakersfield, Calif, USA, May 1998.
- [11] M. A. Mahmoud, A. H. Nasr-El-Din, C. de Wolf, J. N. LePage, and J. H. Bemelaar, "Evaluation of a new environmentally friendly chelating agent for high-temperature applications," in *Proceedings of the International Symposium and Exhibition on Formation Damage Control*, Society of Petroleum Engineers (SPE '10), Lafayette, La, USA, February 2010.
- [12] J. N. LePage, C. A. de Wolf, J. H. Bemelaar, and H. A. Nasr-El-Din, "An environmentally friendly stimulation fluid for high-temperature applications," *SPE Journal*, vol. 16, no. 1, pp. 104–110, 2011.
- [13] W. Frenier, M. Rainey, D. Wilson, D. Crump, and L. Jones, "A biodegradable chelating agent is developed for stimulation of oil and gas formations," in *Proceedings of the SPE/EPA/DOE Exploration and Production Environmental Conference*, SPE-80597-MS, Society of Petroleum Engineers, San Antonio, Tex, USA, March 2003.
- [14] W. Frenier, D. Wilson, D. Crump et al., "Use of highly acid-soluble chelating agents in well stimulation services," in *Proceedings of the SPE Annual Technical Conference and Exhibition*, Society of Petroleum Engineers, 2000.
- [15] M. A. Mahmoud, H. A. Nasr-El-Din, C. A. de Wolf, and A. K. Alex, "Sandstone acidizing using a new class of chelating agents," in *Proceedings of the International Symposium on Oil-field Chemistry*, Society of Petroleum Engineers, pp. 1–17, April 2011.
- [16] A. H. A. Ali, W. W. Frenier, Z. Xiao, and M. Ziauddin, "Chelating agent-based fluids for optimal stimulation of high-temperature wells," in *Proceedings of the SPE Annual Technical Conference and Exhibition*, Society of Petroleum Engineers, 2002.
- [17] S. A. Ali, E. Ermel, J. Clarke, M. J. Fuller, Z. Xiao, and B. P. Malone, "Stimulation of high-temperature sandstone formations from West Africa with chelating agent-based fluids," *SPE Production and Operations*, vol. 23, no. 1, pp. 32–38, 2008.
- [18] L.-M. Zhang, "Type for hydrofluoric acid dissolution effect of montmorillonite clay," *Drilling Fluid and Completion Fluid*, vol. 10, no. 5, pp. 28–32, 1993.

- [19] L.-M. Zhang, "Effect of hydrochloric acid in mud acid through sandstone acidizing," *Oil Drilling & Production Technology*, vol. 16, no. 6, pp. 51–57, 1994.
- [20] S.-G. Zhang, *Theoretical study on the operation mechanism of scale and corrosion inhibitors [Ph.D. thesis]*, 2006.
- [21] C.-W. Cui, S.-F. Li, H. Yang et al., "Study of corrosion inhibitors PBTCA, HEDP and ATMP," *Materials Science & Technology*, vol. 14, no. 6, pp. 605–611, 2006.
- [22] Y. Q. Zheng, E. W. Shi, W. J. Li, B. G. Wang, and X. F. Hu, "Research and development of the theories of crystal growth," *Journal of Inorganic Materials*, vol. 14, no. 3, pp. 321–331, 1999.
- [23] Y.-X. Yang, *X-Ray Diffraction Analysis*, Shanghai Jiao Tong University Press, 1989.
- [24] T.-S. Li, *Foundation of Crystal X-ray Diffraction Study*, Metallurgical Industry Press, 1990.
- [25] N. M. Min, *Physical Foundation of Crystal Growth*, Shanghai Science Technology Press, 1982.
- [26] J. Li and Z.-Y. Lin, "A Study on Scale Inhibiting Mechanism of HEDP Based on Molecule Simulation," *Journal of Tongji University (Science and Technology)*, vol. 34, no. 4, pp. 518–522, 2006.
- [27] Y.-X. Cao, J. Yang, and J. Li, "Study of inhibition HEDP and PBTCA," *Journal of Tongji University*, vol. 32, no. 4, pp. 556–560, 2004.
- [28] L.-J. Yang, Y.-X. Zhang, and Y.-H. Huang, "Effect of scale inhibitor-dispersant on the crystallization of potassium (sodium) fluosilicate," *Chemical Industry and Engineering*, vol. 19, no. 1, pp. 1–5, 2002.
- [29] Y. Lin-jun and Z. Yun-xiang, "Kinetics of growth of potassium (Sodium) fluosilicate crystal," *Chemical Engineering*, vol. 30, no. 2, pp. 15–18, 2002.
- [30] G.-N. Feng, Y.-E. Chen, H.-L. Zhu, Y.-Q. Li, R. Zu, and H.-Q. Tang, "An improvement in complexometric titration for evaluating the efficiency of scale inhibitors," *Oilfield Chemistry*, vol. 21, no. 3, pp. 284–286, 2004.

## Research Article

# A Review on Homogeneous Charge Compression Ignition and Low Temperature Combustion by Optical Diagnostics

Chao Jin<sup>1</sup> and Zunqing Zheng<sup>2</sup>

<sup>1</sup>School of Environmental Science and Engineering, Tianjin University, Tianjin 300072, China

<sup>2</sup>State Key Laboratory of Engines, Tianjin University, Tianjin 300072, China

Correspondence should be addressed to Zunqing Zheng; zhengzunqing@tju.edu.cn

Received 13 January 2015; Revised 18 May 2015; Accepted 20 May 2015

Academic Editor: João Paulo Leal

Copyright © 2015 C. Jin and Z. Zheng. This is an open access article distributed under the Creative Commons Attribution License, which permits unrestricted use, distribution, and reproduction in any medium, provided the original work is properly cited.

Optical diagnostics is an effective method to understand the physical and chemical reaction processes in homogeneous charge compression ignition (HCCI) and low temperature combustion (LTC) modes. Based on optical diagnostics, the true process on mixing, combustion, and emissions can be seen directly. In this paper, the mixing process by port-injection and direct-injection are reviewed firstly. Then, the combustion chemical reaction mechanism is reviewed based on chemiluminescence, natural-luminosity, and laser diagnostics. After, the evolution of pollutant emissions measured by different laser diagnostic methods is reviewed and the measured species including NO, soot, UHC, and CO. Finally, a summary and the future directions on HCCI and LTC used optical diagnostics are presented.

## 1. Introduction

Homogeneous charge compression ignition (HCCI), as a new combustion mode in internal combustion engines, has been widely studied in recent 20 years. At first, the HCCI means a homogeneous charge formed by port-injection or in-cylinder early-injection is autoignited as the temperature and pressure are high enough in the cylinder. Noguchi et al. [1] investigated the HCCI combustion process by a spectroscopic system in 1979 and found that the combustion chemical radicals were detected subsequently. For example, CHO, HO<sub>2</sub>, and O radicals were first detected, followed by CH, C<sub>2</sub>, and H radicals, and finally was the OH radical. This combustion process was different to the conventional gasoline engines where all radicals were observed nearly at the same time. This study work confirms that the HCCI should be initiated by the autoignition of premixed mixture due to the compression. After that, with the development of HCCI, more optical diagnostic technologies are applied to study this new combustion process. Meanwhile, researchers find that although HCCI can achieve low NO<sub>x</sub> and soot emissions and high efficiency, the operation range is limited

and the control on autoignition timing is difficult compared to conventional diesel and gasoline engines. Therefore, some new strategies, such as active stratification on temperature and charge, changes of fuel properties, and different injection strategies, are used to solve the disadvantages of HCCI. More new combustion models, such as premixed charge combustion ignition (PCCI) and diesel low temperature combustion (LTC), have been developed. In fact, all these new combustion modes are dominated by the chemical reaction kinetics, and the combustion emits low NO<sub>x</sub> and soot emissions, but high UHC and CO emissions.

In previous HCCI and LTC review papers, such as papers by Yao et al. [2], Dec [3], Musculus et al. [4], and Komninos and Rakopoulos [5], they have introduced that how to extend the HCCI and LTC operating range and to control the autoignition timing. In this paper, we will focus on the physical and chemical reaction processes in HCCI and LTC by measurements of optical diagnostics, which will help readers to understand the combustion processes in HCCI and LTC and to use different optical techniques to study new combustion models.

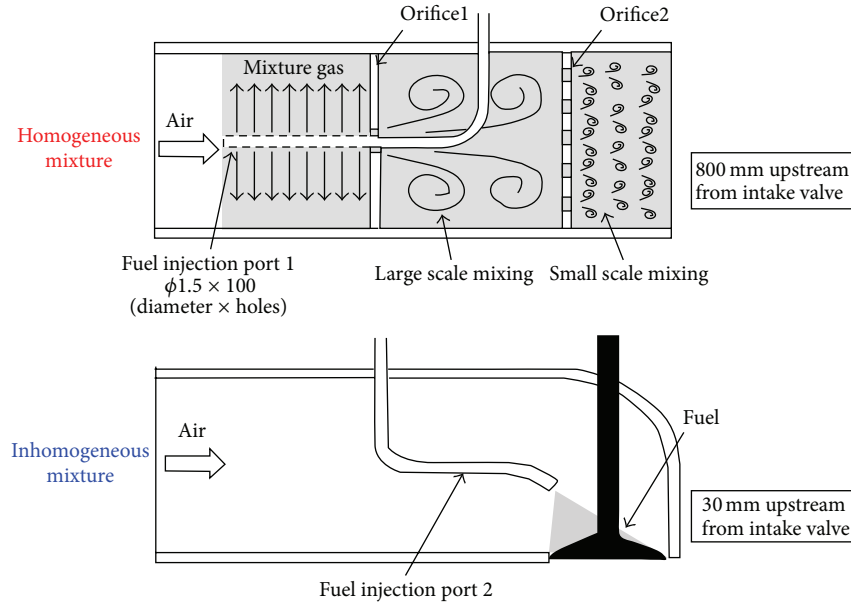


FIGURE 1: The different mixing process in the manifold [8].

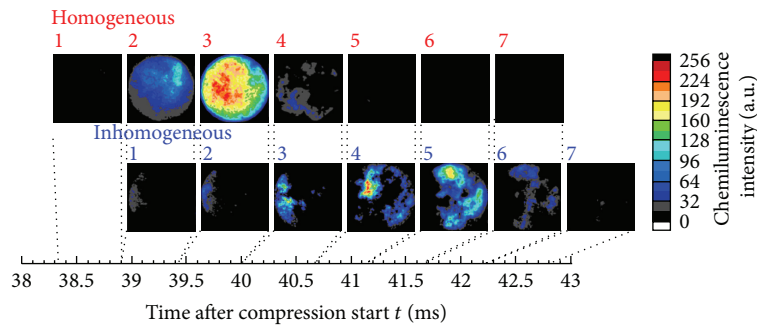


FIGURE 2: Chemiluminescence images with different mixing process [8].

## 2. Optical Diagnostics for In-Cylinder Mixture Formation

The mixture formation of fuel and air is physical process, but it has large effect on combustion chemistry subsequently. Therefore, the mixing process is reviewed firstly based on both port-injection and in-cylinder direct-injection. Finally, mixture formation combined by port and in-cylinder injection will also be reviewed.

*2.1. Mixture Formation by Port Injection.* Although the fuel distribution in the HCCI engine is homogeneous in macroscopically due to a quite long premixed time, the inhomogeneity in fuel distribution and temperature is lying in microscopically and thus may affect the autoignition and subsequent combustion process. Richter et al. [6] investigated the images of fuel/air mixture by using planar laser induced fluorescence (PLIF) in a HCCI engine. Two different pre-mixing procedures were used to obtain different degrees of homogeneity of the fuel/air charge. One was a standard port injection to form the premixed charge, and the other was

an additional preheated mixing tank of 20 liters to prepare a more homogenous charge. The PLIF measurement confirmed that different fuel preparation strategies affected the fuel/air homogeneity and the spatial variations of the combustion process. In the further study [7], Richter et al. found that even if the PLIF results presented a high degree of homogeneity, they were still lying in local inhomogeneous fluctuations by the measurements of Raman scattering which was caused by cycle-to-cycle variations.

Kumano et al. [8] investigated the effects of charge inhomogeneity on the HCCI combustion process. The chemiluminescence images were obtained by using a framing camera on an optical engine and dimethyl ether (DME) was used as a test fuel. The designed device was fixed into more upstream of intake manifold to form more homogeneous charge as shown in Figure 1, which was used to compare with the inhomogeneous charge. The whole combustion processes under homogeneous and inhomogeneous mixture have been shown in Figure 2. It could be seen that the combustion duration got longer at inhomogeneous mixture and thus resulted in a moderate heat release and lower maximum

pressure rise rate. However, the homogeneous charge formed a very fast combustion process. Therefore, they concluded that the HCCI needed a local moderate combustion but not overall combustion in the cylinder.

*2.2. Mixture Formation by In-Cylinder Injection.* In fact, more optical diagnostics for in-cylinder mixture formation is focus on the direct injection. For extending the HCCI operating range at high load and controlling the autoignition timing, some researchers introduce stratification in the cylinder but do not form quite homogeneous charge. In order to distinguish the HCCI, some new terms, such as stratification charge compression ignition (SCCI) [9–12] and premixed charge compression ignition (PCCI) [13–18], are used. Meanwhile, in recent 10 years, high EGR dilution low temperature combustion (LTC) [19–26] have been studied widely in diesel engines due to the fact that it is more practical than HCCI. All in all, all of these combustion modes need direct-injection and thus the mixture preparation is more complicated than that of port-injection.

Musculus [19] investigated the in-cylinder spray and mixing processes at LTC conditions and the oxygen concentration was 12.7%. The optical engine operated at low load of 4-bar indicated mean effective pressure (IMEP). The start of injection (SOI) was set to  $-22^{\circ}\text{CA}$  ATDC and both naturally aspirated and low boost pressure at 1.34 bars were tested. Mie scattering was used to present liquid-fuel penetration, while fuel fluorescence was used to measure the vapor jet. The results have been shown in Figure 3. It can be seen that the maximum liquid-fuel penetration was between 45 and 50 mm for the naturally aspirated condition and 40 and 45 mm for the low-boost condition. However, the typical liquid-fuel penetration was about 25 mm at conventional diesel conditions [27, 28]. In this work, the early-injection conditions resulted in lower ambient gas density and temperature than that of near top dead center (TDC) injection in the conventional diesel combustion. The longer penetration made the fuel impinge on the piston bowl and resulted in wetting of the piston.

Kashdan et al. [29] investigated the in-cylinder mixture distribution in an optically accessible direct-injection HCCI engine. A high-pressure common-rail injection system supplied 1100-bar injection pressure. The nozzle has 6 holes nozzle with a narrow angle (less than  $70^{\circ}$ ). Planar laser induced exciplex fluorescence (PLIEF) imaging was used in this study, which allowed qualitative visualization of the mixture (liquid and vapor phase) distribution within the piston bowl through the use of exciplex forming dopants. They found that as the start of injection (SOI) was  $-40^{\circ}\text{CA}$  ATDC, liquid fuel typically appears  $2^{\circ}\text{CA}$  later. At  $-33^{\circ}\text{CA}$  ATDC, the liquid fuel impinges on the piston face whilst the corresponding vapor phase images acquired at this crank angle degree. At  $-30^{\circ}\text{CA}$  ATDC, a certain degree of fuel stratification and a fuel rich region was seen in the center of the piston bowl due to fuel impingement. Further, this stratification trend was intensified with the retard of injection timings.

Fang et al. [30–32] investigated the liquid spray evolution process by Mie scattering and the combustion processes in a high-speed direct inject (HSDI) diesel engine. Keeping the

IMEP constant, the injection timing was changed from  $-40^{\circ}$  to  $-80^{\circ}\text{CA}$  ATDC for both conventional wide angle injector and narrow angle injector to form the homogeneous charge. At  $-40^{\circ}\text{CA}$  ATDC injection, the air density and temperature were higher and liquid spray tip impinged on the bowl wall and there was only a little fuel film on the bowl wall and thus the poor fire area was quite small. However, at  $-80^{\circ}\text{CA}$  ATDC injection, the liquid spray impinged on the piston top and some fuel collided with the cylinder liner and then flowed into the crankcase without combustion, which would worsen fuel economy and dilute oil. Although the narrow angle injector could reduce the fuel deposited on the liner, the narrow angle injector could also lead to fuel-wall impingement on the bowl wall and subsequent pool fires. The similar wall wetting was also observed by other study works, such as Liu et al. [33] and Kiplimo et al. [34].

Steeper and de Zilwa [35] investigated two gasoline direct injection (GDI) injectors on a HCCI engine at the stratified low-load condition. One injector has 8 holes with  $70^{\circ}$  spray angle and the other is a  $53^{\circ}$ -degree swirl injector. The Mie scattering and LIF were used to measure the spray development and fuel distributions and the results showed that probability density function (PDF) statistics of equivalence ratio distribution were similar for two injectors, but the 8-hole injector produced smaller and more numerous fuel packers than that of swirl injector.

Liu et al. [36] investigated spray penetration under different ambient temperatures (700–1000 K) covering both conventional diesel combustion and LTC conditions. Results showed that the liquid penetration lengths were reduced due to the heating caused by the downstream combustion flames. Compared to higher ambient temperatures, the lower ambient temperature had smaller effects on liquid penetration length, as shown in Figure 4. Furthermore, compared to soybean biodiesel, n-butanol spray only had a little change on liquid penetration length, which should be due to the longer soot lift-off for n-butanol spray flames.

*2.3. Mixture Formation Combined by Port and In-Cylinder Injection.* Recently, the dual-fuel injection combined by port and in-cylinder has been studied widely to achieve high efficiency and clean combustion [37–42]. By this dual-fuel injection, the homogeneous mixture can be formed by port injection using high volatility fuels, while the in-cylinder injection is used to form different stratification in the cylinder by changing injection timings. In addition, in dual-fuel injection system, two fuels with opposite autoignition characteristics, such as one high octane number and the other low octane number fuel, can form different fuel reactivity in the cylinder, which can also control autoignition and extend operating range of high efficiency and clean combustion. The optical diagnostics on mixing formation in dual fuel injection are limited and Figure 5 presents charge stratification and reactivity stratification studied in [37].

From what has been discussed, it can be concluded that the direct-injection strategy has more advantages than that of port-injection for HCCI autoignition control and operating range extending. However, as using early direct-injection strategy, it helps to form a more uniform air-fuel mixture

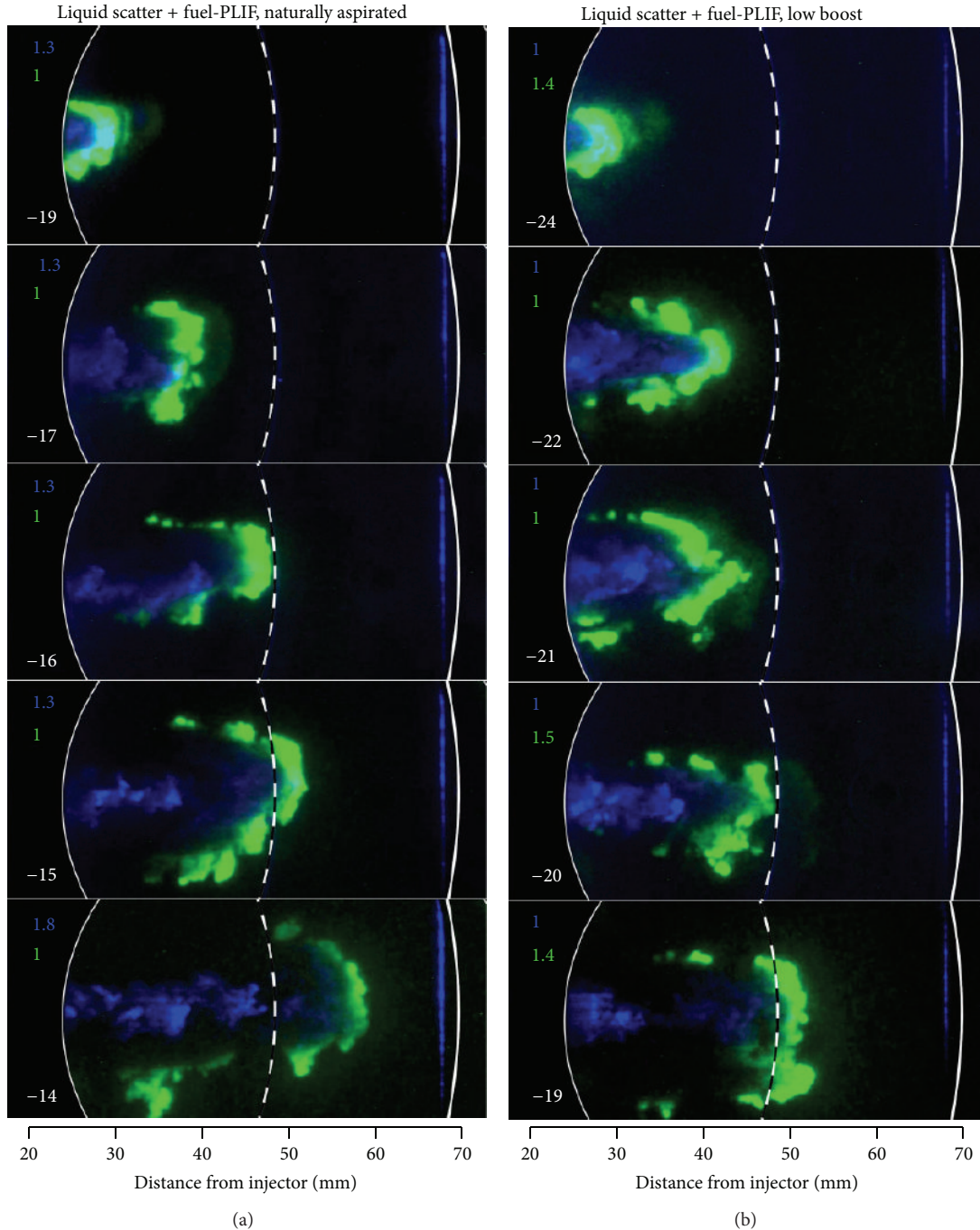


FIGURE 3: Liquid fuel (blue) and vapor fuel perimeter (green) for naturally aspirated (a) and low-boost (b) conditions (the dashed line is the edge of piston bowl-rim) [19].

before ignition but fuel can impingement on the piston head or the cylinder liner and results in wall-wetting and the dilution of oil. Some optimized methods have been carried out, such as using the narrow angle injector [30–32], 2-stage or multistage injection [18, 43, 44], and super high injection pressures [45, 46] and the reader can find detailed improvement for mixing processes based on these references.

### 3. Optical Diagnostics for Chemical Reaction Processes

*3.1. Chemiluminescence Imaging/Natural-Luminosity and Spectral Analysis.* As stated in [47], chemiluminescence often starts from low temperature combustion due to relaxation of the excited combustion radicals to their ground

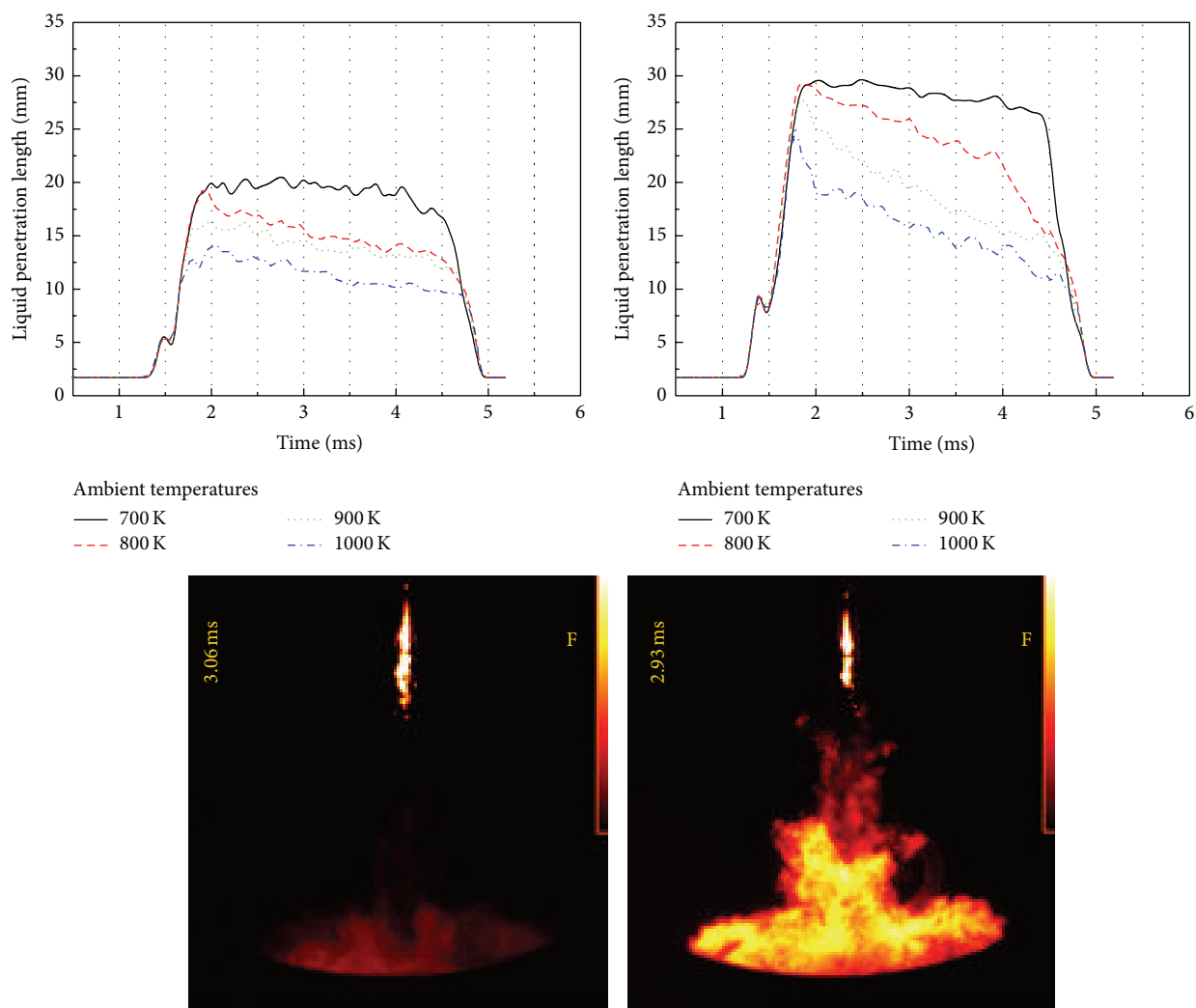


FIGURE 4: Liquid penetration lengths at different ambient temperatures for n-butanol and soybean biodiesel [36].

states, which indicates the start of exothermic chemical reaction and heat release. Generally speaking, natural flame emission from conventional diesel combustion includes two parts: chemiluminescence and soot luminosity. For diesel combustion, chemiluminescence often comes from the visible and near ultraviolet bands due to OH, CH, CH<sub>2</sub>O, and C<sub>2</sub> radicals [48]. However, the chemiluminescence signal is quite weak in diesel combustion and the ICCD camera is needed to capture these nonluminous flames. It should be noted that chemiluminescence exists on the whole diesel combustion process, but it is overwhelmed by strong radiation from luminous flame after soot is generated in the flame. The soot luminosity in the GDI engine is also very strong and thus the chemiluminescence from interesting species produced in combustion processes will be disturbed. The similar problem can also be found in the spectral analysis. The spectral analysis has been used as an in-cylinder diagnostics for many years [49]. However, due to the strong black body radiation from soot particles, the signal to noise ratio is usually too low for detecting the specific species if the flame includes a large amount of soot particles.

Most researches involved with spectral analysis were applied to the conventional gasoline engines or diesel engines with low sooting fuels such as dimethyl ether (DME). But for the new combustion models, such as HCCI, PCCI, and LTC, they only emit very low soot emissions. Therefore, the chemiluminescence images and spectral analysis are more suitable to these new combustion modes. In this part, the chemiluminescence imaging and spectral analysis will be introduced in these new combustion modes. And the soot luminosity optical diagnostics will be introduced in the next section.

**3.1.1. Chemiluminescence Analysis for HCCI.** Hultqvist et al. [50] investigated the HCCI combustion process using chemiluminescence images and spectra fueling the blends of n-heptane and isooctane. Cool flames were found at about  $-20^{\circ}\text{CA}$  ATDC with a weak and homogeneous distribution in the visible area, which was called as low temperature heat release (LTHR). After cool flames, no luminosity could be captured until the main heat release started. During high temperature heat release (HTHR), the fuel/air mixture begins

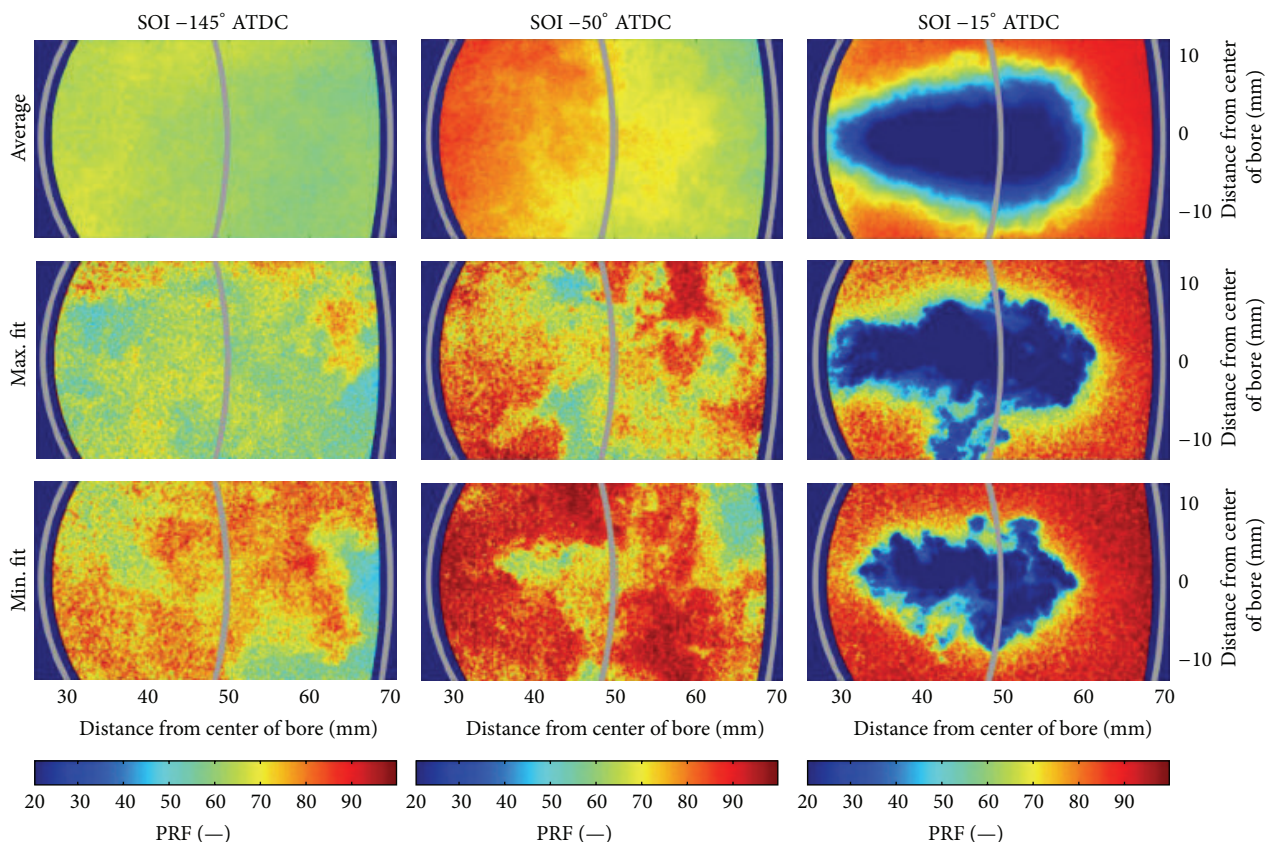


FIGURE 5: Comparison of ensemble-averaged and single shot PRF images at  $-5^{\circ}$  ATDC [37].

to autoignition simultaneously at arbitrary points throughout the visible area. The peak light intensity at HTHR is one order of magnitude greater than that of LTHR. Kim et al. [51] investigated HCCI combustion with dimethyl ether in a single cylinder engine using spectra analysis. Results showed that the cool flames in LTHR was derived from HCHO according to Emel ous's bands while the CO-O recombination spectra was the main emission during HTHR and a strong correlation was obtained between high temperature heat release and the CO-O recombination spectra.

Augusta et al. [52] investigate the effects of different engine operating parameters on the chemiluminescence spectra in a HCCI engine and the changes of operating parameters including the intake temperatures, fuel supply methods, and engine loads. Results found that the changes of engine operating parameters led to different autoignition timings but these operating parameters did not affect the reaction pathways of HCCI combustion once the combustion started. Several distinct spectra peaks emitted by CHO, HCHO, CH, and OH could be observed and all these spectra were superimposed on the CO-O continuum. The similar results have also been obtained in the study works of Liu et al. [53] and Murase et al. [54].

Mancaruso and Vaglieco [55] investigated the autoignition and combustion processes of HCCI in a diesel engine with high-pressure common-rail injection system. By using common-rail injection system, the total fuel mass per cycle

was split into five injections. The chemiluminescence images and spectra showed that the HCO and OH were homogeneously distributed in the visible area. Since a large amount of OH radicals were captured in the visible area, it suggested that OH radicals should be contributed to the soot reduction in the cylinder. The OH radicle was a suitable tool to identify the start of HTHR and phase the rate of heat release.

All in all, the HCCI combustion process can be described as following. At LTHR, a homogeneous weak light can be observed throughout the chamber, which is caused by the HCHO chemiluminescence. At HTHR, more strong luminosity derived mainly from CO-O continuum and OH is a mark of the start of high temperature reaction. Between LTHR and HTHR, no luminosity can be captured.

*3.1.2. Chemiluminescence/Natural-Luminosity Analysis of Stratified HCCI.* Dec et al. [56, 57] investigated the HCCI chemiluminescence imaging on a single-cylinder optical engine by a high-speed intensified camera. Isooctane, as a surrogate of gasoline, was used as the test fuel and the start of injection was set to  $-320^{\circ}$ CA ATDC. High-speed chemiluminescence images show that the HCCI combustion has a progressive process from the hot region to cold region even as the fuel and air are fully premixed before intake occurs, as shown in Figure 6. This result demonstrated that the HCCI combustion was not homogeneous and they thought that the inhomogeneities should be derived

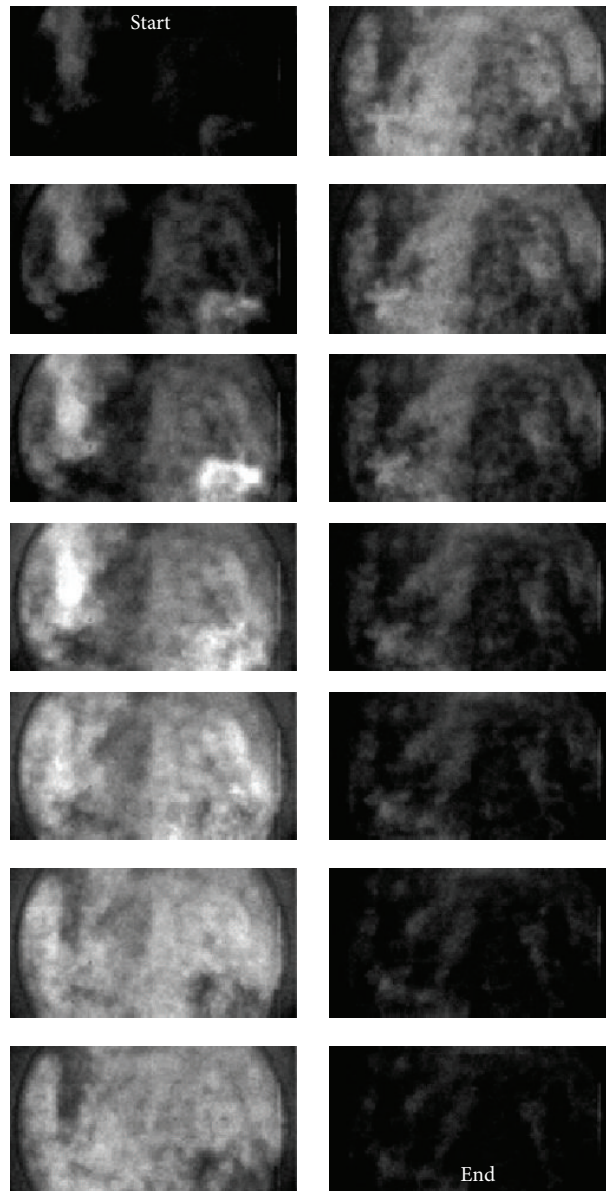


FIGURE 6: High-speed movie sequence of HCCI (the interval between frames as displayed is  $100 \mu\text{s}$  ( $0.71 \text{ CAD}$ ), and exposure time is  $49 \mu\text{s}$  per frame) [56].

primarily from naturally thermal stratification caused by heat transfer during compression and turbulent transport in the cylinder. And these inhomogeneities could slow the pressure rise rate (PRR) and thus had more advantages on the high-load extending. It should be noted that this propagation is derived from autoignition but does not take place through flame propagation because the global propagation speed is much higher than some very fast turbulent hydrocarbon flames [58, 59]. Furthermore, the similar HCCI combustion processes have also been found by Hultqvist et al. [60]. Therefore, the HCCI combustion process also includes the temperature or thermal stratification caused by the heat transfer in the cylinder. If we can strengthen the charge or thermal stratification through some active methods, such as different injection strategies, internal or external EGR, the

geometry of combustion chamber, and the modulated intake temperatures, the HCCI operating range will be extended further and the combustion phasing should be controlled.

Vressner et al. [61] investigated the effects of turbulence on HCCI combustion and the turbulence was formed by two different combustion chamber geometries: one disc shaped and the other a square bowl in piston. The chemiluminescence images demonstrated that the combustion began in the square bowl and propagated to the squish volume. The combustion process was more stratified in the square bowl geometry because of temperature inhomogeneities. The piston with a square bowl can form stronger turbulence than that of disc shaped piston, and then the variation of turbulence intensity will form the temperature stratification in the cylinder. Therefore, 2-stage combustion including in

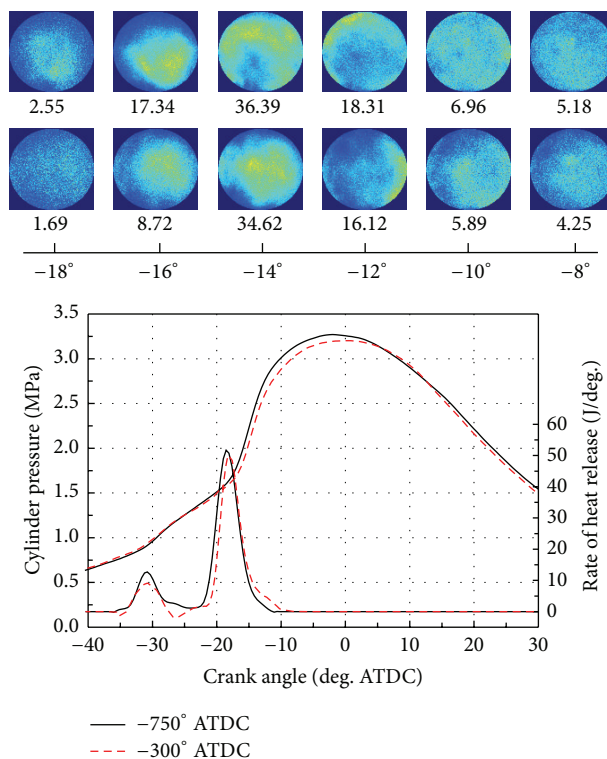


FIGURE 7: Chemiluminescence images under different intake and coolant temperatures with the same 50% burn point and  $\text{SOI} = -300^\circ\text{CA}$  ATDC;  $T_{\text{in}} = 95^\circ\text{C}$ ,  $T_c = 85^\circ\text{C}$  (first) and  $T_{\text{in}} = 125^\circ\text{C}$ ,  $T_c = 55^\circ\text{C}$  (last). The number below each image is the light intensity [62].

and out the square bowl was observed and led to a lower PRR compared to the disc shaped combustion chamber where the turbulence and temperature were more homogeneous and thus the autoignition occurred simultaneously in the chamber.

Liu et al. [62, 63] formed different charge and temperature stratification on the HCCI combustion by modulating injection timings, intake and coolant temperatures, and combustion chamber geometries. Figure 7 showed the chemiluminescence images with different temperature stratifications. The higher intake temperature of  $125^\circ\text{C}$  and lower coolant temperature of  $55^\circ\text{C}$  formed larger temperature stratification in the visible area and thus the combustion presented more inhomogeneous than that of intake temperature of  $95^\circ\text{C}$  and coolant temperature of  $85^\circ\text{C}$  where the in-cylinder had lower temperature stratification. The larger temperature stratification resulted in lower heat release rate and had the potential to extend the operating range to higher loads. Figure 8 presented the HCCI combustion process with different combustion chamber geometries. Various squish lip configurations as shown in Figure 9 generated different turbulence motion in the chamber and therefore the autoignition location for V-type and H-type geometries was more dispersive and near to the chamber wall, while the autoignition of A-type geometry always started in the center of the chamber due to the fact that high turbulence intensity in the bowl resulted in larger heat loss through the chamber wall. Therefore, the A-type geometry induced higher turbulent kinetic energy and led to larger temperature inhomogeneities, which had

more advantages on reducing PRR and heat release rates. This proves that the change of piston geometry can induce different turbulence or temperature stratification, which will affect the HCCI combustion processes although it is generally thought that HCCI is controlled by chemical kinetics.

Aleiferis et al. [64] generated charge and thermal stratification under HCCI conditions by different injection timings and by both inlet air heating and residual gas trapping (internal EGR). Combustion images showed that the larger temperature inhomogeneities in the cylinder would lead to slower autoignition front moving speed. These temperature inhomogeneities were derived from the difference in injection timings without EGR conditions or from the mixing between the fresh fuel/air and the trapped residual gases in cases with IEGR.

Berntsson and Denbratt [65] investigated the effect of charge stratification on combustion and emissions under HCCI operating conditions. Port injection was used to create a homogeneous charge in the cylinder, while a GDI injector was used to form charge stratification. They compared the early autoignition process on both homogeneous and stratified conditions. From autoignition appearing to reactions taking place throughout the combustion chamber, the HCCI with homogeneous conditions would spend  $4^\circ\text{CA}$ , while the stratified condition spent  $8^\circ\text{CA}$ . Furthermore, the combustion images showed that the combustion duration was enlarged because the local variation of equivalence ratio can moderate the rate of heat release and thus can further extend HCCI operating range.

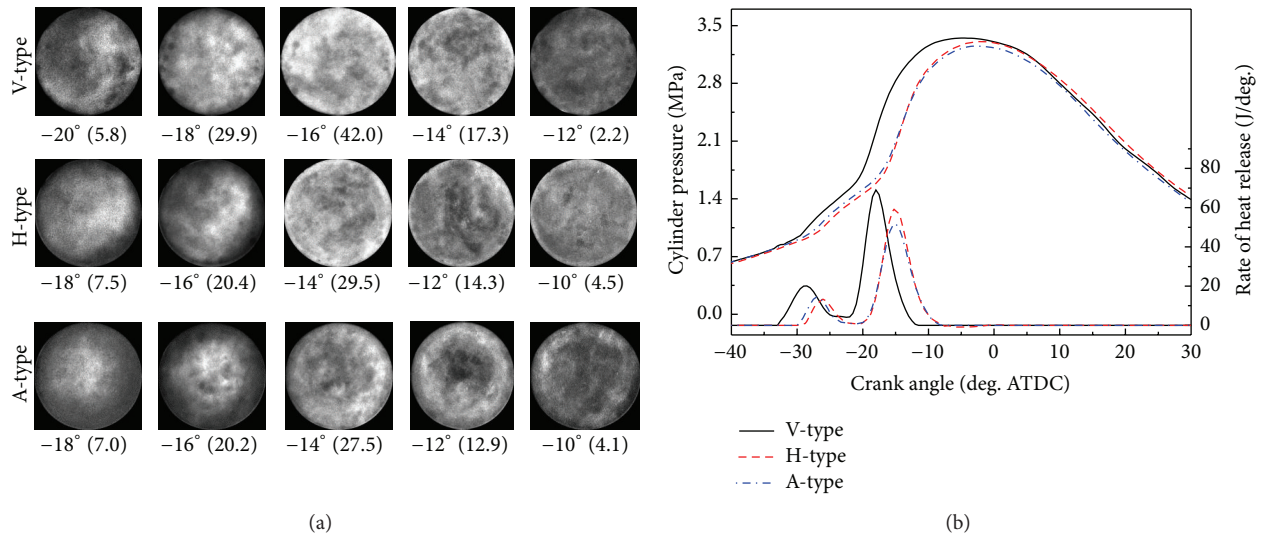


FIGURE 8: Chemiluminescence images, cylinder pressure, and rate of heat release with various piston bowl geometries at  $T_{in} = 95^{\circ}\text{C}$ ,  $T_c = 85^{\circ}\text{C}$ . The number below each image is the crank angle and light intensity [63].

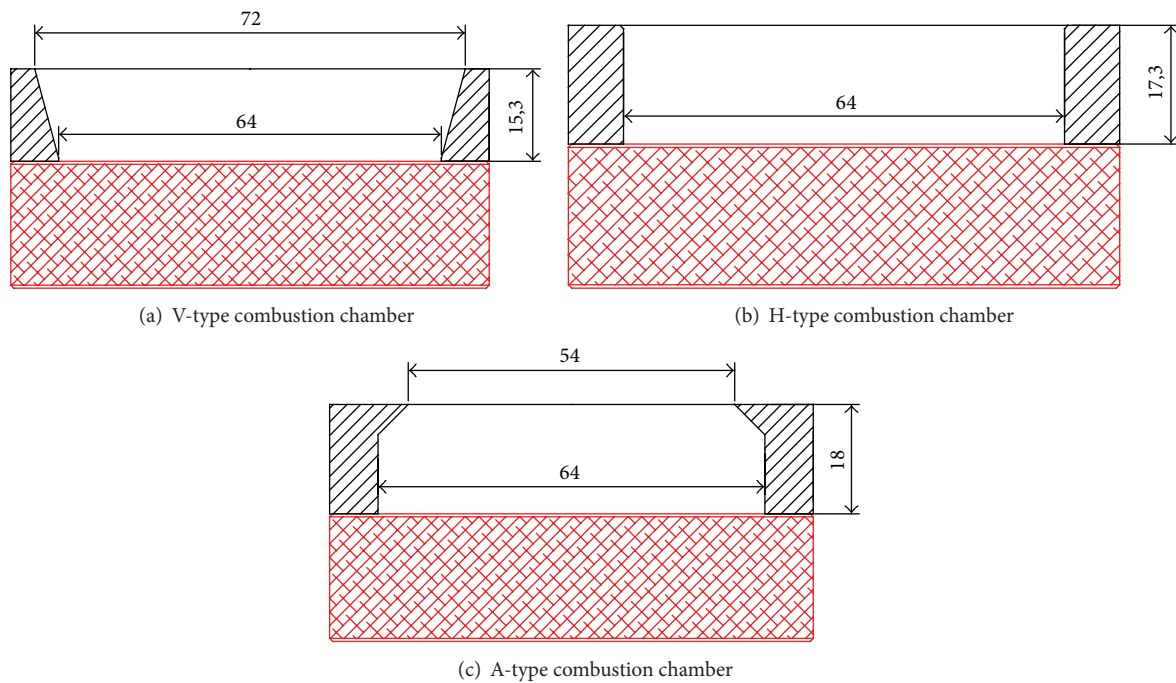


FIGURE 9: Various piston bowl geometries with the same compression ratio, squish distance, and visible area [63].

Kook and Bae [66] investigated the premixed charged compression ignition (PCCI) combustion by two-stage injection strategy in a diesel engine. The first injection ( $10\text{ mm}^3$ ) was set to  $-200^{\circ}\text{CA}$  ATDC to generate homogeneous and complete mixture between diesel and air. The second injection ( $1.5\text{ mm}^3$ ) was set to  $-15^{\circ}\text{CA}$  ATDC as an ignition promoter and to control the autoignition process. The injection pressure was controlled at 120 MPa. Meanwhile, the conventional diesel combustion was also tested in comparison with PCCI, of which total fuel ( $11.5\text{ mm}^3$ ) was injected into the cylinder at  $-15^{\circ}\text{CA}$  ATDC directly. The luminous flame could

be observed due to the thermal radiation from soot as shown in Figure 10. However, for the PCCI, the luminous flames were quite weak and the distribution was also quite limited and only located at heterogeneous combustion regions of the second injection. Finally, the authors concluded that the first injection timing needed to be advanced earlier than  $-100^{\circ}\text{CA}$  ATDC for the homogeneous and nonluminous flames (Figure 11).

Based on above reviews on charge or thermal stratification through some active methods, it can be found that the stratification can reduce maximum heat release rates and

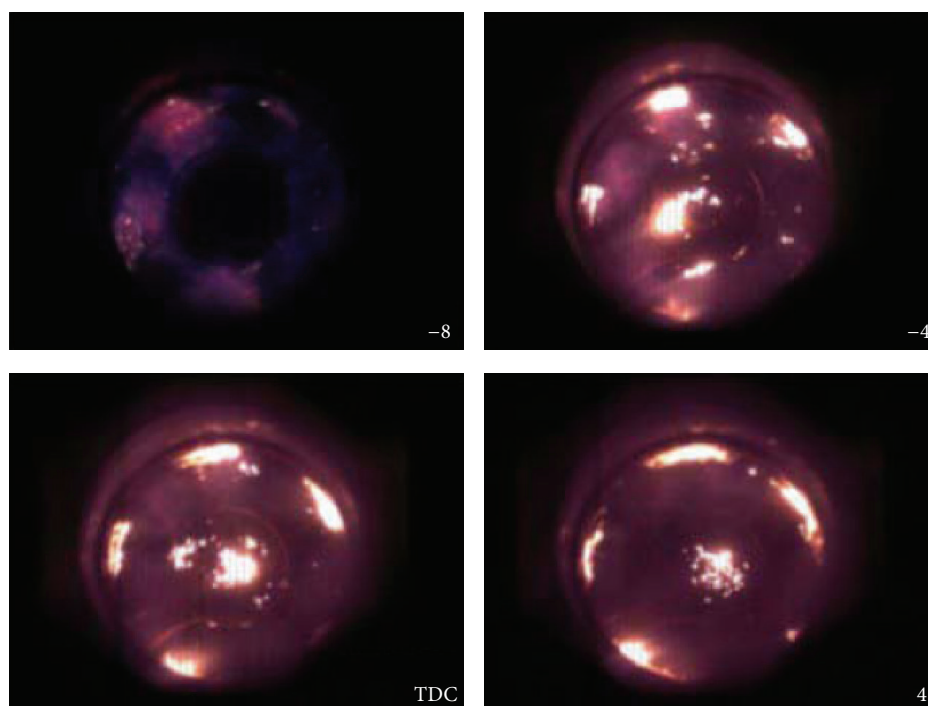


FIGURE 10: Direct-imaging of luminous DI-diesel combustion; single injection, injection timing =  $-15^{\circ}$ CA ATDC, injection quantity =  $11.5 \text{ mm}^3$ , injection pressure = 120 MPa, and injection angle =  $150^{\circ}$  [66].

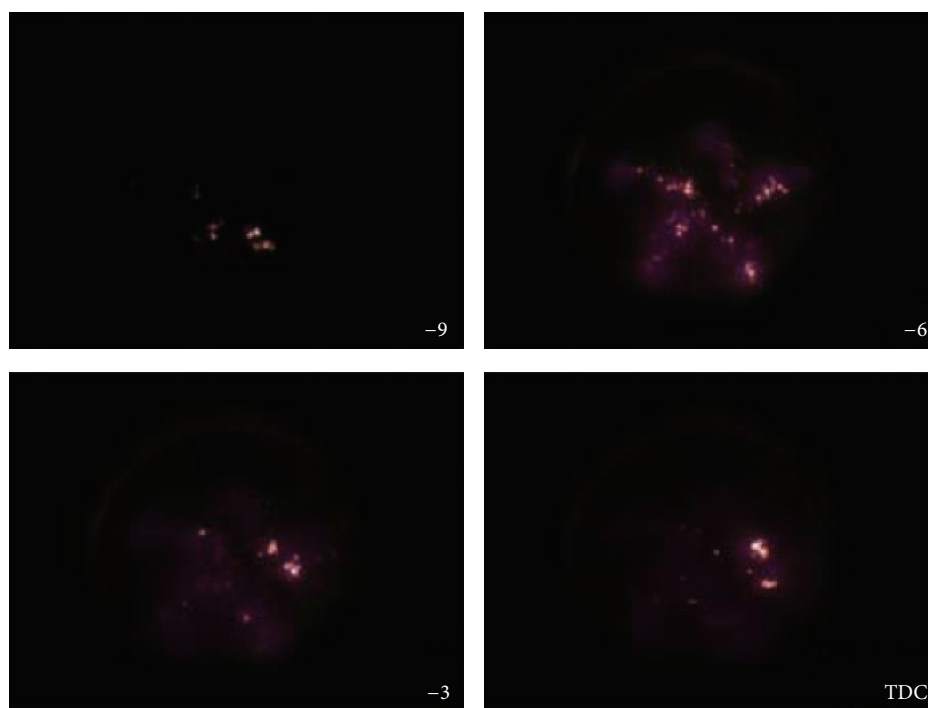


FIGURE 11: Direct imaging of PCCI combustion with two-stage injection strategy; main injection timing =  $-200^{\circ}$ CA ATDC, main injection quantity =  $10 \text{ mm}^3$ , second injection quantity =  $1.5 \text{ mm}^3$ , injection pressure = 120 MPa, and injection angle =  $150^{\circ}$  [66].

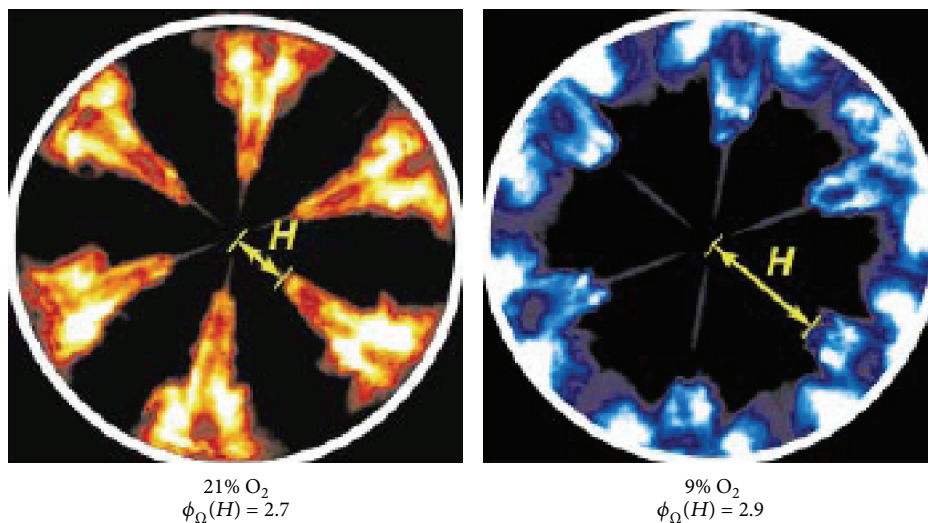


FIGURE 12: The imaging of conventional diesel and LTC [67].

pressure rise rates and thus may extend HCCI operating range. The combination between port-injection and direct injection or two-stage direct-injection in the cylinder is effective technological measures to achieve charge stratification. However, for temperature or thermal stratification, the most direct measures are changing the intake and coolant temperatures but this method is very hard to achieve in a real engine. Accordingly, the internal EGR is a more reliable method to form temperature inhomogeneity in the cylinder; however the EGR will affect the HCCI combustion by chemical action, dilution, and temperatures. Therefore, it is very hard to clarify that the temperature stratification caused by IEGR must be a very main reason on affecting HCCI combustion. In addition, a specific piston geometry will also form different turbulence intensity and thus generate the temperature inhomogeneity. Anyway, the charge and thermal stratification are effective methods to control the HCCI combustion.

**3.1.3. Chemiluminescence/Natural-Luminosity Analysis of LTC.** Since the diesel fuel has low volatility, the port-injection is not a practical way without significant change of intake system, such as increasing intake temperature. An early in-cylinder injection strategy, to some extent, can result in a quite homogeneous charge before ignition. However, due to lower charge density, in-cylinder pressure, and temperature, the liquid fuel impingement on the liner wall or piston wall is unavoidable, which leads to high HC and CO emissions and oil dilution. In recent ten years, high EGR dilution low-temperature combustion (LTC) has gained tremendous attention [67–75]. For LTC, the start of injection is near to top dead center; therefore the injection timing can control the autoignition timing to some extent. Furthermore, the later injection timing will not result in fuel impinge into piston head or cylinder liner. However, the late injection leads to the uncompleted mixing between diesel fuel and air, and thus there is a locally rich region in the mixture which is similar to diesel conventional combustion. But the soot formation can still be suppressed due to the

quite low combustion temperature caused by large amounts of EGR which can avoid the soot formation region. Akiyama et al. [20] firstly found that high EGR dilution can suppress soot formation on an optical diesel engine in 2001. The soot luminosity was increased firstly with the increase of EGR rates, but with higher EGR rates, soot luminosity was decreased and no luminosity was observed under quite high EGR dilution. Simultaneously, NO<sub>x</sub> emissions can also be near to zero due to high EGR dilution and subsequent low combustion temperature. In addition, the injection characteristic (including injection pressure, timing, and multiple injections) influences the temperature during the ignition delay period, the peak flame temperature reached, and the premixing improvement. Finally, in order to keep the power density and the combustion efficiency of the engine at high EGR rates, high boost levels are required. Therefore, the control and optimize of EGR rate, injection characteristic, and high boost are the keystone of the LTC. Compared to HCCI strategy, LTC has more benefits such as high efficiency over broad load range, simple control of ignition timing, reduced pressure-rise rates, high-load capability, and so forth, besides low emissions of NO<sub>x</sub> and soot. This is the reason why LTC is widely studied in recent years.

Upatnieks et al. [67, 71, 72] measured lame lift-off lengths using in-cylinder images of natural luminosity. Results showed that soot incandescence could not be observed even for local fuel-rich mixture, while the similar stoichiometric combustion must lead to soot incandescence without EGR dilution, as shown in Figure 12. Meanwhile, a blue flame could be seen for LTC condition, which was because of the too low flame temperature. Furthermore, the flame lift-off at LTC condition was larger than that of conventional diesel combustion. After that, Musculus et al. also investigated the LTC by different laser diagnostics and proposed the LTC combustion concept in the review paper [4].

Liu et al. [68, 73, 74] investigated the natural luminosity under both conventional diesel combustion and low temperature combustion by using different fuels such as

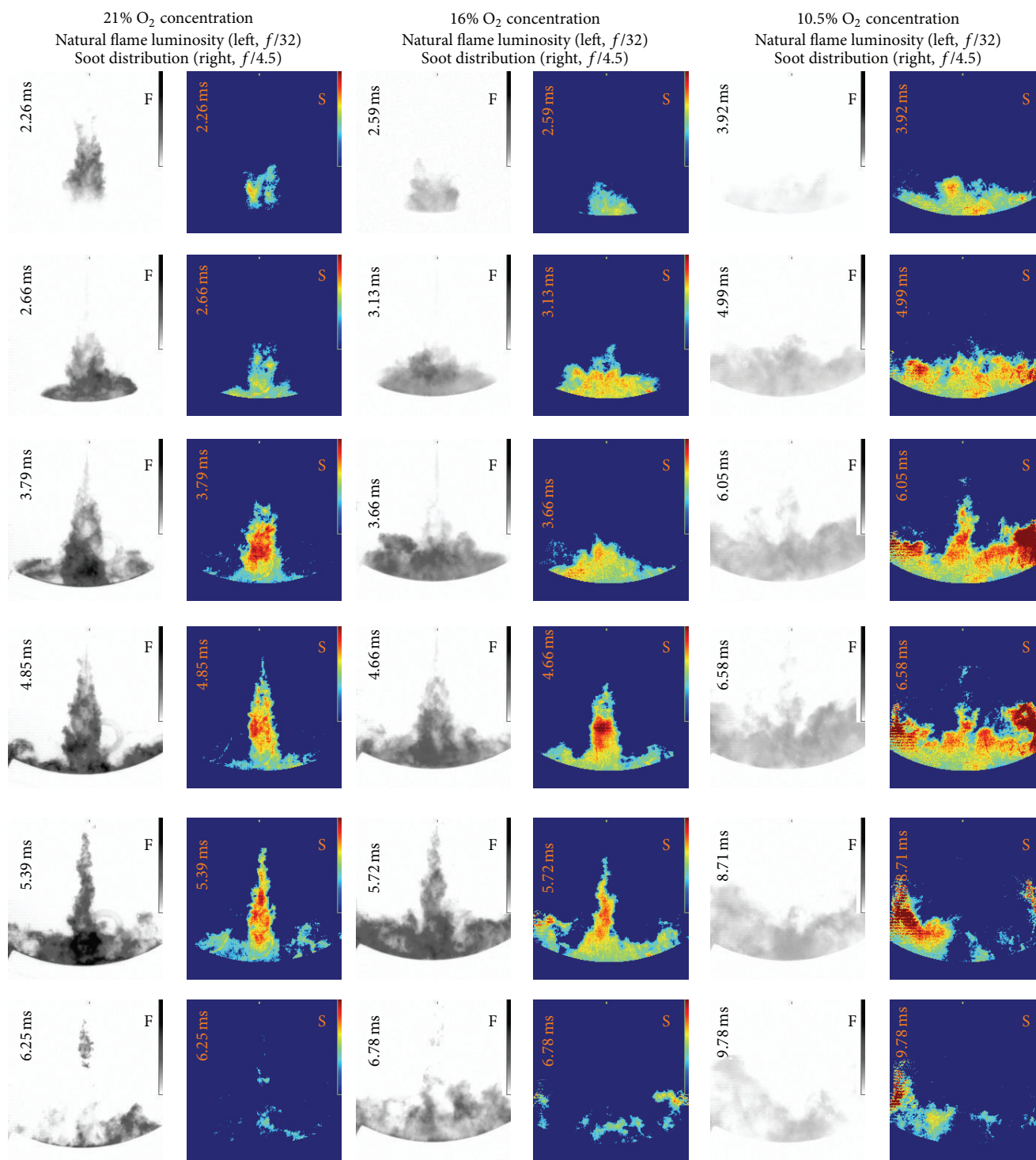


FIGURE 13: Natural flame luminosity and soot distribution for soybean biodiesel at 1000 K ambient temperature [68].

diesel, soybean biodiesel, n-butanol, ethanol, and the blended fuels. They found that natural flame luminosities were reduced with the decrease of ambient oxygen concentrations and ambient temperatures. Furthermore, the flame distribution or flame area was increased obviously at low oxygen concentration of 10.5% and much flame could be seen near chamber wall regions. However, the difference

between high and low ambient temperatures is that even if the natural luminosity was decreased with the decline of oxygen concentrations at 1000 K ambient temperature, soot emissions were increased as shown in Figure 13. But, the natural luminosities and soot emissions were reduced simultaneously at 800 K ambient temperature as shown in Figure 14. Further analysis conducted by Bi et al. [75] found

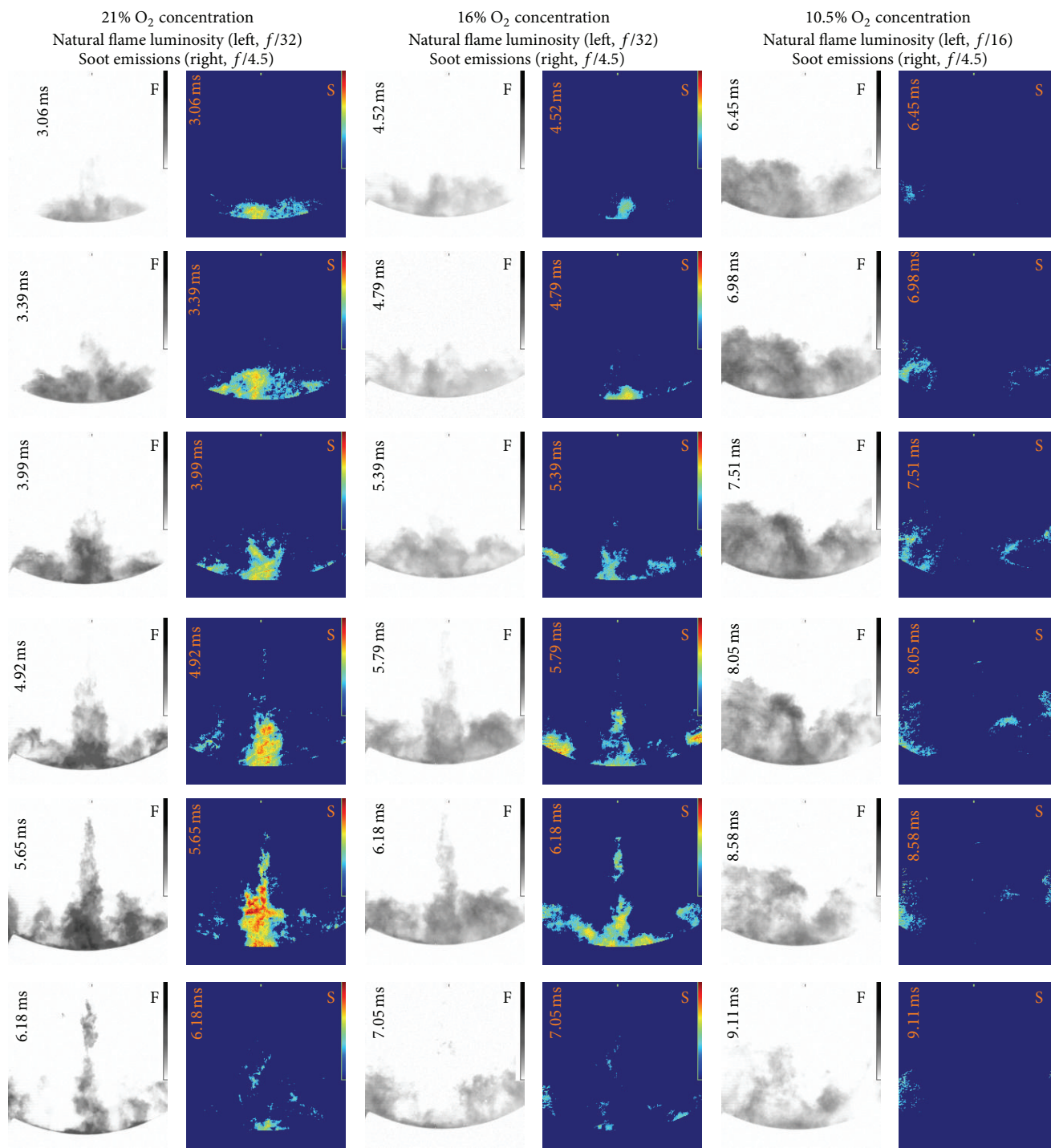


FIGURE 14: Natural flame luminosity and soot distribution for soybean biodiesel at 800 K ambient temperature [68].

that the changes of oxygen concentrations altered the soot formation and oxidation rates and thus resulted in different soot emissions.

Based on above reviews on natural luminosity of LTC, it can be found that the combustion flame with larger distribution was more near to cylinder wall, which means that the flame lift-off are larger than that of conventional diesel

combustion. With the decrease of oxygen concentrations or with the increase of EGR rates, the natural luminosity reduced monotonously, but the soot emissions increase firstly and then decrease after achieving the peak value.

3.2. Laser Diagnostic Imaging on Chemical Reaction Processes of HCCI and LTC. Above reviews are aiming for the methods

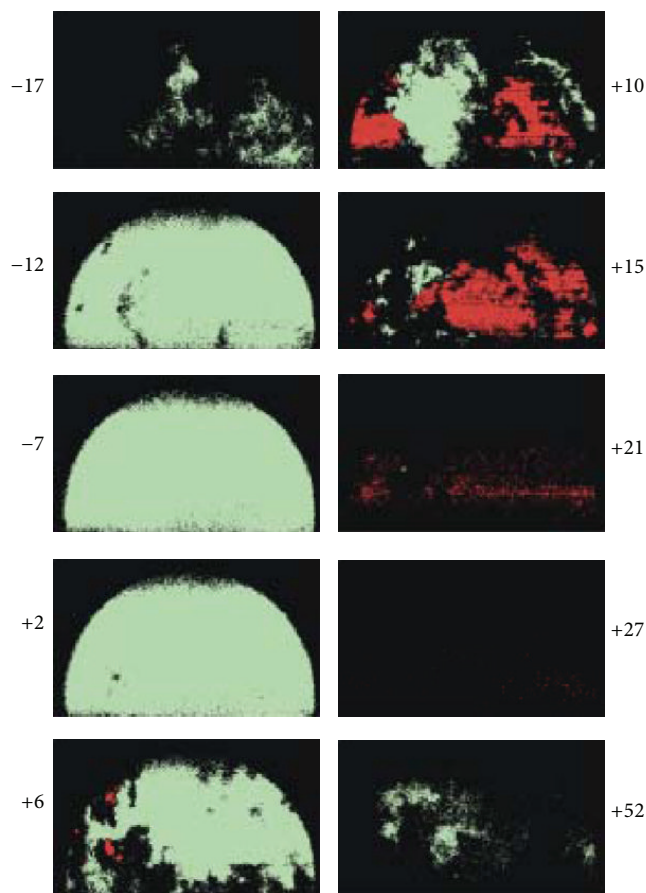


FIGURE 15: Single-shot images from onset of LTR combustion until the end of the main combustion. Formaldehyde is shown in green and OH is shown in red [76].

of chemiluminescence or natural luminosity. Even if the direct images are easy to measure, some combustion intermediate species cannot be measured effectively. By the laser diagnostics, the specific species can be captured by adjusting the laser wavelength. Therefore, the laser diagnostics on HCCI and LTC combustion species will be reviewed in this section.

Collin et al. [76] simultaneously measured OH and formaldehyde LIF on an HCCI engine using two laser sources at wavelength of 283 and 355 nm and two ICCD cameras were used to collect LIF signals. The blend of isooctane and n-heptane was used as tested fuel and was injected by intake port and the compression ratio of the HCCI engine was set to 12. The width of the laser sheet was 40 mm, which is nearly a half of the cylinder bore. Results showed that formaldehyde could be captured at the start of the low temperature reactions as shown in Figures 15 and 16. With the progress of the combustion reaction, more formaldehyde was detected in the cylinder and formaldehyde filled the entire visible area after the low temperature reactions ended. At the start of the high temperature reactions, some holes in homogeneous formaldehyde signals could be captured, which demonstrated that formaldehyde was consumed with the progress of combustion processes. At about 6°CA ATDC,

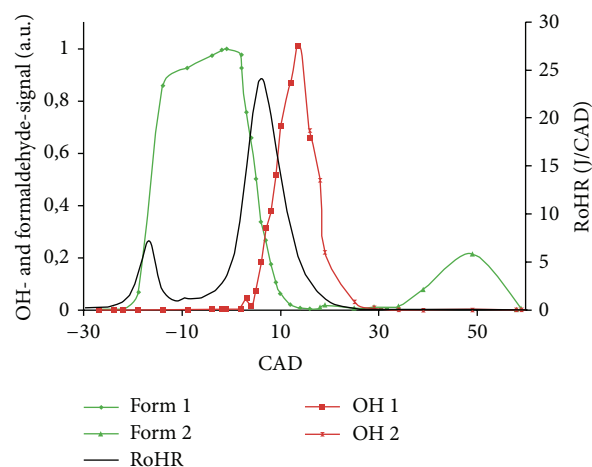


FIGURE 16: Average rate of heat-release and average OH- and HCHO-signals [76].

OH-LIF was captured firstly, and the OH-LIF could only be observed in regions where formaldehyde was absent. Under a relatively long period about 9-crank-angle degree, LIF signals of OH and formaldehyde were captured simultaneously but never in same regions for these two intermediate species. The OH-LIF intensity was lagging the rate of heat release (RoHR) by about 8 crank-angle degree, and the maximum OH intensity was captured as the most of fuel was consumed at about 15°CA ATDC and thus close to in-cylinder peak temperature. Therefore, the autoignition and combustion processes of HCCI can be detected by visualizing the distributions of formaldehyde and OH radicals. For formaldehyde, its formation occurs through low temperature oxidation in an early phase of the ignition process and then is consumed later in the combustion process. Therefore, formaldehyde is an indicator of the autoignition of low temperature heat release in HCCI engine. Meanwhile, it is also a marker for regions with low temperature reactions. For OH radical, it is formed in flame regions with high temperature and there is a strong relationship between maximum combustion temperatures and maximum OH concentrations.

Särner et al. [77] simultaneously investigated images of formaldehyde-LIF and fuel-tracer LIF in a direct-injection HCCI engine. The blend of n-heptane and isooctane was used as fuel and toluene was added as fluorescent tracer. LIF of fuel-tracer was excited by a Nd:YAG laser with the wavelength of 266 nm, and the fluorescence was captured by an ICCD camera in the spectral region of 270–320 nm. Formaldehyde-LIF was excited by the other Nd:YAG laser with the wavelength of 355 nm, and the fluorescence was captured by the other ICCD camera in the spectral region of 395–500 nm. An early injection timing (−250°CA ATDC) was used to form homogeneous charge and the distribution of fuel-tracer and formaldehyde-LIF were quite homogeneous before it was consumed at start of high temperature reaction as shown in Figure 17. However, for a late timing (−35°CA ATDC), it formed stratified charge and the distribution of fuel-tracer and formaldehyde-LIF were inhomogeneous

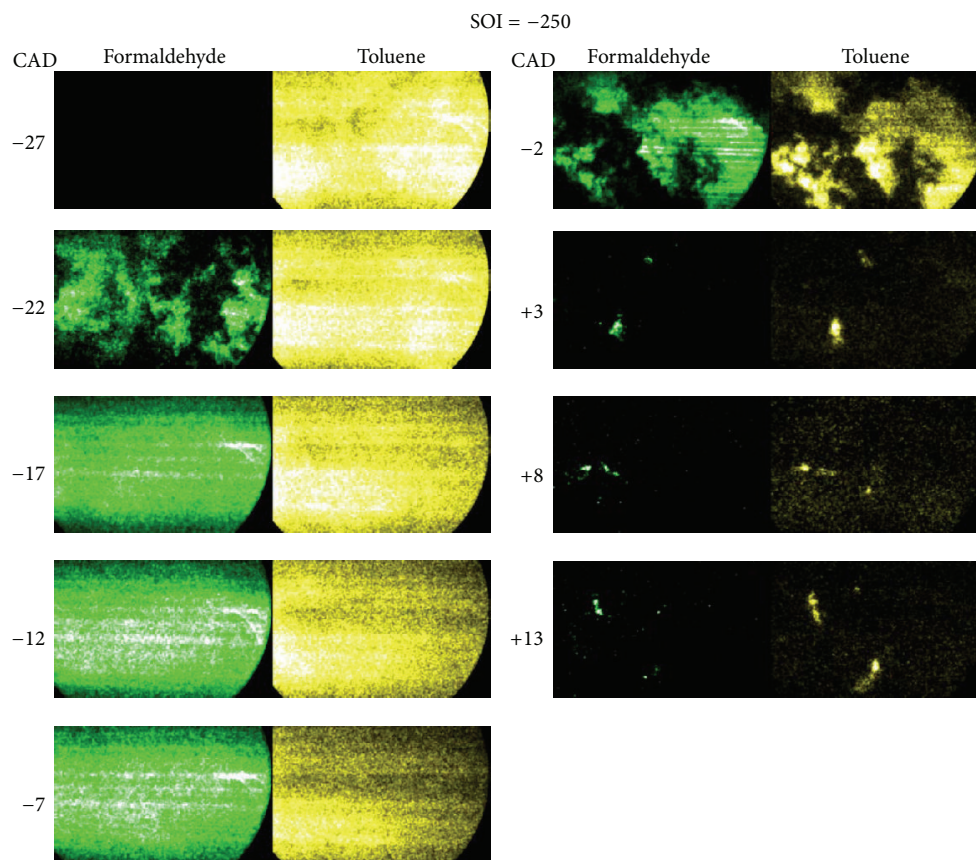


FIGURE 17: Simultaneous images of formaldehyde and toluene at start of injection of  $-250^{\circ}\text{CA}$  ATDC to ensure the fuel sufficient time to mix with air forming a very homogeneous mixture before ignition [77].

in the visible area as shown in Figure 18. Images from both early and late injection showed that both toluene and formaldehyde LIF signals have very similar distribution. That is to say, once fuels have higher boiling points and thus no suitable tracer can be used to measure, the formaldehyde-LIF is a good alternative method to fuel-tracer LIF.

Zhao et al. [78] investigated formaldehyde-LIF distribution on the HCCI combustion process by fueling different primary reference fuels (PRFs). They found that the formaldehyde formation was mainly affected by the charge temperature, while the fuel concentration had less effect on formaldehyde formation. Even if PRFs had different isooctane ratio, all fuels had similar formaldehyde formation timings to that of pure n-heptane, which meant that the addition of isooctane did not influence the start of low temperature reactions apparently.

Kashdan et al. [29] investigated the late-injection diesel fuel HCCI combustion process at 45% EGR dilution. They found that formaldehyde-LIF images could be captured earlier than that of chemiluminescence in early stages of the cool flame. Similar to the homogeneous conditions, formaldehyde was consumed quickly at the start of the high temperature reactions and took place by the presence of OH-LIF subsequently. Because of the late injection resulted in some local high equivalence ratio regions, soot precursors were also captured, demonstrated by the strong PAH fluorescence.

In his further study [79], they investigated the effects of split injection and EGR rates on HCCI combustion. They found that the start of formaldehyde-LIF signals was not affected by EGR rates, but the high temperature heat release was advanced with the decrease of EGR rates and ultimately reduced the formaldehyde lifetime and consequently increased the inhomogeneous state in the cylinder. As split injection was used, formaldehyde-LIF showed locally rich distribution like the reference of 73, which demonstrated that the split injection resulted in larger charge stratification. Furthermore, the lifetime of formaldehyde-LIF was prolonged and the whole combustion duration was also prolonged.

Hildingsson et al. [80] investigated formaldehyde- and OH-LIF on a light duty diesel engine with different injection strategies of port-injection HCCI, direct-injection HCCI, and UNIBUS. The formaldehyde formation always began at about  $20\text{--}25^{\circ}\text{CA}$  BTDC no matter what injection strategies were used. But the intensity of formaldehyde-LIF was very fast for port-injection HCCI compared to UNIBUS and late-injection HCCI. This should be due to the fact that port-injection can supply more homogeneous charge than that of direct-injection HCCI and UNIBUS, and thus the whole chemical reaction rates are higher. Formaldehyde-LIF lifetime in the UNIBUS injection strategy was longer than that of port- or direct-HCCI because formaldehyde was formed from the dual injections of the fuel.

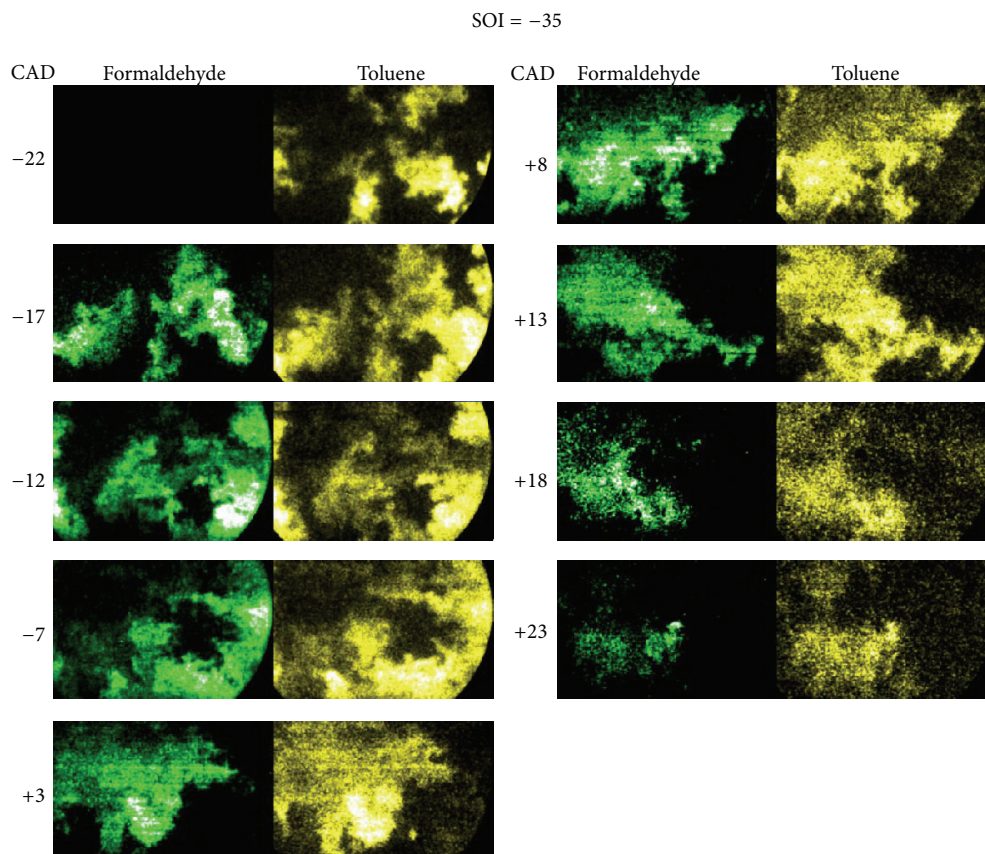


FIGURE 18: Simultaneous images of formaldehyde and toluene at start of injection of  $-35^{\circ}$  CA ATDC to form a stratified mixture before ignition [77].

Berntsson et al. [81, 82] investigated the effects of spark-assisted stratified charge HCCI combustion processes. LIF diagnostics on fuel-tracer, formaldehyde, and OH were conducted on an optical single-cylinder direct-injection SI engine with negative valve overlap (NVO) and low lift to increase the thermal atmosphere to ensure the stable HCCI combustion. They found that the charge inhomogeneity was formed in the cylinder and the fuel injection timing and spark-assisted ignition timings were the primary parameters to affect the HCCI combustion phasing. The high-temperature reactions were influenced by injection timings and spark-assisted ignition timings, indicating different amounts of OH-LIF signals. Based on NVO, spark-assisted ignition, and charge stratification, HCCI combustion phasing could be effectively controlled and the operating range could be extended to lower and higher engine loads.

Musculus [19] investigated the OH-LIF and chemiluminescence of low temperature combustion at the injection timing of  $-22^{\circ}$  CA ATDC. He found that a distinct cool flame could be captured and overlapped with the liquid fuel spray, which would increase the rate of fuel vaporization. Compared to conventional diesel combustion, the OH-LIF distributions were different. For conventional diesel combustion, OH radicals could only be captured at the periphery of the diesel jet with a thin sheet structure. However, for LTC conditions, OH radicals could be detected throughout the jet cross

section, which demonstrated that there was more complete mixing between liquid jet and ambient air. Furthermore, once autoignition occurred, OH radicle could be detected with broadening distributions, which demonstrated that the LTC process should be the volumetric autoignition and combustion, rather than flame propagation in conventional diesel combustion.

Above studies show that the formaldehyde and OH are good markers of the HCCI combustion process at low temperature and high temperature reactions, respectively. Furthermore, the distribution of OH and formaldehyde is never in the same regions even if both of them can be detected simultaneously at a relatively long period. The timing of formaldehyde formation is unaffected by the EGR level, but the formaldehyde lifetime and the degree of homogeneity and subsequent high temperature ignition are influenced by EGR level. For a given EGR rate, a split injection strategy results in the charge stratification and prolongs the HCHO lifetime. Furthermore, the rising rate of formaldehyde-LIF intensity is more quickly under homogeneous conditions than that of stratified conditions. OH distributions in HCCI and LTC combustion processes are more broad than that of conventional gasoline spark-ignition or diesel compression-ignition, which indicates that the whole combustion should be more close to volumetric combustion rather than flame propagation. Therefore, the LIF diagnostics are a quite

effective method to reveal the HCCI and LTC combustion process with high spatial distributions.

#### 4. Optical Diagnostics for Emissions Evolution

Due to the very low emissions of  $\text{NO}_x$  and soot for HCCI combustion with port-injection or early-injection due to the quite homogeneous charge, the researches on emissions are very limited. But if the fuel stratification is introduced by late direct-injection, the emissions of  $\text{NO}_x$  and soot will increase. So, the study on  $\text{NO}_x$  and soot formation process is necessary to reduce them in new combustion modes. In this section, optical researches on these emissions mainly focus on the NO and soot.

**4.1.  $\text{NO}_x$  Optical Diagnostics on HCCI and LTC.** The spectroscopic structure of the NO molecule permits a number of excitation detection strategies and some of them have been utilized in engines. However, all of these strategies are more or less susceptible to the interference from oxygen [83], PAH, and  $\text{CO}_2$  [84]. Also, all techniques in varying degrees are the absorption of laser and signal light mainly by hot  $\text{CO}_2$  and  $\text{H}_2\text{O}$  [85]. Furthermore, the signal is dependent on pressure, temperature, and burned gas composition. Advantages and disadvantages of different excitation/detection strategies have been discussed extensively in a series of publications [86–88].

NO-LIF images have been developed and applied over the last decade in conventional CI or SI engines and GDI engines by many researchers [88–91]. These researches developed the theory of the NO formation. For example, Dec and Canaan [88] investigated the NO-LIF in a conventional diesel engine and found that NO was not produced by the initial premixed combustion which was fuel-rich but began around the jet periphery just after the diffusion flame formed. Then, NO formation increased progressively and NO was still confined to the jet periphery until the jet structure started to disappear toward the end of heat releases. After that, the LIF signals could also be captured until the end of heat releases, which demonstrated that NO formation continued in hot postcombustion gases. However, in new clean combustion modes, NO emissions are very low due to the quite low combustion temperature, which restricts NO formation. Therefore, there is little research on the NO-LIF in an HCCI combustion processes.

Zilwa and Steeper [92, 93] predicted the emissions of  $\text{CO}_2$ , CO, HC, and  $\text{NO}_x$  from HCCI engines using LIF fuel-distribution measurements. The method is based on the simplifying premise that each individual fuel-air packet burnt as if in a homogeneous mixture at the same equivalence ratio. The relative success of the prediction method indicated a strong correlation between in-cylinder charge distribution and engine emissions. In particular it encouraged the formulation of ideal fuel distributions to guide the development of advanced charge-preparation strategies in HCCI and LTC modes.

**4.2. Soot Optical Diagnostics on HCCI and LTC.** Due to the sufficient premixed combustion, the soot emission in HCCI

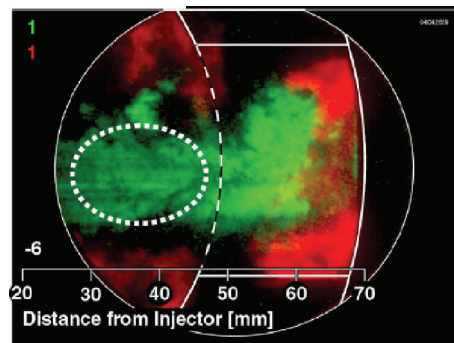


FIGURE 19: OH (green, OH-PLIF) throughout jet cross section, with soot (red, soot luminosity) only at head of jet [19].

can be negligible. But, once the charge stratification was introduced in HCCI, the soot emission will not be neglected in some operation conditions. In this section, the focus will be the soot formation in the new combustion mode, especially for the PCCI and LTC.

Singh et al. [94] and Huestis et al. [95] investigated the soot formation and oxidation processes by two-color pyrometry in LTC conditions. Nitrogen gas was used to achieve lower oxygen concentration and different injection strategies including early-injection, late-injection, and double-injection were tested. They all found that the soot thermometry and luminosity images of LTC were lower than that of conventional high temperature combustion. Soot temperatures measured by two-color pyrometry were near to the adiabatic flame temperatures under LTC conditions. The amount of peak soot volume of late- and double-injection was about 1.5 times higher than that of early-injection. For LTC conditions, there was enough time available for diesel fuel to penetrate and mix with the ambient air, and thus sooting combustion occurred mainly near the edge of the bowl. However, soot was formed farther upstream in the fuel jet under high temperature combustion conditions.

Musculus [19] investigated the soot luminosity and soot laser-induced incandescence of low temperature combustion at the injection timing of  $-22^\circ\text{CA}$  ATDC. He found that the soot formation was only captured in regions without OH radicals, and thus soot and OH should not lie in the same regions. The soot-LII and OH-LIF in conventional diesel combustion have shown that OH radicals could only be captured at the periphery of the diesel jet or the soot cloud with a thin sheet structure at the earlier combustion stage [96, 97], as shown in Figure 19. After that, with the progress of combustion, the OH-LIF could be captured with broad distribution, but regions between soot and OH did not overlap spatially [98]. That is to say, OH and soot generally did not persist within the same regions. Both soot luminosity and soot-LII images all showed that the soot is first observed far downstream of the spray jet but located at the head of the spray jet near the cylinder liner. As the spray jet continued to penetrate and develop in the cylinder, the soot-LII were mainly located at either “side” of the jet, which was called “head vortex” for spray jet, as shown in Figure 19.

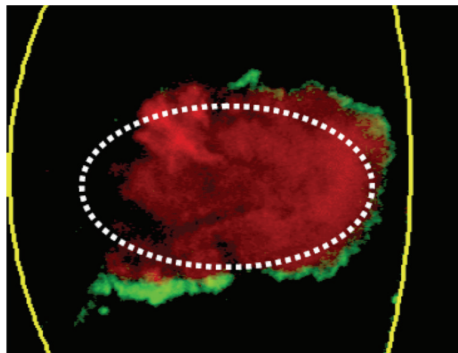


FIGURE 20: OH (green, OH-PLIF) in thin envelope surrounding soot (red, soot LII) throughout the jet cross section [27].

Indeed, even if soot-LII could be captured upstream spray, which should be attributed to the impingement of sooting jets, rather than formed by upstream spray jets. Therefore, the soot formation regions and distributions are different between LTC and conventional diesel combustion where soot is formed farther upstream and throughout the jet cross section [27, 99], as shown in Figure 20. Furthermore, soot was still formed in regions of head vortex for conventional diesel combustion. Thus, it can be concluded that the upstream soot formation has been eliminated for new LTC modes compared with conventional diesel combustion conditions. The same upstream regions have been shown as the white dotted circle in Figures 19 and 20. And, the soot formation reduction in the regions of head vortex is still a large challenge even if aiming to a relative longer premixed low temperature combustion process.

Liu et al. [68, 73, 74] quantitatively investigated the soot concentration by forward illumination light extinction with a copper vapor laser under both conventional diesel combustion and LTC conditions. Meanwhile, the soot models have been improved to understand the soot evolution [75, 100]. They found that compared with 21% oxygen concentration, both rates of soot formation and oxidation were increased simultaneously at 18% oxygen; however the higher soot formation rate resulted in the higher soot mass in the combustion process. At 15% oxygen concentration, both rates of soot formation and oxidation were reduced simultaneously; however the soot mass in the combustion process were increased further and the reason should be caused by suppressed soot oxidation rates. With the further decrease of oxygen concentrations, the soot formation was suppressed dramatically and thus the soot emissions were reduced. At 1000 K, the soot mass was increased with the decline of oxygen concentrations, which should be derived from the increased regions of high equivalence ratios and the increased acetylene and soot precursors formation at lower ambient oxygen concentration. At 800 K ambient temperature, however, the soot mass was decreased with the decline of oxygen concentrations, which should be caused by reduced regions of high equivalence ratios and by reduced acetylene and soot precursors formation. The soot distributions have been shown in Figures 13 and 14. Therefore, the authors

concluded that soot formation transition from 1000 K to 800 K should be the responsible factor for different soot emissions, because of ambient oxygen dilution in conventional and low-temperature flames. The similar studies about ambient temperatures and oxygen concentrations have also been conducted by Zhang et al. [101, 102] by two-color pyrometry and soot luminosity.

These optical diagnostics have presented the distribution and mass concentration for soot emissions in LTC modes. Unlike the conventional diesel combustion which forms soot just downstream of the liquid spray and throughout the jet cross section, the soot formation in LTC is much farther downstream of the liquid spray and only at the head of the jet, in the head vortex or near the edge of the bowl. Furthermore, even if the combustion temperature are not low as shown in Figure 13, the soot distributions are still concentrated on farther downstream of liquid spray and near the chamber wall regions. Therefore, it can be concluded that soot specific distributions are caused by quite low oxygen concentrations.

*4.3. Unburned Hydrocarbons and CO Optical Diagnostics on HCCI and LTC.* Although HCCI and LTC can achieve very low emissions of  $\text{NO}_x$  and soot, they typically have increased emissions unburned hydrocarbons (UHC) and CO. Musculus et al. [4] investigated the overmixing and unburned hydrocarbon emissions in LTC conditions on a heavy-duty optical diesel engine. The equivalence ratio of mixtures near the injector was measured under without combustion conditions by planar laser-Rayleigh scattering in a constant volume combustion chamber and by LIF of a fuel tracer in an optical engine. The optical diagnostic images indicated that the transient ramp-down of the injector produced a low-momentum spray penetration at the end of injection and thus formed fuel-lean mixture in the upstream region of the spray jet. Furthermore, the fuel-lean mixture continued until the late of that cycle. Therefore, the upstream fuel-lean mixture likely became too lean to achieve complete combustion, thus contributing to UHC emissions under LTC condition.

Ekoto et al. [103, 104] and Petersen et al. [105] investigated the UHC and CO distribution on a light-duty diesel optical engine under both early- and late-injection under LTC conditions. The LIF measurements on equivalence ratios, UHC and CO, all showed that most fuel accumulated on inner bowl during high temperature heat release, but much of them transported into the squish-volume with the motion of reverse squish flows. Then, the lean mixtures combined with high heat transfer losses to the wall suppressed the fuel oxidation in squish regions. Therefore, the main distributions on UHC and CO were captured in squish regions.

It should be noted that there are also a large amount of UHC and CO emissions in HCCI combustion processes and more studies focus on the formaldehyde-LIF measurements and there is little studies on CO distributions in HCCI. This should be due to the HCCI is controlled by chemical kinetics and the UHC and CO evolution can be explained well by chemical reaction mechanism. For LTC conditions, it is not only controlled by chemical kinetics, but also controlled by mixed process between diesel fuel and air. Under LTC conditions, fuel-lean regions that formed during the period

of ignition delays are likely a significant source of UHC and CO emissions for EGR-diluted LTC diesel engines.

## 5. Summary

Optical diagnostics is an effective method to understand the chemical reaction processes in homogeneous charge compression ignition and low temperature combustion modes. Based on optical diagnostics, the true mixing, combustion, and emissions can be seen directly. In this paper, the mixing process by port-injection and direct-injection was reviewed firstly. Then, the combustion chemical reaction mechanism was reviewed based on chemiluminescence, direct-luminosity, and laser diagnostics. Finally, the evolution of pollutant emissions was reviewed including  $\text{NO}_x$ , soot, UHC, and CO. The main summaries are shown as follows.

**5.1. Fuel-Air Mixing Process.** It can be found that different port-injection strategies also change the degree of homogeneous charge in the cylinder. Even if a high degree of homogeneity can be seen in the cylinder, there is still lying in local inhomogeneous fluctuations caused by cycle-to-cycle variations. The direct-injection strategy has more advantages than that of port-injection for HCCI autoignition control and operating range extending. However, using early direct-injection strategy, it helps to form a more uniform air-fuel mixture before ignition but fuel can impinge on the piston head or the cylinder liner and results in wall-wetting and the dilution of oil, which restricts the application of early-injection to some extent. By dual-fuel injection, the stratification on charge and fuel reactivity can be achieved flexibly even if it needs one more fuel tank.

**5.2. Combustion Chemical Reaction Processes.** It can be found that the HCCI combustion process can be described as follows. At low temperature heat release, a homogeneous weak light can be observed throughout the chamber, which is caused by the formaldehyde chemiluminescence. At high temperature heat release, more strong luminosity derived mainly from CO-O continuum and OH is a mark of the start of high temperature reaction. Between LTHR and HTHR, no luminosity can be captured. Both charge and thermal stratifications can reduce maximum heat release rates and pressure rise rates and thus may extend HCCI operating range. Optical diagnostics shows that the combination between port-injection and direct injection or two-stage direct-injection in the cylinder is effective technological measures to achieve charge stratification. Changes of the intake and coolant temperatures can form temperature or thermal stratification and affect the combustion chemiluminescence, but this method is very hard to achieve in a real engine. A specific piston geometry will also form different turbulence intensity and thus generates the temperature inhomogeneity. For low temperature combustion, the combustion flame with larger distribution is located near to cylinder wall, which means that the flame lift-off is larger than that of conventional diesel combustion.

Although the chemiluminescence or natural-luminosity images present a good time-resolved combustion process in HCCI and LTC, they only provide the results of line-of-sight and without presenting the spatial distributions. Therefore, laser induced fluorescence is used to give spatial distributions on combustion processes and results show that the formaldehyde and OH are good markers of the HCCI combustion process at low temperature and high temperature reactions, respectively. Furthermore, the distribution of OH and formaldehyde is never in the same regions even if both of them can be detected simultaneously at a relatively long period. The timing of formaldehyde formation is unaffected by the EGR level, but the formaldehyde lifetime and the degree of homogeneity, and subsequent high temperature ignition are influenced by EGR level. For a given EGR rate, a split injection strategy results in the charge stratification and prolongs the HCHO lifetime. Furthermore, the rising rate of formaldehyde-LIF intensity is more quickly under homogeneous conditions than that of stratified conditions. OH distributions in HCCI and LTC combustion processes are more broad than that of conventional gasoline spark-ignition or diesel compression-ignition, which indicates that the whole combustion should be more close to volumetric combustion rather than flame propagation.

**5.3. Emission Evolution Processes.** In HCCI and LTC, NO emissions are very low due to the quite low combustion temperature, which restricts NO formation. Therefore, there is little research on the NO-LIF in an HCCI and LTC combustion processes. There are little studies on soot evolution in HCCI due to the nearly zero soot emissions. In LTC conditions, the soot formation is much farther downstream of the liquid spray and only at the head of the jet, in the head vortex or near the edge of the bowl. Furthermore, even if the combustion temperature is not low, the soot distributions are still concentrated on farther downstream of liquid spray and near the chamber wall regions. Therefore, it can be concluded that soot specific distributions in LTC conditions are caused by quite low oxygen concentrations. There are also a large amount of UHC and CO emissions in HCCI combustion processes and some studies focus on the formaldehyde-LIF measurements to represent UHC distribution in the late cycle. But there are little studies on CO distributions in HCCI, which should be due to the fact that HCCI is controlled by chemical kinetics and the UHC and CO evolution can be explained well by chemical reaction mechanism. For LTC conditions, it is not only controlled by chemical kinetics but also controlled by mixed process between diesel fuel and air. Under LTC conditions, fuel-lean regions that formed during the period of ignition delays are likely a significant source of UHC and CO emissions for EGR-diluted LTC diesel engines.

**5.4. Future Direction.** Based on previous works reviews, it can be found that there are some shortcomings in HCCI and LTC chemical reaction processes with optical diagnostics.

Firstly, more intermediate species are needed to be measured. In current studies, the main measured intermediate species include formaldehyde, OH, and CO. Meantime, the

polycyclic aromatics hydrocarbons (PAHs) and  $H_2O_2$  have been captured in the cylinder [19, 106] or has the potential to distinguish PAHs of different rings [107] even if the study works are limited. Obviously, more intermediate species are detected and more detailed combustion reaction mechanism will be revealed. Therefore, other intermediate species, such as CH, NO, and PAHs with different rings, are needed to be detected in future to further understand the HCCI and LTC.

Secondly, high-speed and simultaneous multi-species measurements are needed to improve in future. In current studies, high-speed measurements only focus on chemiluminescence or natural luminosity, but these optical diagnostics have low spatial resolution. However, as using laser diagnostics, it has high spatial resolution but low time resolution. Therefore, the combination between high time and spatial resolution to detect the combustion process is the development direction in future for HCCI and LTC. Meanwhile, the optical diagnostics in HCCI and LTC need to capture more species in the same engine cycle. For example, the simultaneous measurements on formaldehyde, OH, PAHs, and soot will give more detailed and complete mechanism on combustion chemical reaction.

Thirdly, the combustion processes in HCCI and LTC mode are primary controlled by chemical kinetics, and thus a large amount of studies are aiming to propose different chemical kinetic reaction mechanism. However, there is little attention on effects of flow or turbulence on combustion processes. For HCCI, even if it is a homogeneous combustion, there is still inhomogeneous charge in local area; therefore how the turbulence affects the local combustion is still an open question. The same question also lies in the LTC conditions. Furthermore, the mixing process has larger effect on LTC processes compared with HCCI conditions; therefore some recent studies have published some works on effects of turbulence on combustion and emissions by Wang et al. [108] and Perini et al. [109]. Obviously, more detailed measurements especially on local turbulence are necessary to clarify the effect of turbulence.

## Conflict of Interests

The authors declare that there is no conflict of interests regarding the publication of this paper.

## Acknowledgment

The authors would like to acknowledge the financial supports to the research provided by National Basic Research Program of China (973 Program) through its Project of 2013CB228402.

## References

- [1] M. Noguchi, Y. Tanaka, T. Tanaka, and Y. Takeuchi, "A study on gasoline engine combustion by observation of intermediate reactive products during combustion," SAE Paper 790840, 1979.
- [2] M. Yao, Z. Zheng, and H. Liu, "Progress and recent trends in homogeneous charge compression ignition (HCCI) engines," *Progress in Energy and Combustion Science*, vol. 35, no. 5, pp. 398–437, 2009.
- [3] J. E. Dec, "Advanced compression-ignition engines—understanding the in-cylinder processes," *Proceedings of the Combustion Institute*, vol. 32, pp. 2727–2742, 2009.
- [4] M. P. B. Musculus, P. C. Miles, and L. M. Pickett, "Conceptual models for partially premixed low-temperature diesel combustion," *Progress in Energy and Combustion Science*, vol. 39, no. 2–3, pp. 246–283, 2013.
- [5] N. P. Komninos and C. D. Rakopoulos, "Modeling HCCI combustion of biofuels: a review," *Renewable & Sustainable Energy Reviews*, vol. 16, no. 3, pp. 1588–1610, 2012.
- [6] M. Richter, J. Engström, A. Franke, M. Aldén, A. Hultqvist, and B. Johansson, "The influence of charge inhomogeneity on the HCCI combustion process," SAE Paper 2000-01-2868, 2000.
- [7] M. Richter, A. Franke, M. Aldén, A. Hultqvist, and B. Johansson, "Optical diagnostics applied to a naturally aspirated homogeneous charge compression ignition engine," SAE Paper 1999-01-3649, 1999.
- [8] K. Kumano, Y. Yamasaki, and N. Iida, "An investigation of the effect of charge inhomogeneity on the ignition and combustion processes in a HCCI engine using chemiluminescence imaging," *Journal of Thermal Science & Technology*, vol. 2, no. 2, pp. 200–211, 2007.
- [9] J. Kodavasal, D. N. Assanis, G. A. Lavoie, and J. B. Martz, "The effects of thermal and compositional stratification on the ignition and duration of homogeneous charge compression ignition combustion," *Combustion & Flame*, vol. 162, no. 2, pp. 451–461, 2015.
- [10] D. Dahl, M. Andersson, and I. Denbratt, "The role of charge stratification for reducing ringing in gasoline engine homogeneous charge compression ignition combustion investigated by optical imaging," *International Journal of Engine Research*, vol. 14, no. 5, pp. 525–536, 2013.
- [11] A. Krisman, E. R. Hawkes, S. Kook, M. Sjöberg, and J. E. Dec, "On the potential of ethanol fuel stratification to extend the high load limit in stratified-charge compression-ignition engines," *Fuel*, vol. 99, no. 9, pp. 45–54, 2012.
- [12] C. H. Lee and K. H. Lee, "An experimental study of the combustion characteristics in SCCI and CAI based on direct-injection gasoline engine," *Experimental Thermal and Fluid Science*, vol. 31, no. 8, pp. 1121–1132, 2007.
- [13] C. S. Lee, K. H. Lee, and D. S. Kim, "Experimental and numerical study on the combustion characteristics of partially premixed charge compression ignition engine with dual fuel," *Fuel*, vol. 82, no. 5, pp. 553–560, 2003.
- [14] M. Y. Kim, J. H. Lee, and C. S. Lee, "Combustion characteristics and  $NO_x$  emissions of a dimethyl-ether-fueled premixed charge compression ignition engine," *Energy and Fuels*, vol. 22, no. 6, pp. 4206–4212, 2008.
- [15] M. Jia, M. Xie, H. Liu, W.-H. Lam, and T. Wang, "Numerical simulation of cavitation in the conical-spray nozzle for diesel premixed charge compression ignition engines," *Fuel*, vol. 90, no. 8, pp. 2652–2661, 2011.
- [16] S. Choi and K. Min, "Analysis of the combustion and emissions of a diesel engine in early-injection, partially-premixed charge compression ignition regimes," *Proceedings of the Institution of Mechanical Engineers, Part D: Journal of Automobile Engineering*, vol. 227, no. 7, pp. 939–950, 2013.
- [17] H. Kim, K. Kim, and K. Lee, "Reduction in harmful emissions using a two-stage injection-type premixed charge compression

- ignition engine," *Environmental Engineering Science*, vol. 26, no. 11, pp. 1567–1576, 2009.
- [18] H. Kim, J. Lee, K. Kim, and K. Lee, "Effect of the atkinson cycle combined with calibration factors on a two-stage injection-type premixed charge compression ignition engine," *Energy and Fuels*, vol. 23, no. 10, pp. 4908–4916, 2009.
- [19] M. P. B. Musculus, "Multiple simultaneous optical diagnostic imaging of early-injection low-temperature combustion in a heavy-duty diesel engine," SAE Paper 2006-01-0079, 2006.
- [20] K. Akihama, Y. Takatori, K. Inagaki, S. Sasaki, and A. M. Dean, "Mechanism of the smokeless rich diesel combustion by reducing temperature," *SAE Transactions*, vol. 110, no. 3, pp. 648–662, 2001.
- [21] T. Lachaux and M. P. B. Musculus, "In-cylinder unburned hydrocarbon visualization during low-temperature compression-ignition engine combustion using formaldehyde PLIF," *Proceedings of the Combustion Institute*, vol. 31, no. 2, pp. 2921–2929, 2007.
- [22] A. S. Cheng, B. T. Fisher, G. C. Martin, and C. J. Mueller, "Effects of fuel volatility on early direct-injection, low-temperature combustion in an optical diesel engine," *Energy & Fuels*, vol. 24, no. 3, pp. 1538–1551, 2010.
- [23] T. Fang, R. E. Coverdill, C.-F. F. Lee, and R. A. White, "Low-temperature combustion within a HSDI diesel engine using multiple-injection strategies," *Transactions of the Asme—Journal of Engineering for Gas Turbines and Power*, vol. 131, no. 6, Article ID 062803, 2009.
- [24] T. Fang, Y.-C. Lin, M. F. Tien, and C.-F. Lee, "Reducing NO<sub>x</sub> emissions from a biodiesel-fueled engine by use of low-temperature combustion," *Environmental Science & Technology*, vol. 42, no. 23, pp. 8865–8870, 2008.
- [25] H. Liu, J. Xu, Z. Zheng, S. Li, and M. Yao, "Effects of fuel properties on combustion and emissions under both conventional and low temperature combustion mode fueling 2,5-dimethylfuran/diesel blends," *Energy*, vol. 62, pp. 215–223, 2013.
- [26] H. Liu, S. Li, Z. Zheng, J. Xu, and M. Yao, "Effects of n-butanol, 2-butanol, and methyl octynoate addition to diesel fuel on combustion and emissions over a wide range of exhaust gas recirculation (EGR) rates," *Applied Energy*, vol. 112, pp. 246–256, 2013.
- [27] J. E. Dec, "A conceptual model of D.I. diesel combustion based on laser-sheet imaging," *SAE Transactions*, vol. 106, no. 3, pp. 1319–1348, 1997.
- [28] C. Espey, J. E. Dec, and T. A. Litzinger, "Quantitative 2-D fuel vapor concentration imaging in a firing D.I. diesel engine using planar laser-induced Rayleigh scattering," *SAE Transactions*, vol. 103, no. 3, pp. 1145–1160, 1994.
- [29] J. T. Kashdan, N. Docquier, and G. Bruneaux, "Mixture preparation and combustion via LIEF and LIF of combustion radicals in a direct-injection HCCI diesel engine," SAE Paper 2004-01-2945, 2004.
- [30] T.-G. Fang, R. E. Coverdill, C.-F. F. Lee, and R. A. White, "Effect of the injection angle on liquid spray development in a high-speed direct-injection optical diesel engine," *Proceedings of the Institution of Mechanical Engineers, Part D: Journal of Automobile Engineering*, vol. 223, no. 8, pp. 1077–1092, 2009.
- [31] T. Fang, R. E. Coverdill, C.-F. F. Lee, and R. A. White, "Effects of injection angles on combustion processes using multiple injection strategies in an HSDI diesel engine," *Fuel*, vol. 87, no. 15–16, pp. 3232–3239, 2008.
- [32] T. Fang and C.-F. F. Lee, "Low sooting combustion of narrow-angle wall-guided sprays in an HSDI diesel engine with retarded injection timings," *Fuel*, vol. 90, no. 4, pp. 1449–1456, 2011.
- [33] H. Liu, S. Ma, Z. Zhang, Z. Zheng, and M. Yao, "Study of the control strategies on soot reduction under early-injection conditions on a diesel engine," *Fuel*, vol. 139, pp. 472–481, 2015.
- [34] R. Kiplimo, E. Tomita, N. Kawahara, and S. Yokobe, "Effects of spray impingement, injection parameters, and EGR on the combustion and emission characteristics of a PCCI diesel engine," *Applied Thermal Engineering*, vol. 37, pp. 165–175, 2012.
- [35] R. R. Steeper and S. de Zilwa, "Improving the NO<sub>x</sub>-CO<sub>2</sub> trade-off of an HCCI engine using a multi-hole injector," SAE Technical Paper 2007-01-0180, 2007.
- [36] H. Liu, M. Huo, Y. Liu et al., "Time-resolved spray, flame, soot quantitative measurement fueling n-butanol and soybean biodiesel in a constant volume chamber under various ambient temperatures," *Fuel*, vol. 133, pp. 317–325, 2014.
- [37] S. Kokjohn, R. Reitz, D. Splitter, and M. Musculus, "Investigation of fuel reactivity stratification for controlling PCI heat-release rates using high-speed chemiluminescence imaging and fuel tracer fluorescence," *SAE Technical Papers*, vol. 5, no. 2, pp. 248–269, 2012.
- [38] Z. Chen, M. Yao, Z. Zheng, and Q. Zhang, "Experimental and numerical study of methanol/dimethyl ether dual-fuel compound combustion," *Energy and Fuels*, vol. 23, no. 5, pp. 2719–2730, 2009.
- [39] S. Ma, Z. Zheng, H. Liu, Q. Zhang, and M. Yao, "Experimental investigation of the effects of diesel injection strategy on gasoline/diesel dual-fuel combustion," *Applied Energy*, vol. 109, no. 2, pp. 202–212, 2013.
- [40] H. Liu, X. Wang, Z. Zheng, J. Gu, H. Wang, and M. Yao, "Experimental and simulation investigation of the combustion characteristics and emissions using n-butanol/biodiesel dual-fuel injection on a diesel engine," *Energy*, vol. 74, pp. 741–752, 2014.
- [41] S. L. Kokjohn, R. M. Hanson, D. A. Splitter, and R. D. Reitz, "Fuel reactivity controlled compression ignition (RCCI): a pathway to controlled high-efficiency clean combustion," *International Journal of Engine Research*, vol. 12, no. 3, pp. 209–226, 2011.
- [42] X. Lu, J. Ma, L. Ji, and Z. Huang, "Simultaneous reduction of NO<sub>x</sub> emission and smoke opacity of biodiesel-fueled engines by port injection of ethanol," *Fuel*, vol. 87, no. 7, pp. 1289–1296, 2008.
- [43] Y. J. Kim, K. B. Kim, and K. H. Lee, "Effect of a 2-stage injection strategy on the combustion and flame characteristics in a PCCI engine," *International Journal of Automotive Technology*, vol. 12, no. 5, pp. 639–644, 2011.
- [44] W. H. Su and W. B. Yu, "Effects of mixing and chemical parameters on thermal efficiency in a partly premixed combustion diesel engine with near-zero emissions," *International Journal of Engine Research*, vol. 13, no. 3, pp. 188–198, 2012.
- [45] X. G. Wang, Z. H. Huang, O. A. Kuti, W. Zhang, and K. Nishida, "An experimental investigation on spray, ignition and combustion characteristics of biodiesels," *Proceedings of the Combustion Institute*, vol. 33, no. 2, pp. 2071–2077, 2011.
- [46] X. G. Wang, Z. H. Huang, W. Zhang, O. A. Kuti, and K. Nishida, "Effects of ultra-high injection pressure and micro-hole nozzle on flame structure and soot formation of impinging diesel spray," *Applied Energy*, vol. 88, no. 5, pp. 1620–1628, 2011.
- [47] I. Glassman, *Combustion*, Academic Press, New York, NY, USA, 3rd edition, 1996.

- [48] J. E. Dec and C. Espey, "Chemiluminescence imaging of auto-ignition in a DI diesel engine," SAE Technical Paper 982685, 1998.
- [49] A. G. Gaydon, *The Spectroscopy of Flames*, Chapman & Sons, 2nd edition, 1974.
- [50] A. Hultqvist, M. Christensen, B. Johansson, A. Franke, M. Richter, and M. Aldén, "A study of the homogeneous charge compression ignition combustion process by chemiluminescence imaging," SAE Paper 1999-01-3680, 1999.
- [51] B. Kim, M. Kaneko, Y. Ikeda, and T. Nakajima, "Detailed spectral analysis of the process of HCCI combustion," *Proceedings of the Combustion Institute*, vol. 29, no. 1, pp. 671–677, 2002.
- [52] R. Augusta, D. E. Foster, J. B. Ghandhi, J. Eng, and P. M. Najt, "Chemiluminescence measurements of homogeneous charge compression ignition (HCCI) combustion," SAE Paper 2006-01-1520, 2006.
- [53] H.-F. Liu, M.-F. Yao, C. Jin, P. Zhang, Z.-M. Li, and Z.-Q. Zheng, "Chemiluminescence spectroscopic analysis of homogeneous charge compression ignition combustion processes," *Spectroscopy and Spectral Analysis*, vol. 30, no. 10, pp. 2611–2615, 2010.
- [54] E. Murase, K. Hanada, T. Miyaura, and J. Ikeda, "Photographic observation and emission spectral analysis of homogeneous charge compression ignition combustion," *Combustion Science and Technology*, vol. 177, no. 9, pp. 1699–1723, 2005.
- [55] E. Mancaruso and B. M. Vaglieco, "Optical investigation of the combustion behaviour inside the engine operating in HCCI mode and using alternative diesel fuel," *Experimental Thermal & Fluid Science*, vol. 34, no. 3, pp. 346–351, 2010.
- [56] J. E. Dec, W. Hwang, and M. Sjöberg, "An investigation of thermal stratification in HCCI engines using chemiluminescence imaging," SAE Technical Paper 2006-01-1518, 2006.
- [57] W. Hwang, J. Dec, and M. Sjöberg, "Spectroscopic and chemical-kinetic analysis of the phases of HCCI autoignition and combustion for single- and two-stage ignition fuels," *Combustion & Flame*, vol. 154, no. 3, pp. 387–409, 2008.
- [58] J. B. Heywood, *Internal Combustion Engine Fundamentals*, McGraw-Hill, New York, NY, USA, 1988.
- [59] N. Peters, *Turbulent Combustion*, Cambridge Monographs on Mechanics, Cambridge University Press, Cambridge, UK, 2000.
- [60] A. Hultqvist, M. Christensen, B. Johansson et al., "The HCCI combustion process in a single cycle-high-speed fuel tracer LIF and chemiluminescence imaging," SAE Paper 2002-01-0424, SAE International, 2002.
- [61] A. Vressner, A. Hultqvist, and B. Johansson, "Study on the combustion chamber geometry effects in an HCCI engine using high-speed cycle-resolved chemiluminescence imaging," SAE Paper 2007-01-0217, 2007.
- [62] H. Liu, P. Zhang, Z. Li, J. Luo, Z. Zheng, and M. Yao, "Effects of temperature inhomogeneities on the HCCI combustion in an optical engine," *Applied Thermal Engineering*, vol. 31, no. 14-15, pp. 2549–2555, 2011.
- [63] H. Liu, Z. Zheng, M. Yao, P. Zhang, B. He, and Y. Qi, "Influence of temperature and mixture stratification on HCCI combustion using chemiluminescence images and CFD analysis," *Applied Thermal Engineering*, vol. 33-34, no. 1, pp. 135–143, 2012.
- [64] P. G. Aleiferis, A. G. Charalambides, Y. Hardalupas, A. M. K. P. Taylor, and Y. Urata, "Modelling and experiments of HCCI engine combustion with charge stratification and internal EGR," SAE Paper 2005-01-3725, 2005.
- [65] A. W. Berntsson and I. Denbratt, "HCCI combustion using charge stratification for combustion control," SAE Technical Paper 2007-01-0210, 2007.
- [66] S. Kook and C. Bae, "Combustion control using two-stage diesel fuel injection in a single-cylinder PCCI engine," SAE Paper 2004-01-0938, 2004.
- [67] A. Upatnieks, C. J. Mueller, and G. C. Martin, "The influence of charge-gas dilution and temperature on DI diesel combustion processes using a short-ignition-delay, oxygenated fuel," SAE 2005-01-2088, 2005.
- [68] H. Liu, C.-F. F. Lee, M. Huo, and M. Yao, "Combustion characteristics and soot distributions of neat butanol and neat soybean biodiesel," *Energy & Fuels*, vol. 25, no. 7, pp. 3192–3203, 2011.
- [69] Z. Zheng, L. Yue, H. Liu, Y. Zhu, X. Zhong, and M. Yao, "Effect of two-stage injection on combustion and emissions under high EGR rate on a diesel engine by fueling blends of diesel/gasoline, diesel/n-butanol, diesel/gasoline/n-butanol and pure diesel," *Energy Conversion and Management*, vol. 90, pp. 1–11, 2015.
- [70] Z. Zheng, C. Li, H. Liu, Y. Zhang, X. Zhong, and M. Yao, "Experimental study on diesel conventional and low temperature combustion by fueling four isomers of butanol," *Fuel*, vol. 141, pp. 109–119, 2015.
- [71] A. Upatnieks and C. J. Mueller, "Controlled DI diesel combustion using dilute, cool charge gas and a short-ignition-delay, oxygenated fuel," SAE Technical Paper 2005-01-0363, 2005.
- [72] C. J. Mueller and A. Upatnieks, "Dilute clean diesel combustion achieves low emissions and high efficiency while avoiding control problems of HCCI," in *Proceedings of the 11th Annual Diesel Engine Emissions Reduction Conference (DEER '05)*, Chicago, Ill, USA, August 2005.
- [73] H. Liu, X. Bi, M. Huo, C.-F. F. Lee, and M. Yao, "Soot emissions of various oxygenated biofuels in conventional diesel combustion and low temperature combustion conditions," *Energy & Fuels*, vol. 26, no. 3, pp. 1900–1911, 2012.
- [74] H. Liu, C.-F. Lee, M. Huo, and M. Yao, "Comparison of ethanol and butanol as additives in soybean biodiesel using a constant volume combustion chamber," *Energy & Fuels*, vol. 25, no. 4, pp. 1837–1846, 2011.
- [75] X. Bi, H. Liu, M. Huo, C. Shen, X. Qiao, and C.-F. F. Lee, "Experimental and numerical study on soot formation and oxidation by using diesel fuel in constant volume chamber with various ambient oxygen concentrations," *Energy Conversion and Management*, vol. 84, pp. 152–163, 2014.
- [76] R. Collin, J. Nygren, M. Richter, M. Aldén, L. Hildingsson, and B. Johansson, "Simultaneous OH- and formaldehyde-LIF measurements in an HCCI engine," SAE Technical Paper 2003-01-3218, 2003.
- [77] G. Särner, M. Richter, M. Aldén, L. Hildingsson, A. Hultqvist, and B. Johansson, "Simultaneous PLIF measurements for visualization of formaldehyde- and fuel-distributions in a DI HCCI engine," SAE Paper 2005-01-3869, 2005.
- [78] H. Zhao, Z. Peng, and T. Ma, "Investigation of the HCCI/CAI combustion process by 2-D PLIF imaging of formaldehyde," SAE Paper 2004-01-1901, 2004.
- [79] J. T. Kashdan and J. F. Papagni, "LIF imaging of auto-ignition and combustion in a direct-injection, diesel-fuelled HCCI engine," SAE Technical Paper 2005-01-3739, 2005.
- [80] L. Hildingsson, H. Persson, B. Johansson et al., "Optical diagnostics of HCCI and UNIBUS using 2-D PLIF of OH and formaldehyde," SAE Paper 2005-01-0175, 2005.
- [81] A. W. Berntsson and I. Denbratt, "Optical study of HCCI combustion using NVO and an SI stratified charge," SAE Paper 2007-24-0012, SAE International, 2007.

- [82] A. W. Berntsson, M. Andersson, D. Dahl, and I. Denbratt, "A LIF-study of OH in the negative valve overlap of a spark-assisted HCCI combustion engine," SAE Paper 2008-01-0037, 2008.
- [83] C. Schulz, J. B. Jeffries, D. F. Davidson, J. D. Koch, J. Wolfrum, and R. K. Hanson, "Impact of UV absorption by CO<sub>2</sub> and H<sub>2</sub>O on NO LIF in high-pressure combustion applications," *Proceedings of the Combustion Institute*, vol. 29, no. 2, pp. 2735–2742, 2002.
- [84] C. Schulz, J. D. Koch, D. F. Davidson, J. B. Jeffries, and R. K. Hanson, "Ultraviolet absorption spectra of shock-heated carbon dioxide and water between 900 and 3050 K," *Chemical Physics Letters*, vol. 355, no. 1-2, pp. 82–88, 2002.
- [85] W. G. Bessler, C. Schulz, T. Lee, J. B. Jeffries, and R. K. Hanson, "Strategies for laser-induced fluorescence detection of nitric oxide in high pressure flames. I. A – X(0, 0) excitation," *Applied Optics*, vol. 41, no. 18, pp. 3547–3557, 2002.
- [86] W. G. Bessler, C. Schulz, T. Lee, J. B. Jeffries, and R. K. Hanson, "Strategies for laser-induced fluorescence detection of nitric oxide in high pressure flames. II. A – X(0, 1) excitation," *Applied Optics*, vol. 42, no. 12, pp. 2031–2042, 2003.
- [87] W. G. Bessler, C. Schulz, T. Lee, J. B. Jeffries, and R. K. Hanson, "Strategies for laser-induced fluorescence detection of nitric oxide in high-pressure flames. III. Comparison of A-X excitation schemes," *Applied Optics*, vol. 42, no. 24, pp. 4922–4936, 2003.
- [88] J. E. Dec and R. E. Canaan, "PLIF imaging of NO formation in a DI diesel engine," SAE Technical Paper 980147, 1998.
- [89] K. Akihama, T. Fujikawa, and Y. Hattori, "Laser-induced fluorescence imaging of no in a port-fuel-injected, stratified-charge SI engine—correlations between N formation region and stratified fuel distribution," SAE Paper 981430, 1998.
- [90] F. Hildenbrand, C. Schulz, J. Wolfrum, F. Keller, and E. Wagner, "Laser diagnostic analysis of NO formation in a direct injection diesel engine with pump-line-nozzle and common rail injection systems," *Proceedings of the Combustion Institute*, vol. 28, no. 1, pp. 1137–1144, 2000.
- [91] W. G. Bessler, M. Hofmann, F. Zimmermann et al., "Quantitative in-cylinder NO-LIF imaging in a realistic gasoline engine with spray-guided direct injection," *Proceedings of the Combustion Institute*, vol. 30, no. 2, pp. 2667–2674, 2005.
- [92] S. D. Zilwa and R. Steeper, "Predicting emissions from HCCI engines using LIF imaging," SAE Paper 2005-01-3747, SAE International, 2005.
- [93] S. D. Zilwa and R. Steeper, "Predicting NO<sub>x</sub> emissions from HCCI engines using LIF imaging," SAE Paper 2006-01-0025, 2006.
- [94] S. Singh, R. D. Reitz, and P. B. M. Mark, "2-color thermometry experiments and high-speed imaging of multi-mode diesel engine combustion," SAE Technical Paper 2005-01-3842, 2005.
- [95] E. Huestis, P. A. Erichson, and M. P. B. Musculus, "In-cylinder and exhaust soot in low-temperature combustion using a wide-range of EGR in a heavy-duty diesel engine," SAE Paper 2007-01-4017, 2007.
- [96] J. E. Dec and E. B. Coy, "OH radical imaging in a DI diesel engine and the structure of the early diffusion flame," *SAE Transactions*, vol. 105, no. 3, pp. 1127–1148, 1996.
- [97] J. E. Dec and D. R. Tree, "Diffusion-flame/wall interactions in a heavy-duty DI diesel engine," *SAE Transactions*, vol. 110, no. 3, pp. 1618–1634, 2001.
- [98] J. E. Dec and P. L. Kelly-Zion, "The effects of injection timing and diluent addition on late-combustion soot burnout in a DI diesel engine based on simultaneous 2-D imaging of OH and soot," SAE Technical Paper 2000-01-0238, 2000.
- [99] Q.-L. Tang, P. Zhang, H.-F. Liu, and M.-F. Yao, "Quantitative measurements of soot volume fractions in diesel engine using laser-induced incandescence method," *Acta Physico-Chimica Sinica*, vol. 31, no. 5, pp. 980–988, 2015.
- [100] M. Xiao, H. Liu, X. Bi, H. Wang, and C.-F. F. Lee, "Experimental and numerical investigation on soot behavior of soybean biodiesel under ambient oxygen dilution in conventional and low-temperature flames," *Energy and Fuels*, vol. 28, no. 4, pp. 2663–2676, 2014.
- [101] J. Zhang, W. Jing, W. L. Roberts, and T. Fang, "Effects of ambient oxygen concentration on biodiesel and diesel spray combustion under simulated engine conditions," *Energy*, vol. 57, pp. 722–732, 2013.
- [102] J. Zhang, W. Jing, W. L. Roberts, and T. Fang, "Soot temperature and KL factor for biodiesel and diesel spray combustion in a constant volume combustion chamber," *Applied Energy*, vol. 107, pp. 52–65, 2013.
- [103] I. Ekoto, W. Colban, P. Miles, S. Park, and D. E. Foster, "Sources of UHC emissions from a light-duty diesel engine operating in a partially premixed combustion regime," *SAE International Journal of Engines*, vol. 2, no. 1, pp. 1265–1289, 2009.
- [104] I. W. Ekoto, W. F. Colban, P. C. Miles et al., "UHC and CO emissions sources from a light-duty diesel engine undergoing late-injection low-temperature combustion," in *Proceedings of the ASME Internal Combustion Engine Division Fall Technical Conference (ICEF '09)*, Paper no. ICEF2009-14030, pp. 163–172, Lucerne, Switzerland, September 2009.
- [105] B. Petersen, P. Miles, and D. Sahoo, "Equivalence ratio distributions in a light-duty diesel engine operating under partially premixed conditions," *SAE International Journal of Engines*, vol. 5, no. 2, pp. 526–537, 2012.
- [106] B. Li, M. Jonsson, M. Algotsson et al., "Quantitative detection of hydrogen peroxide in an HCCI engine using photofragmentation laser-induced fluorescence," *Proceedings of the Combustion Institute*, vol. 34, no. 2, pp. 3573–3581, 2013.
- [107] P. Zhang, H.-F. Liu, B.-L. Chen, Q.-L. Tang, and M.-F. Yao, "Fluorescence spectra of polycyclic aromatic hydrocarbons and soot concentration in partially premixed flames of diesel surrogate containing oxygenated additives," *Acta Physico-Chimica Sinica*, vol. 31, no. 1, pp. 32–40, 2015.
- [108] B. L. Wang, C. W. Lee, R. D. Reitz, P. C. Miles, and Z. Han, "A generalized renormalization group turbulence model and its application to a light-duty diesel engine operating in a lower-temperature combustion regime," *International Journal of Engine Research*, vol. 14, no. 3, pp. 279–292, 2013.
- [109] F. Perini, P. C. Miles, and R. D. Reitz, "A comprehensive modeling study of in-cylinder fluid flows in a high-swirl, light-duty optical diesel engine," *Computers & Fluids*, vol. 105, pp. 113–124, 2014.

## Research Article

# Adsorption of Polymeric Additives Based on Vinyl Acetate Copolymers as Wax Dispersant and Its Relevance to Polymer Crystallization Mechanisms

Ayman M. Atta,<sup>1,2</sup> Rasha A. El-Ghazawy,<sup>2</sup> Fatma A. Morsy,<sup>3</sup>  
Ali M. S. Hebishy,<sup>3</sup> and Abdullah Elmorsy<sup>3</sup>

<sup>1</sup>Chemistry Department, College of Science, King Saud University, Riyadh 11451, Saudi Arabia

<sup>2</sup>Petroleum Application Department, Egyptian Petroleum Research Institute, Nasr City, Cairo, Egypt

<sup>3</sup>Chemistry Department, Faculty of Science, Helwan University, Helwan, Egypt

Correspondence should be addressed to Ayman M. Atta; [aatta@ksu.edu.sa](mailto:aatta@ksu.edu.sa)

Received 26 October 2014; Revised 13 March 2015; Accepted 1 April 2015

Academic Editor: Chao Jin

Copyright © 2015 Ayman M. Atta et al. This is an open access article distributed under the Creative Commons Attribution License, which permits unrestricted use, distribution, and reproduction in any medium, provided the original work is properly cited.

The present work has main target to study the effect of additives molecular weight and composition on the flow characteristics of wax crude oil at low temperature below pour point temperature. In this respect, maleic anhydride ester-co-vinyl acetate copolymers with varied monomers feed ratios and different alkyl ester lengths, namely, dodecyl, stearyl, and behenyl alkyl chains, were prepared. These polymeric materials were characterized by FTIR, <sup>1</sup>HNMR, and GPC. The performance of these additives as pour point depressants and flow improver for Egyptian waxy crude oil was evaluated through measurements of pour point and rheological parameters (viscosity and yield stress). It was observed that stearyl maleate-vinyl acetate copolymer with 1:2 feed ratio shows the best efficiency as pour point depressant even at low concentration while octadecyl maleate-vinyl acetate copolymers with 2:1 feed ratio are effective as flow improver.

## 1. Introduction

The paraffin deposition formed during production and transportation of light crude oil and natural gases and condensates is one of the main problems that affect the oil productivity especially at low temperature [1–3]. The crude oil constituents have pronounced effect on its flow characteristics with variation of the surrounding temperature. Egyptian crude oil contains different amounts of paraffin wax depending on the field and area of production. At low temperatures, crude oil containing high amounts of paraffin shows high pour points due to paraffin deposition; that is, paraffins tend to crystallize forming wax crystals. The wax deposition is a result of cooling down the crude oil below certain temperatures during transportation or storage. This temperature depends upon the constituents of crude oil and is called pour point temperature (PPT) [4]. The wax deposit on the walls of the pipeline causes many serious problems such as decreasing the effective diameter of the pipeline and even

pipeline blocking [5]. Thus, it is valuable from the economic point of view to minimize the effect of wax deposition. It is necessary to maintain the temperature of paraffin crude oil by insulation or heating which consumed more energy to prevent the crude oil treatments. The mechanical and thermal treatments have been used to control the paraffin deposition but these treatments consumed times and energy. The chemical treatments based on using pour point depressants, viscosity modifiers, flow improver, wax modifier, and asphaltene dispersant attracted great attention in oilfield chemicals to increase the oil transportation and productivity [6–9]. The literatures [10, 11] proved that these chemicals should have similar structure to paraffin to interact with paraffin and prevent their agglomeration in crude oils. Moreover, these additives should have polar functional groups to repulse each other to cocrystallize with paraffin and disperse them in crude oil.

Copolymerization is of great interest in synthesizing polymers with desired physical and chemical properties

TABLE 1: The physicochemical properties of Norpetco crude oil.

Test	Method	Result
API gravity at 60 F	ASTM D-1298	41.1
Specific gravity at 60/60 F	ASTM D-1298	0.820
Wax content (wt%)	UOP 46/64	8.4
Asphaltene content (wt%)	IP 143/84	3
Water content (vol%)	IP 74/70	0.23
Kinematic viscosity (cSt) at		
50°C	ASTM D-445	7
60°C		4.3
Pour point °C	QPC procedure	30

through controlling monomers ratio, their concentrations, and polymerization procedure. PPD is synthesized with two essential parts: oil soluble paraffinic chain and a polar moiety. The usefulness of paraffin chain is to cause nucleation and cocrystallization while the polar part controls the crystal growth and limits the size of wax crystals [12–15]. Vinyl acetate polymers such as vinyl acetate- $\alpha$ -olefin [16], poly-n-alkyl acrylates [1, 2], and methacrylate copolymers [17–19] have been used to improve crude oil flowability. The application of pour point depressants has also been described in several patents [20, 21]. More recently, pour point depressant effect on rheological behaviors of heavy and light Mexican crude oils was evaluated with various copolymers based on different combinations of vinyl acetate, styrene, and n-butyl acrylate [22]. This work aims to prepare vinyl acetate maleic anhydride copolymers having different monomer compositions using radical polymerization followed by esterification with different types of aliphatic alcohol to study the performance of the prepared copolymers as PPD additives for Egyptian waxy crude. Moreover, the efficiency of the prepared copolymers as flow improver was evaluated through rheology measurements of the treated crude oil. The effects of three modified polymers upon the deposition with a multicomponent wax of the tested crude oil were also investigated.

## 2. Experimental

**2.1. Materials.** Vinyl acetate, maleic anhydride, dodecyl alcohol (DA), stearyl alcohol (SA), behenyl alcohol (BA), benzoyl peroxide (BP), and P-toluene sulfonic acid monohydrate (PTSA) were purchased as analytical grade from Aldrich Chemicals Co., Germany. Benzene, dimethylformamide (DMF), and xylene were delivered from Adweic Chemicals Co., Egypt.

Egyptian waxy crude oil (Norpetco, Egypt) was delivered without treatment from Fardous field. The physicochemical characteristics and composition of Fardous mixed crude oils are listed in Table 1.

**2.2. Copolymerization.** Maleic anhydride-vinyl acetate copolymer was prepared by copolymerizing vinyl acetate (VA) and maleic anhydride (MA) in different molar feed ratios of VA:MA, namely, 1:1, 1:2, and 2:1, in reaction flask using

dry benzene as solvent and 1% (wt/wt) benzoyl peroxide (BP) as initiator. The reaction proceeds for 6 hours at 60–70°C with constant stirring under nitrogen atmosphere. After completion of polymerization, benzene was distilled off under vacuum. The copolymer was purified using benzene as solvent and petroleum ether as nonsolvent. The purified copolymer was dried at 60°C under vacuum.

**2.3. Esterification.** The reaction mixture containing 0.01 mol VA-MA copolymer solution in DMF, with one of the previously described molar ratios, and 0.02 mol of each alcohol (dodecyl, stearyl, or behenyl) was refluxed separately in presence of 0.1 (wt%) PTSA as a catalyst. The reaction was carried out at the refluxing temperature until theoretical amount of water was collected azeotropically in the Dean Stark trap that contains small amount of toluene to determine the amount of produced water. The resulting esters were washed out with water to remove the catalyst and any unreacted materials.

The prepared esters, dodecyl maleate-vinyl acetate (VADM) copolymers, stearyl maleate-vinyl acetate (VASM) copolymers, and behenyl maleate-vinyl acetate (VABM) copolymers were purified and used as additives for crude oil.

**2.4. Characterization.** The carbon distribution number of separated wax was determined using GC-Mass spectrometer.

<sup>1</sup>H NMR analysis were recorded on a Varian Gemini 2000 at 300 MHz and Fourier transform infrared (FTIR, Perkin-Bhaskar-Elmer Co., USA) spectrometers were used to determine the chemical structures of copolymers.

The molecular weight data of the prepared copolymers, such as the weight average molecular weights ( $M_w$ ), the number average molecular weights ( $M_n$ ), and polydispersity index, were characterized using Shimadzu's gel permeation chromatograph equipped with refractive index detector and polydivinylbenzene mix gel-D column. Tetrahydrofuran (THF) with a flow rate of 1 mL/min was used as mobile phase and polystyrene was used as the standard.

**2.5. Evaluation Tests.** Pour points measurements were determined using modified ASTM D-97 method without reheating to 45°C using different concentrations of the prepared additives, namely, 1000, 2000, 3000, 4000, and 5000 ppm. The effect of additive on the wax crystal morphologies was observed using an Olympus BX51 polarized-light microscope with a Linkam THMS 600 hot stage. The images were taken after transferring a small quantity of treated or untreated crude oil to glass slide inside a copper stage which has central window.

Viscosity and flow curves (rheogram) were measured using Brookfield viscometer equipped with thermostated cooling system for temperature adjustment [23]. Measurements were carried out at different temperatures below pour point of crude oils ranging from 21 to 12°C using 5000 ppm of each additive separately.

The yield stress measurements were determined from the relationship between shear stress and shear rate valued measured using Brookfield viscometer. Oil samples with or without additives were heated to 80°C, with the temperature

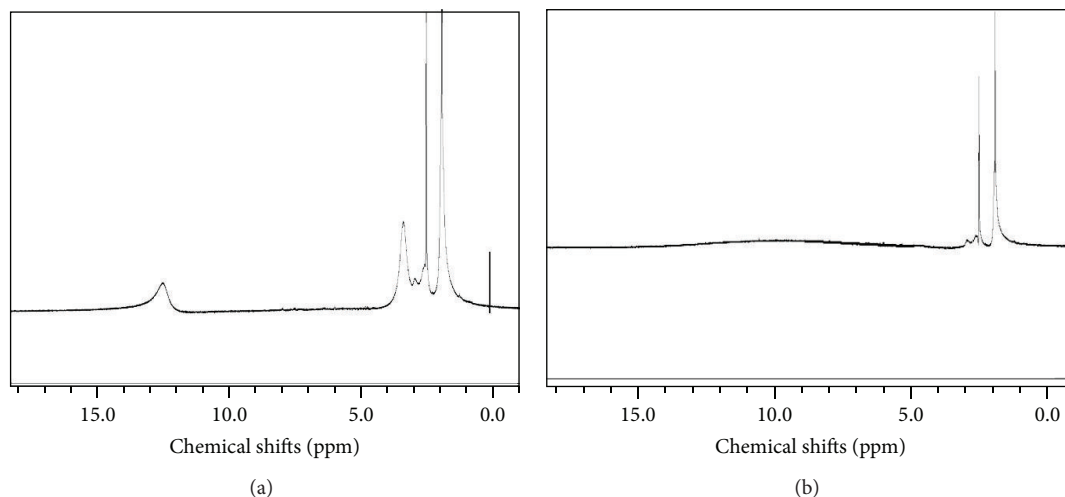


FIGURE 1:  $^1\text{H}$ NMR spectra of VA : MA having monomer feed compositions (a) (1 : 2) and (b) (1 : 1).

maintained for 5 min to adopt their thermal history. The temperature decreased by  $10^\circ\text{C}/\text{min}$  cooling rate to the experimental test temperature. The test temperature was determined from pour point measurements for both the crude oils and treated crude oils. The viscosity values were measured, after annealing the sample at the measurement temperature without shear for 5 min, by applying stress and incrementally increased every 10 s (100 stress increments per decade). The yield stress is defined as the stress below which no flow occurs.

### 3. Result and Discussion

Polymers including vinyl acetate (VA) and alkyl acrylate are used mainly as additives to improve the flow ability of waxy crude oil at low temperature. It is presumed that effective additives should match crude wax in structure, composition, and content. In this respect, we select vinyl acetate and maleic anhydride to prepare polymeric additives for Egyptian waxy crude oil. The main idea depends on variation of copolymer compositions by changing the monomer feed composition of VA : MA as 1 : 1, 1 : 2, and 2 : 1 followed by esterification with different types of n-alkanol such as dodecyl, stearyl, or behenyl alcohol. The chemical structure was designed on the previous results showing that VA copolymers containing from 20 to 40% w/w of vinyl acetate performed well when applied in some petroleum samples [1, 2]. Moreover, VA copolymers containing long side chains (from  $\text{C}_{12}$  to  $\text{C}_{18}$ ) have also presented good performance for other kinds of oil [24].

$^1\text{H}$ NMR spectra of maleic anhydride-vinyl acetate copolymer with different monomer feed composition are presented in Figure 1. The spectra show different chemical shifts at about 1.8 ppm for methyl protons, 2.4 ppm for methyl protons adjacent to ( $\text{C}=\text{O}$  group) in VA moieties, and 3.5 ppm for CH protons adjacent to the acetate group in VA moieties. The disappearance of vinyl group peaks in the range of chemical shift 4.5–6.5 ppm indicates polymerization of VA and MA. The appearance of peak at 12 ppm indicated the

TABLE 2: The average molecular weight of the prepared copolymer at different mole ratios.

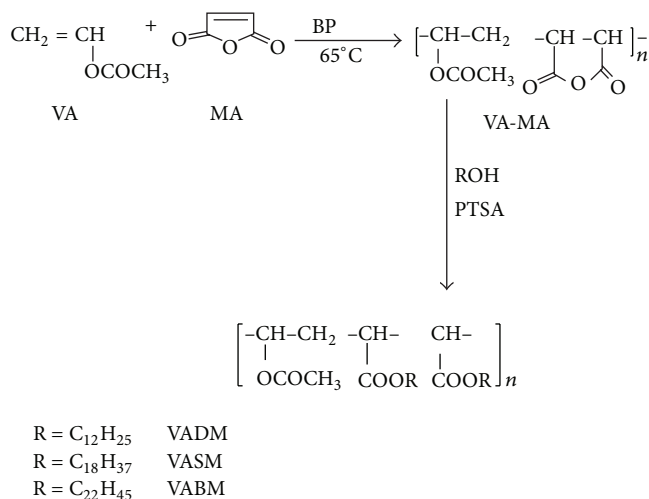
Polymer composition	Molecular weight (g/mol)		
	$M_w$	$M_n$	PD
VA-MA (1 : 1)	$1.13 \times 10^4$	$3.5 \times 10^3$	3.22
VA-MA (1 : 2)	$1.7 \times 10^4$	$4.7 \times 10^3$	3.61
VA-MA (2 : 1)	$9.65 \times 10^3$	$6.03 \times 10^3$	1.6

conversion of anhydride group to  $\text{COOH}$  groups for VA-MA copolymer compositions 2 : 1 and 1 : 2. Here, a conversion near 100% was determined by gravimetric measurements.

Molecular weights of the prepared polymers with the different feed ratios were determined using gel permeation chromatography (GPC) using THF as eluent and the results are summarized in Table 2. The molecular weight results indicated that the molecular weight slightly increase by increasing the maleic anhydride content.

**3.1. Esterification of VA-MA Copolymers.** Through this paper, three VA-MA copolymers were reacted with alkanol having different alkyl length using esterification reaction as illustrated in Scheme 1. The alkyl group introduced in VA-MA copolymers was used to increase the solubility of esterified copolymers in toluene and crude oil. The chemical structure of the esterified copolymer was confirmed by FTIR spectroscopy. In this respect, FTIR spectrum of VADM was selected as representative sample and represented in Figure 2. The FTIR spectrum shows strong absorption bands at  $1745\text{ cm}^{-1}$  (indicating the presence of  $\text{C}=\text{O}$  ester group) and disappearance of bands at about  $1810$  and  $1780\text{ cm}^{-1}$  and  $3500\text{ cm}^{-1}$  which is attributed to  $\text{C}=\text{O}$  stretching vibration of anhydride and OH of carboxylic maleic groups, respectively.  $3080\text{--}3150\text{ cm}^{-1}$  indicates the complete esterification of VA-MA copolymers [25].

In addition, the chemical structure of esterified VA-MA copolymers was confirmed by  $^1\text{H}$ NMR. Figure 3 represents



SCHEME 1: Synthesis of VA-MA ester copolymers.

the  $^1\text{H}$ NMR spectra of VADM, VASM, and VABM esters of VA-MA (1:2). Molecular characterization of the esterified copolymers was determined using the method outlined by Thamizharasi et al. [26] where a comparison of the intensity of some selected peaks was held to determine the copolymer compositions. The relative peak intensities were determined from peak areas calculated by means of electronic integration. In this respect, we select peaks at 12 ppm (attributed to COOH protons) and new peak observed at 3.9 ppm (referring to  $\text{CH}_2$  protons attached to COO of MA group) to confirm the esterification of VA-MA copolymers. The data indicate efficient esterification reaction of VA-MA copolymers with SA more than both BA and DA. The data indicated that the esterification of VA-MA with SA, DA, and BA was 100, 80, and 55%, respectively. This may be attributed to the difference in polarity and compatibility between the reactants, a factor that would affect the reactivity of the functional groups [27–29].

### 3.2. The Influence of Additive on Pour Point of Crude Oil.

It is common that all waxy crude oils eventually become nonfluid on chilling [30]. This is related to precipitation of wax crystals by chilling which interlock to form three-dimensional network. PPD are especially designed substance having hydrophobic moieties to change the rheology of crude oil and to facilitate the flow problems [31]. The efficiency of any polymeric additive used as pour point depressant is attributed to its ability to disperse the paraffin wax. It was previously reported that [32] the polymeric additives should have hydrophobic side chains and have strong interactions with crude oil to reduce their viscosity and enhance their ability to flow. Moreover, the average molecular weight distribution of additives should have broad distribution to cover the n-paraffin distribution. In addition, the performance of PPD depends on the characteristics of crude oil itself including total wax content, the chain length and shape (linear or branched), and quantity and type of wax present in crude [33]. In this respect, urea adduction method is used to isolate paraffin from crude oil to be analyzed with GLC as described

TABLE 3: The pour point of untreated crude oil and treated crude oil with VADM.

Copolymer composition	Pour point temperature ( $^\circ\text{C}$ ) at concentrations (ppm)					
	Nil	1000	2000	3000	4000	5000
VADM (1:1)	30	27	24	21	21	18
VADM (1:2)	30	30	27	24	24	21
VADM (2:1)	30	30	27	24	24	21

TABLE 4: The pour point of untreated crude oil and treated crude oil with VASM.

Copolymer composition	Pour point temperature ( $^\circ\text{C}$ ) at concentrations (ppm)					
	Nil	1000	2000	3000	4000	5000
VASM (1:1)	30	27	27	27	27	24
VASM (1:2)	30	15	15	12	12	12
VASM (2:1)	30	15	15	15	15	12

in the Experimental. The n-paraffin is determined as 12 wt.% from urea adduct method. Further analysis of n-paraffins by GLC for Norpetco crude oil was carried out to determine the carbon numbers as shown in Figure 4.

From data represented in Figure 4, the total carbon average of paraffin is 44 with broad molecular weight distribution. This means that the n-paraffin with C-44 tends to form precipitate and block the crude oil flow by forming interlocking networks. Accordingly, the side chains of polymers should have lengths resembling paraffin wax distributions to interact with paraffin and inhibit the formation of wax networks. The structure and composition of flow improvers should possess high polar functional groups such as amide, ester, amine, and hydroxyl groups. When an additive contains both long-chain hydrocarbon and polar moieties, it may be efficient as wax dispersant and flow improver. The mechanism of pour point depression has been well explained [34]; the PPD in crude oil changes the wax crystal shapes from extensively interlocking plates to more compact crystals by cocrystallizing with the wax. The more similar the polymer structure to wax components, the better its performance and the better its ability to attach to wax components and create a barrier for networking of wax particles.

The evaluation of the prepared copolymer esters as PPD was studied through preparation of crude oil samples treated with different concentrations from each additive, namely, 1000, 2000, 3000, 4000, and 5000 ppm. The results of pour point measurement are given in Tables 3, 4, and 5. The pour point data, given in Tables 3–5, show that the length of the alkyl chain affects the efficiency of polymeric additives. Generally, the most effective additives are the VASM and VADM showing a maximum of  $9^\circ\text{C}$  depression in pour point only at high dose of additive (5000 ppm), that is, low effectiveness as PPD, while in VASM the extent of depression in pour point reaches about  $18^\circ\text{C}$  at the same dose (5000 ppm). These results of pour point also showed that VASM with mol ratio (1:2) are the most efficient PPD.

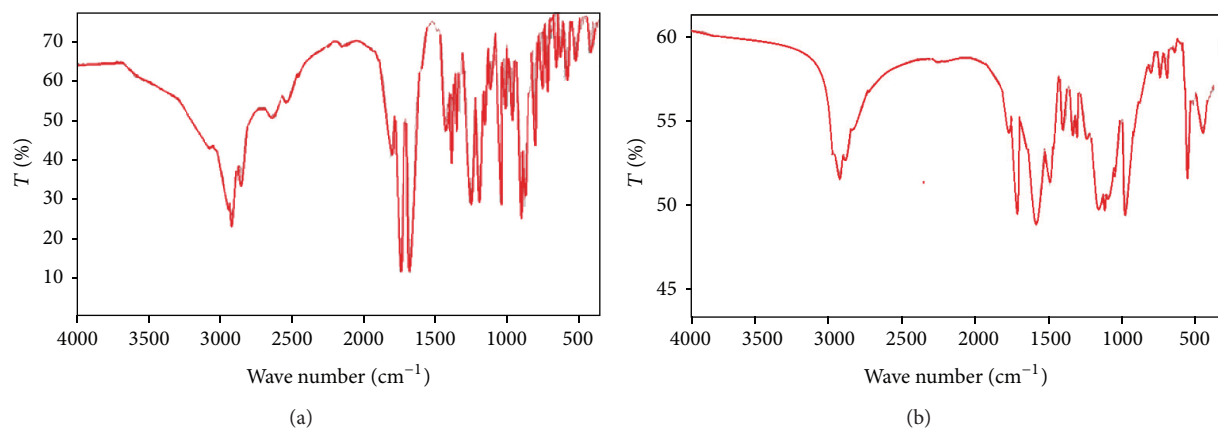


FIGURE 2: FTIR spectra of (a) VA-MA and (b) VADM copolymers.

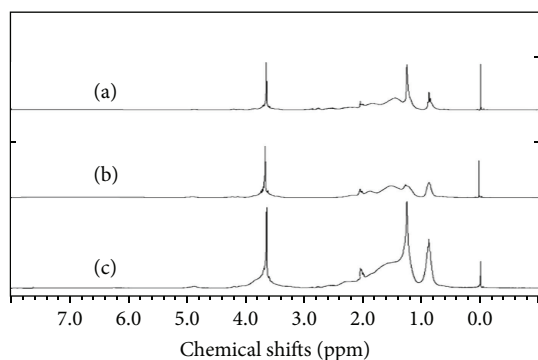
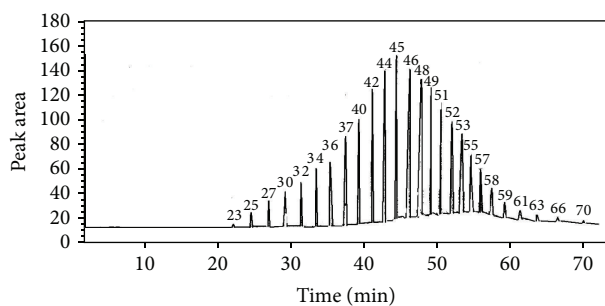
FIGURE 3: <sup>1</sup>H NMR spectra of (a) VASM, (b) VADM, and (c) VABM copolymers.

FIGURE 4: Chromatogram of paraffins extracted from Norpetco crude oil.

The higher efficiency of these esters can be correlated to the presence of higher alkyl side chain and to the percentage of esterification to VA content. This additive contains the highest maleic anhydride content and thus high dispersing activity as a result of combined effect of carbonyl oxygen of maleic anhydride and the polarity exerted by methoxy group in the polymers. However, regarding the performance of VABM, they do not show noticeable effect as PPD for this crude oil; this can be rationalized by the increased chain length which renders the polymer more bulky and less soluble

TABLE 5: The pour point of untreated crude oil and treated crude oil with VABM.

Copolymer composition	Pour point temperature (°C) at concentrations (ppm)					
	Nil	1000	2000	3000	4000	5000
VABM (1:1)	30	30	30	27	27	27
VABM (1:2)	30	30	30	27	27	24
VABM (2:1)	30	30	27	27	27	24

making it less effective. In other words, VABM may itself deposit acting as a nucleus for deposition of paraffin wax of crude oil.

The microscopic images of untreated and treated Norpetco crude oil with 5000 ppm of VASM (1:2) at the pour point temperature are shown in Figures 5(a) and 5(b). The wax crystals of untreated crude oil appeared agglomerated thin and feather-shaped which indicates the growth of wax crystals at nucleating sites (Figure 5(a)). These agglomerates will impart high surface energy to untreated crude oil and tend to interconnect into a three-dimensional network structure. This interaction increased the pour point of untreated crude oil. However, the addition of 5000 ppm VASM (1:2) modifies the crystal structure to globular morphologies (Figure 5(b)).

**3.3. The Impact of Additives on Rheology of Crude Oil.** The rheology is used to evaluate the crude oil flow ability in the absence and presence of the prepared polymeric additives. The rheological parameters for untreated and treated crude oil with 5000 ppm of VASM were determined at different temperatures, namely, 12°C, 15°C, and 21°C. Figures 6, 7, and 8 represent variation of shear stress as a function of shear rate. The Bingham plastic flow model is illustrated by the following equation: Shear stress (Pa) = Yield stress (Pa) + Shear rate ( $S^{-1}$ )  $\times$  plastic viscosity (mPas). The yield stress values of the treated crude oil in presence of 5000 ppm of VASM additives with different composition are displayed in Table 6. The data show that the tested crude oils possess high yield shear stress values at low temperature at and below their pour points. On

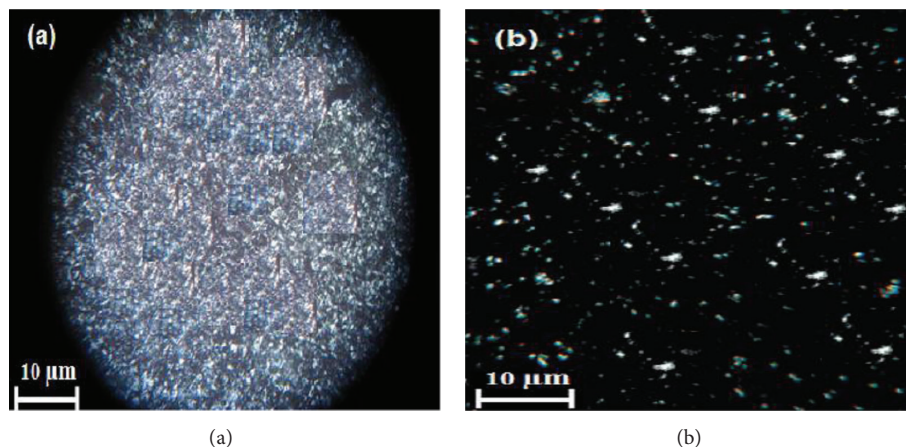


FIGURE 5: Polarized microscopic image morphologies of (a) untreated and (b) treated Norpetco crude oils with 5000 ppm of VASM (1:2) at their pour point temperatures.

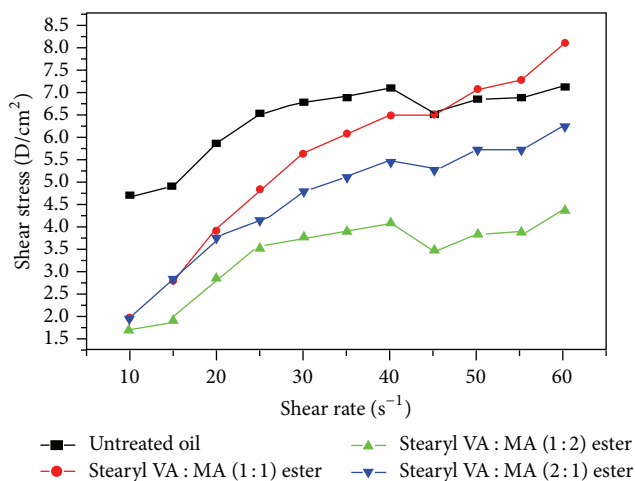


FIGURE 6: Rheogram of untreated and treated crude oil with 5000 ppm of different mol ratios at 12°C.

the other hand, it was observed that the viscosity of crude oils was increased with cooling. Therefore, the high wax content leads to the formation of gelled crude at low temperatures due to the crystallization of the wax which in turn affects the viscosity of crude oils.

Moreover, the long-chain alkyl grafts in VASM (2:1) have the same effect on the long-chain paraffins in the distribution of wax and paraffin in the crude oil. The possible reason for lowering the yield stress and pour point temperature is attributed to match of side alkyl chain length with the paraffin length of the tested crude oil. Moreover, the molecular weight of alkyl substituent has strong effect on the solubility of the additives in the crude oil. It is found that the VA-MA (2:1) ester copolymers have low polydisperse molecular weights and have moderate high molecular weight (Table 2), achieving the best low pour point temperature and yield stress results (Tables 3–6). This behavior was attributed to the effect of polymer molecular weights on the polymer radius of gyration and hence on the viscosity [24].

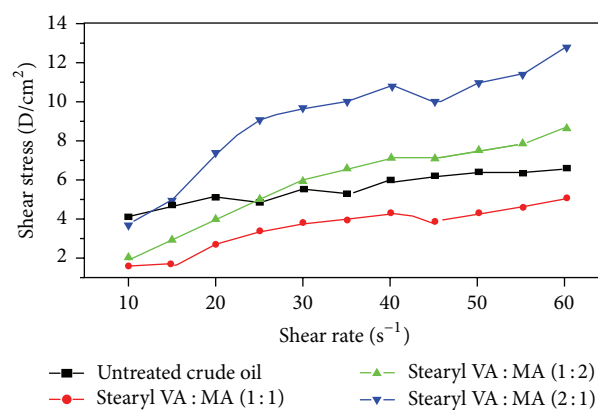


FIGURE 7: Rheogram of untreated and treated crude oil with 5000 ppm of different mol ratios at 15°C.

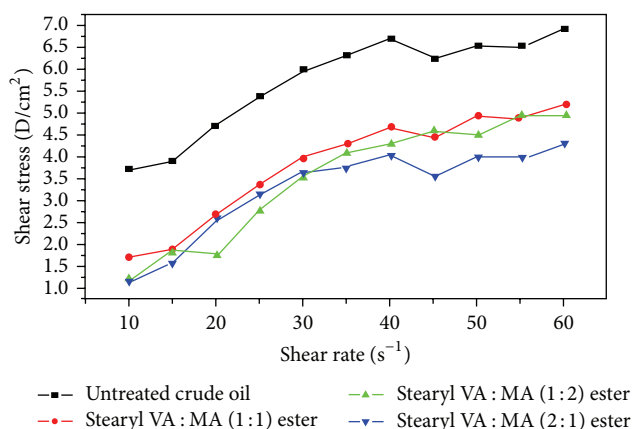


FIGURE 8: Rheogram of untreated and treated crude oil with 5000 ppm of different mol ratios at 21°C.

The apparent viscosities (mPaS) of the untreated and treated crude oils with VASM (2:1) were determined at different temperatures to evaluate the effect of the polymer

TABLE 6: Yield value of untreated and treated crude oil with 5000 ppm concentration of the additives of different composition.

Oil sample	$T$ ( $^{\circ}\text{C}$ )	Yield value (Dyne/cm <sup>2</sup> )
Untreated	12	4.89
	15	3.93
	21	3.52
VASM (1:1)	12	1.57
	15	1.36
	21	1.34
VASM (1:2)	12	1.83
	15	1.56
	21	1.19
VASM (2:1)	12	1.99
	15	1.50
	21	1.30

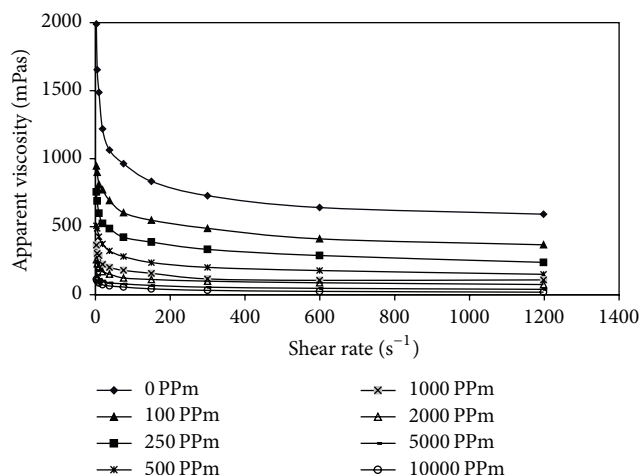


FIGURE 9: Effect of VASM (2:1) on the apparent viscosity on Norpetco crude oil at 15°C.

on the viscosities of Norpetco crude (representative samples are shown in Figure 9).

The values of the plastic viscosity (mPaS) and yield shear stress values (Pa) decreased by the addition of VASM (2:1) additives even at high concentrations (10,000 ppm). Figure 9 shows the variation of crude oil viscosity as a function of copolymer concentration at 15°C. It can be observed that high concentration of copolymer can effectively reduce the crude oil viscosity. In absence of PPD additives at this temperature range (below PPT of blank crude sample), paraffin crystals would be formed in the liquid media causing a non-Newtonian behavior of the oil. Upon treating crude samples with VASM (2:1) additives, Newtonian behavior can be observed even at this low temperature (15°C) for all tested crude oil samples at 10,000 ppm. This indicates that VASM (2:1) copolymer has the ability to disperse wax crystals and improve the flow behaviors of the tested crude oils as observed from the data listed in Table 6. These results are in good agreement with data on the polymeric additives [35–38] which decreased both pour point temperatures and the yield

shear stress. Finally we can conclude that the VASM (2:1) can act as flow improver for Egyptian waxy crude oils.

## 4. Conclusions

The new hydrophobically modified VASM copolymers achieve efficient PPD for the Egyptian waxy crude oil. The effective concentration of PPD to inhibit the wax deposition, to decrease the pour point temperature, and to improve the rheological characteristics of crude oils was found to be 100–10000 ppm. The composition of VASM greatly affects the performance of the additive with the copolymer VASM with mole ratio 1:2 which is the most efficient additive in pour point depression, while the copolymer VASM with mole ratio 2:1 was the best additive in improving the crude oil yield shear stress and improving the flow properties of crude oil.

## Conflict of Interests

The authors declare that there is no conflict of interests regarding the publication of this paper.

## Acknowledgment

The authors extend their appreciation to the Deanship of Scientific Research at King Saud University for funding this work through Research Group no. RGP-VPP-235.

## References

- [1] A. L. C. Machado and E. F. Lucas, “The influence of vinyl acetate content of the poly(ethylene-co-vinyl acetate) (EVA) additive on the viscosity and the pour point of a Brazilian crude oil,” *Petroleum Science and Technology*, vol. 19, no. 1-2, pp. 197–204, 2001.
- [2] A. L. C. Machado, E. F. Lucas, and G. González, “Poly(ethylene-co-vinyl acetate) (EVA) as wax inhibitor of a Brazilian crude oil: oil viscosity, pour point and phase behavior of organic solutions,” *Journal of Petroleum Science and Engineering*, vol. 32, no. 2-4, pp. 159–165, 2001.
- [3] R. Hoffmann and L. Amundsen, “Influence of wax inhibitor on fluid and deposit properties,” *Journal of Petroleum Science and Engineering*, vol. 107, pp. 12–17, 2013.
- [4] A. E. Erceg Kuzmić, M. Radošević, G. Bogdanić, V. Srića, and R. Vuković, “Studies on the influence of long chain acrylic esters polymers with polar monomers as crude oil flow improver additives,” *Fuel*, vol. 87, no. 13-14, pp. 2943–2950, 2008.
- [5] H. P. Soni, D. P. Bharambe, and A. Nagar, “Synthesis of chemical additives and their effect on Akholjuni crude oil (Gujarat, India),” *Indian Journal of Chemical Technology*, vol. 12, no. 1, pp. 55–61, 2005.
- [6] A. Uhde and G. Kopp, “Pipelines problems resulting from the handling of waxy crude oils,” *Journal of the Institute of Petroleum*, vol. 57, pp. 63–73, 1971.
- [7] R. A. Vora and D. P. Bharambe, “Polymeric flow improvers,” *Indian Journal of Technology*, vol. 31, pp. 633–635, 1993.
- [8] A. J. Son, R. B. Graugnard, B. J. Chai, and A. J. Son, “The effect of structure on performance of maleic anhydride copolymers as flow improvers of paraffinic crude oil,” in *Proceedings of the SPE International Symposium on Oil Field Chemistry*, 25186, pp. 351–362, New Orleans, Lo, USA, 1993.

- [9] B. F. Towler and S. Rebbapragada, "Mitigation of paraffin wax deposition in cretaceous crude oils of Wyoming," *Journal of Petroleum Science and Engineering*, vol. 45, no. 1-2, pp. 11-19, 2004.
- [10] A. Borthakur, N. C. Laskar, R. K. Mazumdar, K. V. Rao, and B. Subrahmanyam, "Synthesis and evaluation of alkyl fumarate-vinyl acetate copolymers in combination with alkyl acrylates as flow improvers for Borholla crude oil," *Journal of Chemical Technology and Biotechnology*, vol. 62, no. 1, pp. 75-80, 1995.
- [11] G. A. Holder and J. Winkler, "Crystal-growth poisoning of n-paraffin wax by polymeric additives and its relevance to polymer crystallization mechanisms," *Nature*, vol. 207, no. 4998, pp. 719-721, 1965.
- [12] S. L. Wang, A. Flammer, and T. Kikabhai, "Select the optimum pour point depressant," *Hydrocarbon Processing*, vol. 78, no. 2, pp. 59-62, 1999.
- [13] D. Chanda, A. Sarmah, A. Borthakur, K. V. Rao, B. Subrahmanyam, and H. C. Das, "Combined effect of asphaltenes and flow improvers on the rheological behaviour of Indian waxy crude oil," *Fuel*, vol. 77, no. 11, pp. 1163-1167, 1998.
- [14] D. M. Duffy and P. M. Rodger, "Hydrogen bonding and the conformations of poly(alkyl acrylamides)," *Journal of the American Chemical Society*, vol. 124, no. 18, pp. 5206-5212, 2002.
- [15] A. G. Didukh, R. B. Koizhaiganova, L. A. Bimendina, and S. E. Kudaibergenov, "Synthesis and characterization of novel hydrophobically modified polybetaines as pour point depressants," *Journal of Applied Polymer Science*, vol. 92, no. 2, pp. 1042-1048, 2004.
- [16] H. H. Abou El-Naga, W. M. Abd El-Azim, and M. M. Ahmed, "Polymeric additives for pour point depression of residual fuel oils," *Journal of Chemical Technology and Biotechnology*, vol. 35, no. 5, pp. 241-247, 1985.
- [17] I. M. El-Gamal, A. M. Atta, and A. M. Al-Sabbagh, "Polymeric structures as cold flow improvers for waxy residual fuel oil," *Fuel*, vol. 76, no. 14-15, pp. 1471-1478, 1997.
- [18] K. S. Pedersen and H. P. Rønningsen, "Influence of wax inhibitors on wax appearance temperature, pour point, and viscosity of waxy crude oils," *Energy & Fuels*, vol. 17, no. 2, pp. 321-328, 2003.
- [19] Y. Song, T. H. Ren, X. S. Fu, and X. H. Xu, "Study on the relationship between the structure and activities of alkyl methacrylate-maleic anhydride polymers as cold flow improvers in diesel fuels," *Fuel Processing Technology*, vol. 86, no. 6, pp. 641-650, 2005.
- [20] W. Ahlers, A. Fechtenkotter, F. O. Mahling, I. Trotsch-Schaller, and A. Eisenbeis, "Fuel oil compositions with improved cold flow properties," US Patent Application 20070094920, 2007.
- [21] R. A. Bloch and D. J. Martella, "Carboxylate-vinyl ester copolymer blend compositions for lubricating oil flow improvement," US. Patent no. 6475963, 2002.
- [22] L. V. Castro and F. Vázquez, "Copolymers as flow improvers for Mexican crude oils," *Energy and Fuels*, vol. 22, no. 6, pp. 4006-4011, 2008.
- [23] H. P. Rønningsen, B. Bjoerndal, A. B. Hansen, and W. B. Pedersen, "Wax precipitation from north sea crude oils. 1. Crystallization and dissolution temperatures, and Newtonian and non-Newton flow properties," *Energy & Fuels*, vol. 5, pp. 895-908, 1991.
- [24] C. X. Da Silva, D. R. S. Álvares, and E. F. Lucas, "New additives for the pour point reduction of petroleum middle distillates," *Energy & Fuels*, vol. 18, no. 3, pp. 599-604, 2004.
- [25] H. P. Soni, K. S. Agrawal, A. Nagar, and D. P. Bharambe, "Designing maleic anhydride- $\alpha$ -olefin copolymeric combs as wax crystal growth nucleators," *Fuel Processing Technology*, vol. 91, no. 9, pp. 997-1004, 2010.
- [26] S. Thamizharasi, P. Gnanasundaram, and S. Balasubramanian, "Copolymers of 4-nitrophenyl methacrylate with styrene: synthesis, characterization, and reactivity ratios," *Journal of Applied Polymer Science*, vol. 74, no. 5, pp. 1186-1193, 1999.
- [27] A. M. Atta, A. M. Elsayed, and H. I. Shafy, "Uses of electron-beam irradiation to prepare pH- And temperature-sensitive hydrogels from reactive poly(vinyl alcohol) grafts," *Journal of Applied Polymer Science*, vol. 108, no. 3, pp. 1706-1715, 2008.
- [28] A. M. Atta, M. A. Elsockary, O. F. Kandil, and Z. M. Mohamed, "Using of modified plastic waste based on poly(ethylene-co-acrylic acid) grafts to solve transportation problem of petroleum crude oil," *Journal of Dispersion Science and Technology*, vol. 29, no. 1, pp. 7-19, 2008.
- [29] B. Wesslen and K. B. Wesslen, "Preparation and properties of some water-soluble, comb-shaped, amphiphilic polymers," *Journal of Polymer Science, Part A: Polymer Chemistry*, vol. 27, no. 12, pp. 3915-3926, 1989.
- [30] S. Deshmukh and D. P. Bharambe, "Synthesis of polymeric pour point depressants for Nada crude oil (Gujarat, India) and its impact on oil rheology," *Fuel Processing Technology*, vol. 89, no. 3, pp. 227-233, 2008.
- [31] H. S. Ashbaugh, L. J. Fetters, D. H. Adamson, and R. K. Prud'homme, "Flow improvement of waxy oils mediated by self-aggregating partially crystallizable diblock copolymers," *Journal of Rheology*, vol. 46, no. 4, pp. 763-776, 2002.
- [32] J. Au, "Optimize pour point control to save money," *Hydrocarbon Processing*, vol. 80, no. 1, pp. 73-75, 2001.
- [33] A. Borthakur, N. C. Laskar, R. K. Mazumdar, K. V. Rao, and B. Subrahmanyam, "Synthesis and evaluation of alkyl fumarate-vinyl acetate copolymers in combination with alkyl acrylates as flow improvers for Borholla crude oil," *Journal of Chemical Technology and Biotechnology*, vol. 62, pp. 75-80, 1995.
- [34] G. A. Holder and J. Winkler, "Wax crystallization from distillate fuels, part I. Cloud and pour phenomena exhibited by solutions of binary N-paraffin mixtures," *J. Inst. Pet.*, vol. 51, pp. 228-232, 1965.
- [35] S. E. Kudaibergenov, A. G. Didukh, Z. E. Ibraeva et al., "A regular, hydrophobically modified polyampholyte as novel pour point depressant," *Journal of Applied Polymer Science*, vol. 98, no. 5, pp. 2101-2108, 2005.
- [36] H. Li and J. Zhang, "A generalized model for predicting non-Newtonian viscosity of waxy crudes as a function of temperature and precipitated wax," *Fuel*, vol. 82, no. 11, pp. 1387-1397, 2003.
- [37] J. W. Qian, G. R. Qi, X. Z. Ding, and S. L. Yang, "Assessment of polymer flow improvers for crude oil by viscometry," *Fuel*, vol. 75, no. 3, pp. 307-312, 1996.
- [38] H. P. Rønningsen, "Rheological behaviour of gelled, waxy North Sea crude oils," *Journal of Petroleum Science and Engineering*, vol. 7, no. 3-4, pp. 177-213, 1992.

## Research Article

# Comparative Study on Particles Formation in a Diesel Engine When Lubricating Oil Involved in Fuel Combustion

Lihui Dong,<sup>1</sup> Weiqiang Han,<sup>2</sup> Xingyu Liang,<sup>3</sup> and Yuesen Wang<sup>3</sup>

<sup>1</sup>School of Aeronautical Engineering, Civil Aviation University of China, Tianjin 300300, China

<sup>2</sup>Laboratory of IC Engine, Xihua University, Chengdu 610039, China

<sup>3</sup>State Key Laboratory of Engines, Tianjin University, No. 92 Weijin Road, Nankai District, Tianjin 300072, China

Correspondence should be addressed to Xingyu Liang; [tjulxy@163.com](mailto:tjulxy@163.com)

Received 18 January 2015; Accepted 23 February 2015

Academic Editor: Ming Huo

Copyright © 2015 Lihui Dong et al. This is an open access article distributed under the Creative Commons Attribution License, which permits unrestricted use, distribution, and reproduction in any medium, provided the original work is properly cited.

The effect of lubricating oil on the morphology of particulate matter (PM) was studied in a diesel engine fueled with pure diesel fuel and blended fuel containing 0.5% by weight of lubricating oil. Particulate matter emitted by diesel engines is formed primarily by soot agglomerates which are composed of primary particles. In this paper, particulate matter was collected with a thermophoretic sampling system, and a high-resolution transmission electron microscope (TEM) was used to investigate the primary particles. A Fast Particulate Spectrometer, DMS 500, was used to determine the particle size distributions. The TEM results indicated that the mean diameters of the primary particles increased after the oil was added into the fuel. Particle size distributions results showed that lubricating oil in the fuel gave rise to a higher concentration in nucleation mode.

## 1. Introduction

Although diesel engines are widely used in on-road transport because of their efficiency and reliability, particulate matter (PM) emitted from diesel engines has negative impacts on human health [1, 2]. The total mass of PM emissions from diesel engines has been significantly reduced with the advent of stricter emission standards. However, the current emission standards impose limitations only on the mass of particulate matter that is larger than  $2.5\ \mu\text{m}$  (PM 2.5). Although smaller particulates contribute little to the total mass, their significant number and effect on human health and the environment have drawn people's attention. This is also the reason why particulate matter smaller than  $2.5\ \mu\text{m}$  is proposed to be included in future emission limits. To achieve lower PM emissions, regardless of total mass or number, the optimization of combustion and the use of a posttreatment system could be effective ways to deal with this issue. Detailed characteristics of PM are indispensable to achieve the desired improvement.

A commercial mobility sizer and high-resolution transmission electron microscope (TEM) are widely used in

investigating the detailed characteristics of PM. Although the use of a mobility sizer is always considered to be a controversial way to determine PM characteristics, its high speed and stability are indisputable, especially in comparing PM emissions; thus it is widely used in PM investigations [3–7]. The results from the mobility sizer were also verified to be consistent in tendency with that from TEM investigations [8].

Of course, results from TEM images are more direct and visual. Coupled with a thermophoretic sampling system, many detailed characteristics of PM, such as the primary particle diameters, morphology, and gyration diameters and others, can be achieved [9–13]. These results are of great importance in understanding the formation of particulate matter and in guiding the optimization of combustion to achieve lower PM emissions. However, the choice of samples and the conversion from pixels to actual dimensions can lead to tiny errors.

Many factors will influence the formation of PM and lubricating oil is an important one [14–23]. During engine operation, lubricating oil consumption is inevitable and this is the reason why PM emissions were found in a hydrogen-powered engine [24].

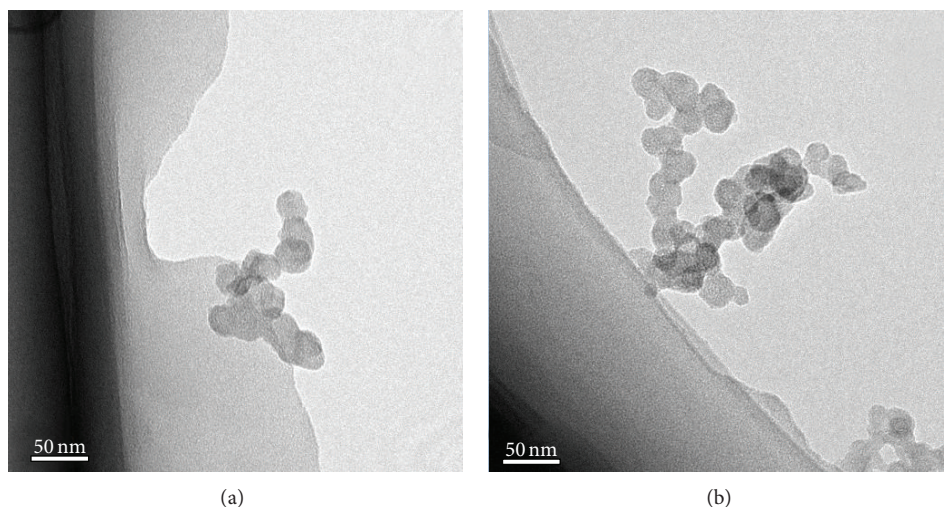


FIGURE 1: TEM photographs of diesel particulates sampled at (a) 2000 rpm/25% load when fueled with pure diesel and (b) 2000 rpm/75% load when fueled with blended fuel containing oil.

The contribution of lubricating oil to PM formation is focused primarily on soluble organic fraction (SOF) [25] and soot [26]. Lubricating oil shows great influence on SOF formation and this can be explained through its means of consumption. The means by which lubricating oil is consumed has been investigated in detail [27]. Such investigations have concluded that cylinder liner evaporation substantially affects total engine oil consumption.

It is easy for the oil evaporated from the cylinder liner to condense on the soot surface and contribute to SOF formation. Part of the oil entering the combustion chamber is not burnt and will contribute to the SOF formation in the same way.

When considering the contributors to oil consumption, part of the oil which enters the combustion chamber will be involved with the fuel combustion because of the complex airflow motion in the chamber. It is easy to imagine that combustion of fuel will be influenced to a minor extent because of lubricating oil droplets cracking, evaporating, or combusting. Oil droplets will absorb heat from their surroundings when they crack or evaporate, and the resultant lower temperature will favor PM formation. Previous studies have also indicated that use of lubricating oil will lead to the change of particle size distributions and total number of concentrations [28].

The main purpose of this paper is to investigate the influence of lubricating oil combustion on soot formation in a diesel engine. Because of the low rate of oil consumption during normal engine operation, it is difficult to achieve repetitive and reliable results. Although oil consumption will rise when engine speed and load increases [27], yet different operating conditions will influence PM formation. In this paper, 0.5% oil in weight is blended into the diesel fuel. This does not conform to normal operating conditions but does make sense in investigating the influence of oil combustion on PM formation. Particulate matter was collected with a thermophoretic sampling system, and a high-resolution transmission electron microscope (TEM) was

used to investigate the primary particles. A Fast Particulate Spectrometer, DMS 500, was used to determine the particle size distributions. The results can well illustrate the influence of lubricating oil combustion on PM formation.

## 2. Experimental Setup

The experiments were performed on a direct-injection four-stroke diesel engine (Yunnei 4100QB) with a peak torque of 340 Nm at 2000 rpm. The compression ratio of each cylinder is 17.8 to 1 and the displacement volume is 3.612 L. The engine speed in this paper was 2000 rpm and the load was 25% and 75% of full load. The test fuel is pure diesel fuel and blended fuel containing 0.5% by weight of lubricating oil (Mobil API CI-4 15W40). The oil blended into the diesel fuel was the same as that in the oil pan.

Before the test, the engine and the DMS500 were warmed up for half an hour. A widely used thermophoretic sampling system was employed to collect the particulate matter. Copper grids were used during the sampling. After each sampling, the grid was carefully removed and stored in the sample box until the TEM observation. A JEM-2010FEF transmission electron microscope with a resolution of 0.23 nm was used to observe particles. Magnifications above 42,500x were used for spherule diameter measurements.

After each sampling, the engine was kept operating. The valve leading to the DMS500 was opened. The pipe connecting the DMS500 to the exhaust pipe was at almost the same position where particles were sampled for TEM observation. The DMS500 would adjust the dilution ratio automatically, and the data would be steady after about 10 seconds. After about 30 seconds, when the data was steady, the experimental results were recorded for 15 seconds.

## 3. Results and Discussions

Figures 1(a) and 1(b) show the typical TEM images of diesel particulates sampled at 2000 rpm/25% load when fueled with

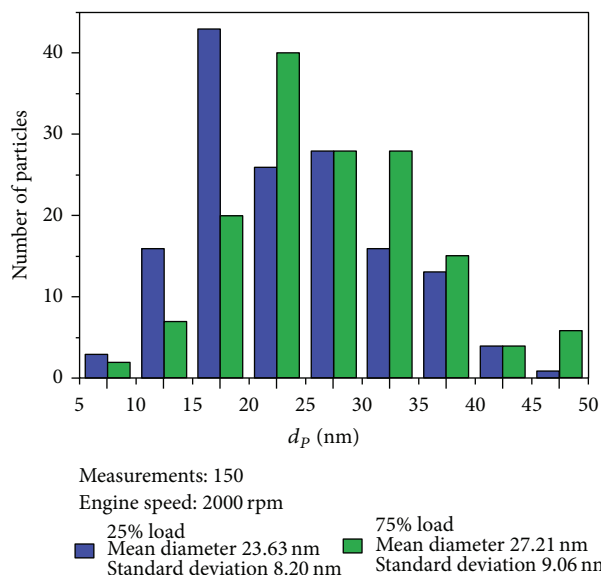


FIGURE 2: Primary particle diameter distribution when fueled with pure diesel.

pure diesel and at 2000 rpm/75% load when fueled with blended fuel containing oil, respectively.

It can be seen from Figure 1 that the appearance of particulates is almost identical to those in other studies; that is, particulates have different shapes with grapelike structures and many spherical primary particles collect to form clusters.

**3.1. Primary Particle Size Distributions.** 20 images were taken of each operating condition and 7 or 8 primary particles with clear boundaries were selected for measurement. Mean diameters of primary particles are obtained by averaging the diameters of 150 primary particles. From the resulting primary diameters, size distributions were obtained for each operating condition as shown in Figures 2 and 3.

Clear conclusions can be made that the distributions were statistically normal before and after the oil is added into diesel fuel. It is statistically acceptable to choose 150 primary particles. In fact, 50 primary particles can well reflect the distributions of particles [9].

The influences of lubricating oil on the primary particle formations are listed below by analyzing the results shown in Figures 2 and 3.

First, the mean primary particle diameters are about 23 nm, 27 nm, 27 nm, and 28 nm under four different conditions as shown in Figures 2 and 3. Uncertainties will definitely exist during the diameter measuring but errors should be within 1 nm. Results in this paper are well in accordance with past results [29, 30]. Although different engines were used in these experiments, the mean diameters of primary particles were in the range of 19 nm to 35 nm. The results indicated that engine types or operating conditions may show little influence on primary particle formation and that the PM emissions should be influenced significantly by soot oxidation.

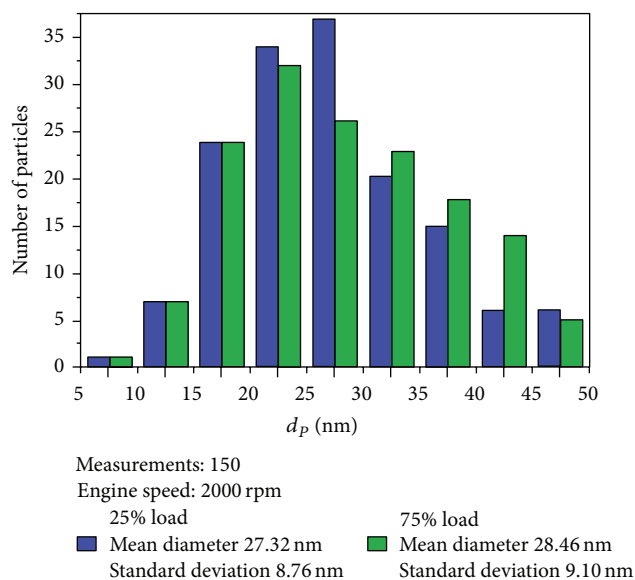


FIGURE 3: Primary particle diameter distribution when fueled with blended fuel containing oil.

However, although primary particle diameter distributions were typically normal ones, problems still exist when judging the primary particle diameters. Figure 4 shows the typical TEM images of diesel particulates sampled at 2000 rpm/25% load when fueled with pure diesel.

Primary particle diameters in the four parts of Figure 4 are quite different: 15~20 nm, 25~30 nm, 35~40 nm, and 10~30 nm, respectively. This phenomenon indicates that combustion in the chamber is not homogeneous. Meanwhile, diameters of primary particles in one cluster tended to be the same, which means that primary particles may agglomerate immediately after they are formed.

During the actual sampling and testing, the diameter of the copper grid is about 3 mm, and the range of TEM observation is an extremely small part of the grid. Choice of cluster photographs may be another factor that causes errors.

Second, the mean diameters of primary particles decrease when the load increases. This can be explained by the situation whereby as combustion temperature and exhaust temperature increase with an increased load, particles are oxidized more completely. However, high load requires more fuel to be injected into the combustion chamber and then incomplete combustion will lead to the growth of particle formation. Other investigations have also explained the conflicting process of particle formation [11, 31]. In this paper, the oxidation rates of particles exceeded the surface growth rates so that primary particles decreased with the load increasing.

Third, mean diameters of primary particle increase from 23.63 nm to 27.21 nm at a speed of 2000 rpm/25% and from 27.32 nm to 28.46 nm at a speed of 2000 rpm/75% load. The results indicate that mean diameters increase after the oil is added into the diesel fuel and the effect is more pronounced when the load is lower. It can be explained that particles will form when the oil is burnt. Since the lubricating oil

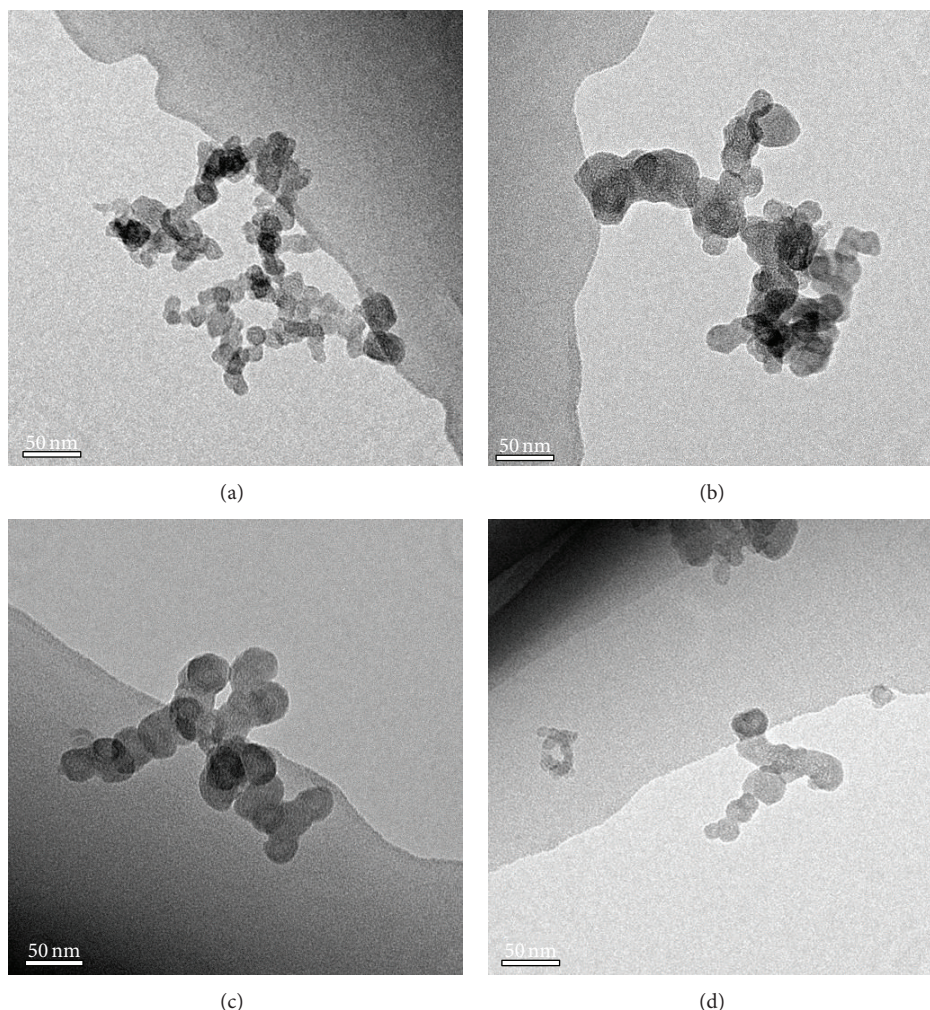


FIGURE 4: TEM photographs of diesel particulates sampled at 2000 rpm/25% load when fueled with pure diesel.

is composed primarily of macromolecules, the particles are bigger than those formed during the combustion of diesel fuel at low load. Combustion temperature will rise when the load is higher and the contribution is diminished. During the actual engine operation, combustion of lubricating oil should contribute little to the total PM emissions because of the low oil consumption. Another factor is the influence of lubricating oil droplets on particle formation during the combustion of diesel fuel. In a small range surrounding the lubricating oil droplets, combustion temperature will change because of the different physical and chemical characteristics of lubricating oil. In addition, additives in the oil may also influence the formation or oxidation of particles. When the load is high, more oil is injected into the combustion chamber and more particles form and then the influence of lubricating oil is not that obvious.

**3.2. Particle Size Distributions.** Particle size distributions at different operating conditions are shown in Figures 5 and 6.

The mean diameter of the agglomerated particles (accumulation mode) is in the range of 50–100 nm.

Particle size distributions changed significantly after the oil is blended into diesel fuel. The most obvious change is in the nucleation mode. When fueled with pure diesel, there are two peaks in nucleation mode and the peak increases rapidly after the oil is blended, regardless of low load or high load. Peaks in accumulation mode changed little after the oil is blended. A conclusion can also be made that oil exerts less influence on the particle size distributions at higher load.

Figure 7 shows the total number concentrations under different conditions. It can be seen here that the total number concentrations increase after the oil is blended into diesel fuel. The influence of lubricating oil on PM emissions is significant when the load is low. Oil shows little influence on total number concentration when the load is high and these results agree well with that of primary particle diameters. However, the total number concentrations are almost the same when the oil is added into diesel fuel. It can be explained that the oil has great influence on the characteristic of particles and

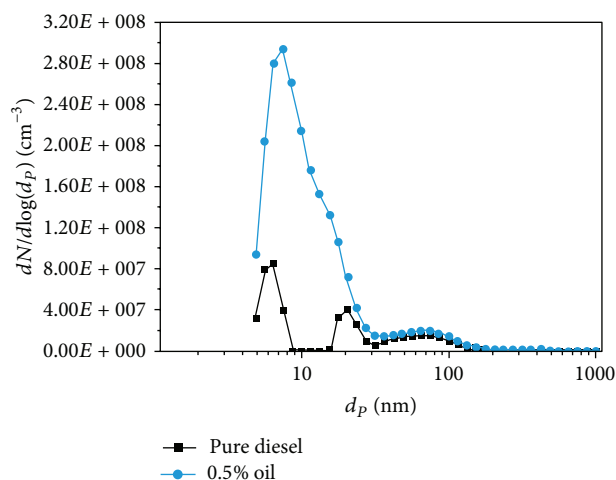


FIGURE 5: Particle size distributions at the speed of 2000 rpm/25% load.

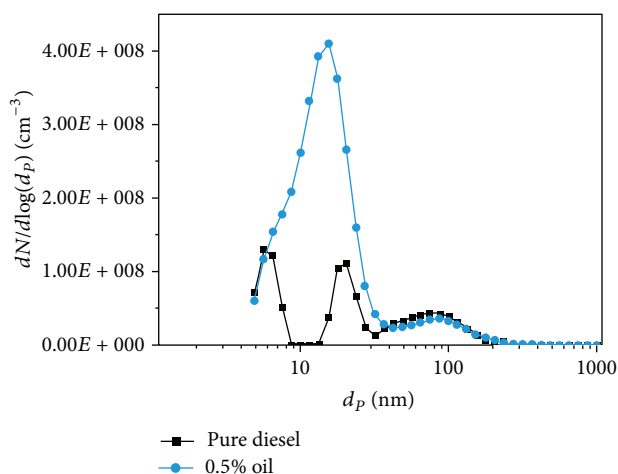


FIGURE 6: Particle size distributions at the speed of 2000 rpm/75% load.

TABLE 1: Particles formation comparison.

Load		25%	75%
Pure diesel	Primary particle diameter	23.63 nm	27.21 nm
	Total number concentrations	$4.32e^7$	$1.21e^8$
Diesel blended with oil	Primary particle diameter	27.32 nm	28.46 nm
	Total number concentrations	$1.91e^8$	$1.81e^8$

this leads to the change of the spectrum identification of the DMS500.

Table 1 shows the comparison of particles formation.

## 4. Conclusions

- (1) Lubricating oil involved in fuel combustion will lead to an increase in primary particle diameters and the influence is obvious when the load is low.
- (2) Particle size distribution results also indicate that the influence of lubricating oil on PM emissions is less obvious when the load is high.
- (3) Results from the mobility sizer and TEM observation show the approximate tendency in comparing the PM emissions. Microstructures of particles will change after oil is involved in combustion.

## Conflict of Interests

The authors declare that there is no conflict of interests regarding the publication of this paper.

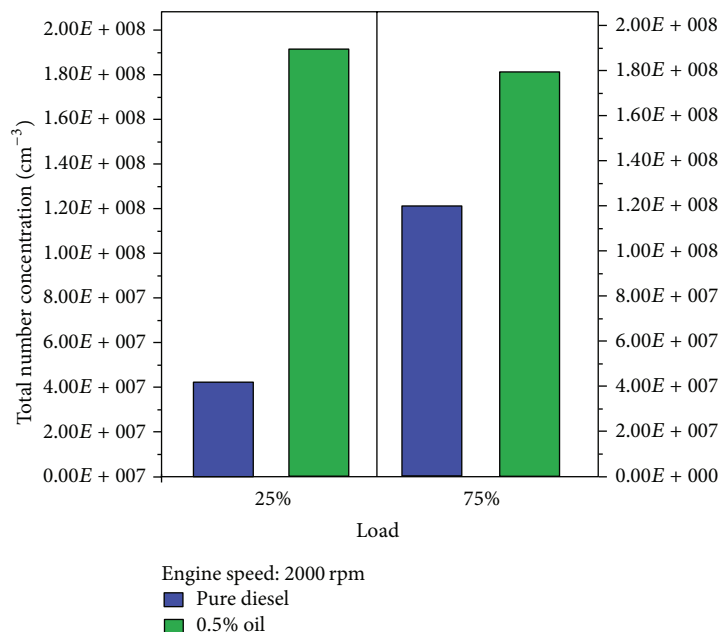


FIGURE 7: Total number concentrations under different conditions.

## Acknowledgments

Authors wish to express their sincere appreciation to the financial support of the NSFC (51376136) and NSFC (51406132).

## References

- [1] A. D. Kappos, P. Bruckmann, T. Eikmann et al., "Health effects of particles in ambient air," *International Journal of Hygiene and Environmental Health*, vol. 207, no. 4, pp. 399–407, 2004.
- [2] D. B. Warheit, C. M. Sayes, K. L. Reed, and K. A. Swain, "Health effects related to nanoparticle exposures: environmental, health and safety considerations for assessing hazards and risks," *Pharmacology and Therapeutics*, vol. 120, no. 1, pp. 35–42, 2008.
- [3] H. Kim and B. Choi, "Effect of ethanol–diesel blend fuels on emission and particle size distribution in a common-rail direct injection diesel engine with warm-up catalytic converter," *Renewable Energy*, vol. 33, no. 10, pp. 2222–2228, 2008.
- [4] B. Bougie, L. C. Ganippa, A. P. van Vliet, W. L. Meerts, N. J. Dam, and J. J. T. Meulen, "Soot particulate size characterization in a heavy-duty diesel engine for different engine loads by laser-induced incandescence," *Proceedings of the Combustion Institute*, vol. 31, pp. 685–691, 2007.
- [5] T. Gupta, A. Kothari, D. K. Srivastava, and A. K. Agarwal, "Measurement of number and size distribution of particles emitted from a mid-sized transportation multipoint port fuel injection gasoline engine," *Fuel*, vol. 89, no. 9, pp. 2230–2233, 2010.
- [6] C. Wang, H. Xu, J. M. Herreros, and J. Wang, "Impact of fuel and injection system on particle emissions from a GDI engine," *Applied Energy*, vol. 132, pp. 178–191, 2014.
- [7] P.-Q. Tan, S.-S. Ruan, Z.-Y. Hu, D.-M. Lou, and H. Li, "Particle number emissions from a light-duty diesel engine with biodiesel fuels under transient-state operating conditions," *Applied Energy*, vol. 113, pp. 22–31, 2014.
- [8] M. F. Chandler, Y. Teng, and U. O. Koylu, "Diesel engine particulate emissions: a comparison of mobility and microscopy size measurements," *Proceedings of the Combustion Institute*, vol. 31, pp. 2971–2979, 2007.
- [9] M. Lapuerta, F. J. Martos, and J. M. Herreros, "Effect of engine operating conditions on the size of primary particles composing diesel soot agglomerates," *Journal of Aerosol Science*, vol. 38, no. 4, pp. 455–466, 2007.
- [10] A. Neer and U. O. Koylu, "Effect of operating conditions on the size, morphology, and concentration of submicrometer particulates emitted from a diesel engine," *Combustion and Flame*, vol. 146, no. 1-2, pp. 142–154, 2006.
- [11] J. Zhu, K. O. Lee, A. Yozgatligil, and M. Y. Choi, "Effects of engine operating conditions on morphology, microstructure, and fractal geometry of light-duty diesel engine particulates," *Proceedings of the Combustion Institute*, vol. 30, pp. 2781–2789, 2005.
- [12] K. Tian, K. A. Thomson, F. Liu, D. R. Snelling, G. J. Smallwood, and D. Wang, "Determination of the morphology of soot aggregates using the relative optical density method for the analysis of TEM images," *Combustion and Flame*, vol. 144, no. 4, pp. 782–791, 2006.
- [13] Y. Wei, K. Wang, W. Wang et al., "Comparison study on the emission characteristics of diesel- and dimethyl ether-originated particulate matters," *Applied Energy*, vol. 130, pp. 357–369, 2014.
- [14] M. T. Spencer, L. G. Shields, D. A. Sodeman, S. M. Toner, and K. A. Prather, "Comparison of oil and fuel particle chemical signatures with particle emissions from heavy and light duty vehicles," *Atmospheric Environment*, vol. 40, no. 27, pp. 5224–5235, 2006.

- [15] J. Cromas and J. B. Ghandhi, "Lubricating oil contribution to direct-injection two stroke engine particulate emissions," SAE Technical Paper 2004-32-0012, 2004.
- [16] J. Czerwinski, J. L. Pétermann, A. Ulrich, G. Mueller, and A. Wichser, "Particle emissions of a TDI-engine with different lubrication oils," SAE Paper 2005-01-1100, 2005.
- [17] B. A. Buchholz, R. W. Dibble, D. Rich, and A. S. Cheng, "Quantifying the contribution of lubrication oil carbon to particulate emissions from a diesel engine," SAE Paper 2003-01-1987, SAE International, 2003.
- [18] H. Jung, D. B. Kittelson, and M. R. Zachariah, "The influence of engine lubricating oil on diesel nanoparticle emissions and kinetics of oxidation," SAE Paper 2003-01-3179, 2003.
- [19] R. Gligorijevic, J. Jevtic, and D. J. Borak, "Engine oil contribution to diesel exhaust emissions," *Journal of Synthetic Lubrication*, vol. 23, no. 1, pp. 27–38, 2006.
- [20] K. Froelund, E. C. Owens, E. Frame et al., "Impact of lubricant oil on regulated emissions of a light-duty Mercedes-Benz OM611 CIDI-engine," SAE Paper 2001-01-1901, 2001.
- [21] P. C. C. de Albuquerque, R. N. de Andrade Ávila, P. H. Barros Zárante, and J. R. Sodré, "Lubricating oil influence on exhaust hydrocarbon emissions from a gasoline fueled engine," *Tribology International*, vol. 44, no. 12, pp. 1796–1799, 2011.
- [22] K. M. Jefferd, J. S. Rogerson, D. E. Copp, R. L. Brundle, and M. A. Huntly, "The impact of lubricants on heavy duty diesel engine fuel economy and exhaust emissions," SAE Paper 2000-01-1983, 2000.
- [23] G. W. R. Taylor, "The effect of lubricating oil volatility on diesel emissions," SAE Paper 2001-01-1261, 2001.
- [24] A. L. Miller, C. B. Stipe, M. C. Habjan, and G. G. Ahlstrand, "Role of lubrication oil in particulate emissions from a hydrogen-powered internal combustion engine," *Environmental Science and Technology*, vol. 41, no. 19, pp. 6828–6835, 2007.
- [25] S. Brandenberger, M. Mohr, K. Grob, and H. P. Neukom, "Contribution of unburned lubricating oil and diesel fuel to particulate emission from passenger cars," *Atmospheric Environment*, vol. 39, no. 37, pp. 6985–6994, 2005.
- [26] M. S. P. Kahandawala, J. L. Graham, and S. S. Sidhu, "Impact of lubricating oil on particulates formed during combustion of diesel fuel—a shock tube study," *Fuel*, vol. 83, no. 13, pp. 1829–1835, 2004.
- [27] E. Yilmaz, T. Tian, V. W. Wong, and J. B. Heywood, "The contribution of different oil consumption sources to total oil consumption in a spark ignition engine," SAE Paper 2004-01-2909, 2004.
- [28] L. Dong, G. Shu, and X. Liang, "Effect of lubricating oil on the particle size distribution and total number concentration in a diesel engine," *Fuel Processing Technology*, vol. 109, pp. 78–83, 2013.
- [29] M. Wentzel, H. Gorzawski, K.-H. Naumann, H. Saathoff, and S. Weinbruch, "Transmission electron microscopical and aerosol dynamical characterization of soot aerosols," *Journal of Aerosol Science*, vol. 34, no. 10, pp. 1347–1370, 2003.
- [30] K. Park, D. B. Kittelson, and P. H. McMurry, "Structural properties of diesel exhaust particles measured by Transmission Electron Microscopy (TEM): relationships to particle mass and mobility," *Aerosol Science and Technology*, vol. 38, no. 9, pp. 881–889, 2004.
- [31] K. O. Lee, R. Cole, R. Sekar et al., "Detailed characterization of morphology and dimensions of diesel particulates via thermophoretic sampling," SAE Technical Paper 2001-01-3572, 2001.

## Research Article

# Experimental Investigation of Injection Strategies on Low Temperature Combustion Fuelled with Gasoline in a Compression Ignition Engine

Binbin Yang,<sup>1,2</sup> Mingfa Yao,<sup>2</sup> Zunqing Zheng,<sup>2</sup> and Lang Yue<sup>2</sup>

<sup>1</sup>School of Transportation and Vehicle Engineering, Shandong University of Technology, Zibo 255049, China

<sup>2</sup>State Key Laboratory of Engines, Tianjin University, Tianjin 300072, China

Correspondence should be addressed to Mingfa Yao; y\_mingfa@tju.edu.cn

Received 9 January 2015; Accepted 3 March 2015

Academic Editor: Ming Huo

Copyright © 2015 Binbin Yang et al. This is an open access article distributed under the Creative Commons Attribution License, which permits unrestricted use, distribution, and reproduction in any medium, provided the original work is properly cited.

The present study focuses on the experimental investigation on the effect of fuel injection strategies on LTC with gasoline on a single-cylinder CI engine. Firstly, the engine performance and emissions have been explored by sweeping SOI and split percentage for the load of 0.9 MPa IMEP at an engine speed of 1500 rpm. Then, the double-injection strategy has been tested for load expansion compared with single-injection. The results indicate that, with the fixed CA50, the peak HRR is reduced by advancing SOI and increasing split percentage gradually. Higher indicated thermal efficiency, as well as lower MPRR and COV, can be achieved simultaneously with later SOI and higher split percentage. As split percentage increases, NO<sub>x</sub> emission decreases but soot emission increases. CO and THC emissions are increased by earlier SOI, resulting in a slight decrease in combustion efficiency. Compared with single-injection, the double-injection strategy enables successful expansion of high-efficiency and clean combustion region, with increasing soot, CO, and THC emissions at high loads and slightly declining combustion efficiency and indicated thermal efficiency, however. MPRR and soot emission are considered to be the predominant constraints to the load expansion of gasoline LTC, and they are related to their trade-off relationship.

## 1. Introduction

With great concerns about engine emitted pollutant and global warming issues, alternative combustion concepts are drawing increasing attention worldwide. The concepts applied to compression ignition (CI) engines mainly consist of homogeneous charge compression ignition (HCCI) [1], premixed charge compression ignition (PCCI) [2], low temperature combustion (LTC) [3], and so forth. They all share the feature of achieving lower temperature combustion together with a lean mixture distribution by allowing extra time from end of the injection to start of the combustion (SOC), thereby yielding the simultaneous ultra-low nitrogen oxides (NO<sub>x</sub>) and particle matter (PM) emissions, which are greatly challenged in conventional CI engines. Therefore, all these combustion concepts can be labeled under the term of LTC.

LTC concept is generally characterized by long ignition delay, high exhaust gas recirculation (EGR) rate, and

premixed charge. With the further research, except the dominating role of chemical kinetics in LTC already been recognized, the importance of fuel and air mixing process has also been realized. However, as the conventional fuel in CI engines, diesel fuel has cetane number (CN) higher than 40 and poor volatility, which makes its ideal mixing with air before the onset of combustion unachievable at high engine loads even by the combination of a variety of technical means, for example, high pressure injection, cooled EGR, and decreased compression ratio [4]. As a result, the operation range of high-efficiency and clean LTC with diesel is still limited within low and medium loads.

Recently, the fuel properties of LTC have gained great scientific concerns, mainly because fuel properties control the time scales of both chemical kinetics and fuel-air mixing. Thus, it is suggested that a less reactive fuel is preferred for combustion control at high engine loads. In the former studies, mixture of gasoline and diesel termed as dieseline

by Turner et al. [5] is demonstrated as a promising fuel for simultaneous reduction of  $\text{NO}_x$  and soot emissions at a lower EGR level, owing to the improved premixture by the better volatility and lower CN. The relevant works have been conducted extensively during the past decade [5, 6], but it is challenging to further increase the engine load. Based on the deep insight into fuel properties of LTC, Johansson et al. proposed to inject gasoline directly into cylinder by common-rail system, which is referred to as partially premixed combustion (PPC) concept [7]. Under PPC conditions, autoignition can be made to occur after the fuel and air are well mixed, and soot emission can be reduced. The successful operation of PPC concept with gasoline has been estimated to reach 49-50% brake efficiency between 1.5 and 2.6 MPa gross indicated mean effective pressure (IMEP) while keeping low emissions [8]. Meanwhile, mixture concentration distribution can be well controlled by adjusting injection strategies, which is favorable for combustion phasing and burning rate control. Furthermore, the high-octane fuel PPC has the ability of reducing the heavy reliance on the EGR usage in diesel LTC, avoiding the consequent fuel economy penalty.

Nevertheless, a full separation between end of the injection and SOC results in unacceptable pressure oscillation which enhances heat transfer and leads to increased specific fuel consumption. Thus, the high pressure rise rate is a great concern for such premixed combustion. In an effort to solve the maximum pressure rise rate (MPRR) issue while maintaining stable combustion, low-octane gasoline has been used to avoid the overmixing of fuel and air [9]. The issue might also be alleviated via applying advanced injection strategies, for example, the double-injection strategy proposed by Kalghatgi et al. [10]. The research identifies that gasoline split injection early in the compression stroke helps reduce MPRR for a given load and enables heat release to occur later with low cyclic variation as compared with single-injection strategy. Because of that, higher IMEP can be reached with lower smoke and  $\text{NO}_x$ ; for example, one of the operating points has mean IMEP of 1.595 MPa, as well as AVL smoke opacity of 0.33% and  $\text{NO}_x$  of 0.58 g/kWh. The research group from Wisconsin University has conducted some relevant works of comparing the single- and double-injection strategy at A50 (1300 rpm @ 1.3 MPa IMEP) condition [11]. Interestingly, the double-injection strategy produces higher MPRR and  $\text{NO}_x$  emission as compared to single-injection strategy, which demonstrates the engine performance and emissions are strongly influenced by injection parameters in multi-injection strategy. Ciatti and Subramanian from Argonne National Laboratory have proposed three injection strategies to struggle for meeting the current emission legislation [12]. For the medium and high loads, the partially premixed charge is obtained through an earlier injection and the rest of the fuel is injected around top dead center. As load increases, the first injection has to be well advanced to prepare sufficient premixing charge. The significance of mixture stratification resulting from the overlap of fuel spray and followed combustion in controlling combustion rate has been recognized by Yang et al. [13].

Based on the analysis of the existing problems, the authors intend to explore the effect of fuelling strategies on LTC with

TABLE 1: Engine and injector specifications.

Bore (mm)	105
Stroke (mm)	125
Connecting rod length (mm)	210
Squish height (mm)	0.85
Displacement (L)	1.08
Compression ratio	16 : 1
Swirl ratio	1.5
I VO ( $^{\circ}$ CA ATDC)	-377
I VC ( $^{\circ}$ CA ATDC)	-133
EVO ( $^{\circ}$ CA ATDC)	125
EVC ( $^{\circ}$ CA ATDC)	-342

93 research octane number (RON) gasoline. The study is driven in two steps. Firstly, a sweeping of start of the first injection (SOI1) and split percentage is experimented in detail to investigate the effect of these two factors on combustion and emission characteristics, as well as to seek for the key limiting factors of operation range expansion. Secondly, the double-injection strategy is tested at high load condition for load expansion, with a baseline experiment with single-injection. Therefore, the current research will be served as a theoretical evidence for the operation range expansion of high-efficiency and clean combustion in CI engines.

## 2. Experimental Apparatus

**2.1. Engine.** The experiments were all performed on a modified six-cylinder CI engine. The test cylinder with a displacement of 1.08 L was separated from other cylinders to avoid multicylinder interference and was equipped with independently adjustable intake/exhaust, exhaust gas recirculation (EGR), and common-rail injection system while other engine components remain intact. The engine specifications are listed in Table 1. The compression ratio was reduced from original 17.5 to 16 for prolonging ignition delay. Fresh air was externally compressed by an auxiliary compressor to simulate the boosted condition, whose pressure was adjusted by a by-pass valve close to the compressor outlet. Both the EGR valve and the back pressure valve were applied to control the amount of exhaust gas flow into the intake pipe and consequently the EGR rate. The schematic diagram of the engine setup is illustrated in Figure 1.

**2.2. Instrumentation.** In-cylinder pressure was measured with a pressure transducer (Kistler 6125A) in conjunction with a charge amplifier (Kistler 5011). The shaft encoder (Kistler 2614A4) had a resolution of  $0.5^{\circ}$  crank angle (CA). Combustion parameters discussed in this paper were calculated from averages of 100 consecutive cycles of cylinder pressure data. Both heat release rate (HRR) and MPRR were calculated by a combustion analysis software package from the averaged cylinder pressure.

The test cylinder was equipped with a second generation prototype common-rail system from Bosch, which is the same as the one on the original engine. The nozzle had an

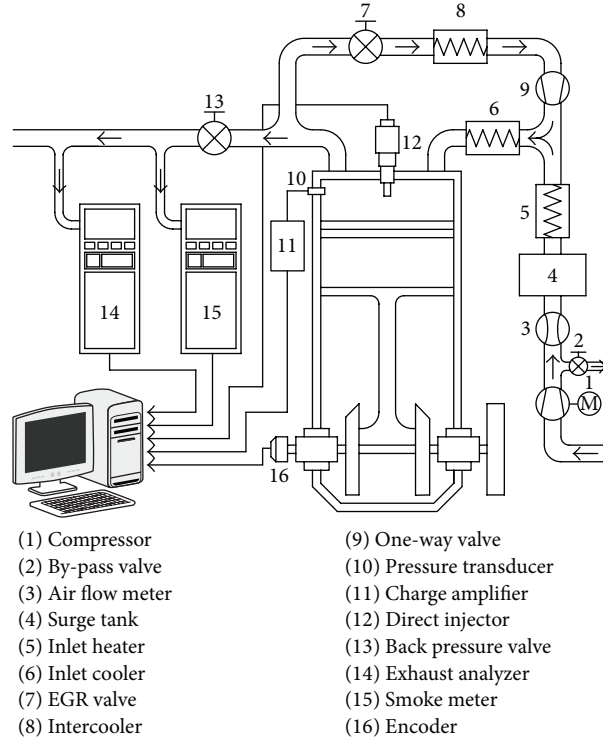


FIGURE 1: Schematic of experimental setup.

umbrella angle of  $150^\circ$  and 8 orifices, whose diameter was 0.15 mm. The ECU for controlling the direct injection system was coordinated by software on a PC. The arrangement enabled flexible settings of common-rail pressure, injection timing, injection quantity, and multi-injection strategies. The fuel flow rate was measured by a fuel consumption meter (AVL 733S) with a gravity scale, and each operating point was sampled for at least 3 minutes.

The concentrations of gaseous emissions, for example,  $\text{NO}_x$ , total hydrocarbon (THC), carbon monoxide (CO), and carbon dioxide ( $\text{CO}_2$ ), were measured using an exhaust analyzer (Horiba MEXA-7100DEGR), which measures  $\text{NO}_x$  by the chemiluminescent method, THC by the flame ionization method, and CO and  $\text{CO}_2$  by the nondispersive infrared method. The EGR rate was determined via calculating the ratio of intake  $\text{CO}_2$  to exhaust  $\text{CO}_2$  concentration, as shown in (1). Consider

$$\text{EGR} = \frac{[\text{CO}_2]_{\text{intake}}}{[\text{CO}_2]_{\text{exhaust}}} \cdot 100\%. \quad (1)$$

A filter smoke meter (AVL 415S) was utilized to measure soot levels in terms of filter smoke number (FSN) and changed into mass by the empirical formula provided by the instrument manual as follows:

$$\text{soot} = \frac{5.32}{0.405} \times \text{FSN} \times e^{0.3062 \times \text{FSN}} \times 0.001 \times \frac{(m_{\text{air}} + m_{\text{fuel}})}{1.2929}, \quad (2)$$

where  $m_{\text{air}}$  and  $m_{\text{fuel}}$  are the intake air flow and fuel consumption rate, respectively, kg/h.

During the combustion process, not all the chemical energy of fuel has been released. The analysis of the energy utilization that is represented by the combustion efficiency, namely, the fraction that is burned compared to that which is supplied, is calculated using the following [14]:

$$\eta_{\text{comp}} = \left( 1 - \frac{\sum_{i=1}^n x_i Q_{\text{LHV}i}}{Q_{\text{LHVfuel}}} \right) \cdot 100\%, \quad (3)$$

where  $x_i$  and  $Q_{\text{LHV}i}$  represent the mass fractions and lower heating values (LHV) of HC, CO, and hydrogen ( $\text{H}_2$ ), respectively. For this study,  $Q_{\text{LHVHC}}$  has been treated equal to  $Q_{\text{LHVfuel}}$ .

Combustion stability was expressed by the coefficient of variability (COV) of IMEP, and a value of 5% was thought to be an acceptable limit for this type of engine. The COV of IMEP was defined by the following:

$$\text{COV}_{\text{IMEP}} = \frac{1}{\text{IMEP}_{\text{mean}}} \sqrt{\frac{\sum_{i=1}^N (\text{IMEP}_i - \text{IMEP}_{\text{mean}})^2}{N - 1}}. \quad (4)$$

**2.3. Fuel.** Commercially available 93 RON gasoline was used for all engine tests. Since the high pressure pump and injector were originally designed to operate with diesel fuel, a lubricity agent (Afton H4140 [15]) of 1000 ppm was added to gasoline fuel to avoid failure of the common-rail injection system. The physical and chemical properties of H4140 lubricity agent were listed in Table 2.

TABLE 2: Physical and chemical properties of H4140 lubricity agent.

Physical form	Liquid
Color	Amber (shallow)
Density (kg/m <sup>3</sup> )	0.91
Solubility	Insoluble in cold water only
Viscosity (cSt@40°C)	17
Flash point (°C)	100 (closed cup)

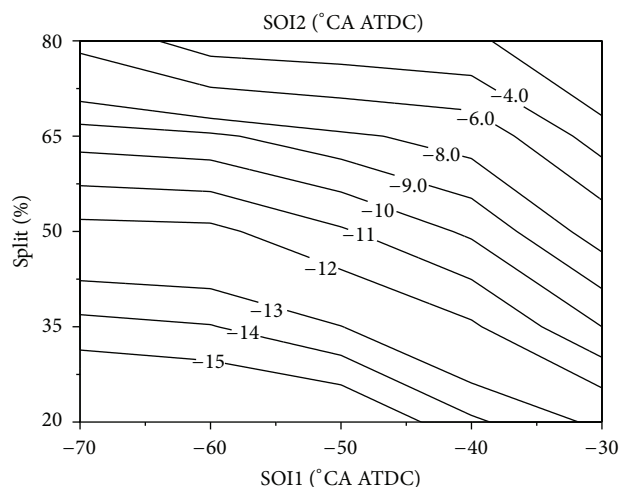


FIGURE 2: SOI2 as a function of SOI1 and split percentage; CA50 set at 10°CA ATDC.

### 3. Results

**3.1. SOI1 and Split Percentage Sweeping.** The major parameters affecting gasoline autoignition considered herein include SOI1 and split percentage. Thus, a sweep in SOI1 and split percentage had firstly been conducted to seek for optimized engine performance and emissions. In this section, the experiments were carried out for the load of 0.9 MPa IMEP (fuelling rate of 50 mg/cycle) at an engine speed of 1500 rpm. SOI1 was altered from -30 to -70°CA after top dead center (ATDC) with an interval of 15°CA and fuel split percentage from 20% to 80% in 10% intervals, where the remaining fuel was injected in the following injection event. Intake pressure and temperature were raised sufficiently to 220 kPa abs. and 323 K, respectively, for stable combustion. A baseline EGR level of 45% was used to avoid combustion reactions during the early stage of the compression stroke. Since the cone angle of the injector is as large as 150°, an appropriately lower injection pressure of 40 MPa was applied to reduce spray penetration, avoiding fuel wall-impingement and entering into the crevice volume. During the SOI1 and split percentage sweeping, the combustion phase of 50% accumulative heat release (CA50) was maintained at 10°CA ATDC, for the efficient combustion coupled with acceptable pressure rise rate. Since EGR rate was kept constant during the experiments, CA50 was mainly controlled by start of the second injection (SOI2).

The contour plot in Figure 2 clearly shows the SOI2 as a function of SOI1 and split percentage to keep CA50 fixed.

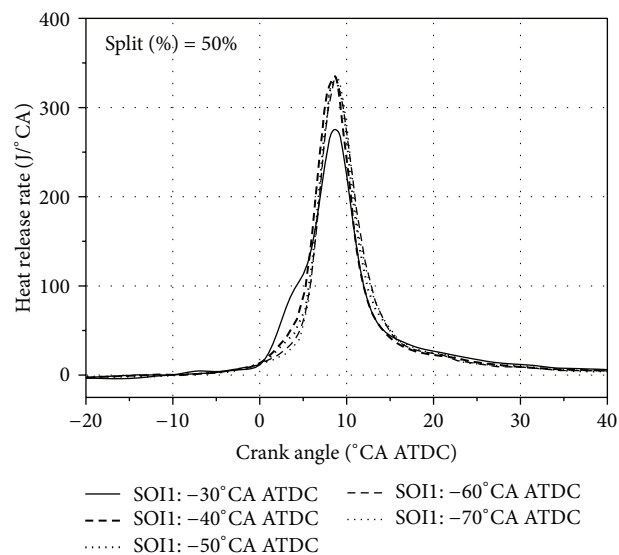


FIGURE 3: Heat release profile as a function of SOI1; split percentage set at 50%.

When SOI1 is advanced, the split fuel and air mixture get even leaner locally and its reactivity is weakened as a consequence, so SOI2 has to be put forward. With the increase of fuel amount in the first injection, the richer premixed charge with enhanced reaction activity has shown the potential to advance the combustion process, so SOI2 has to be delayed for the fixed CA50. It can therefore be concluded that SOI2 should be put forward along with the earlier SOI1 and lower split percentage and retarded closer to TDC otherwise.

Figure 3 presents the effect of SOI1 on heat release profiles while the split percentage is kept at 50%. In the multi-injection strategy in PCCI concept fuelled with diesel, the pilot fuel with good autoignition property generally occurs to combustion during the compression stroke, forming the heat release process of pilot fuel, which reduces the ignition delay and premixed combustion of the main injection, resulting in lower PRR and noise but higher soot level and fuel economy deterioration. Thus, on an energy basis, the pilot fuel is always kept to less than 25% of the total fuel [16]. Based on the points discussed above, for the double-injection strategy in gasoline LTC, large amount of EGR is necessary to prevent premature autoignition of the split fuel, and no obvious heat release process is observed before the total fuel is injected into cylinder as a consequence. The following injection event forms a significant stratification of the gasoline vapor and ignites the premixed charge by the split fuel and air mixing, so a single-peak heat release is observed. With SOI1 fixed at -30°CA ATDC, the combustion reaction occurs at an earlier stage, which leads to a slight decrease in peak HRR, as well as a longer combustion duration. The advancement of SOI1 renders better mixing and produces a more uniform mixture of the split fuel and air, whereas the heat release profiles are almost unchanged, which suggests that the effect of mixing time scale on premixed charge is weakened after a period of sufficient mixing.

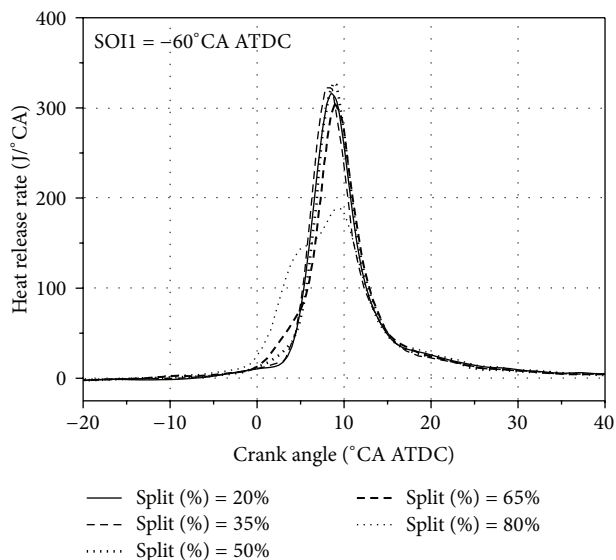


FIGURE 4: Heat release profile as a function of split percentage; SOI1 set at  $-60^{\circ}\text{CA ATDC}$ .

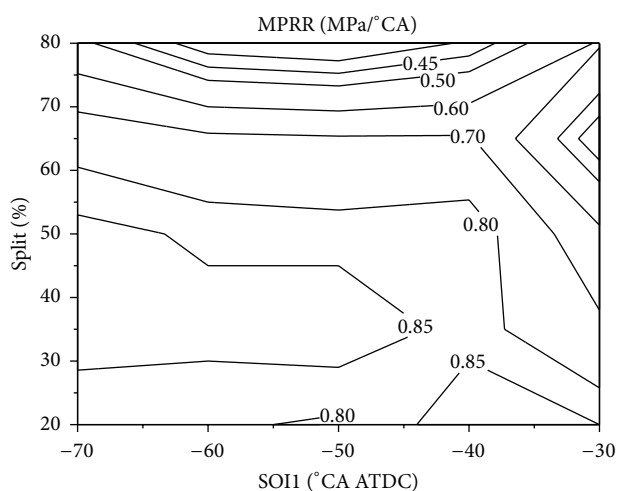


FIGURE 5: MPRR as a function of SOI1 and split percentage.

Figure 4 compares the heat release profiles of various split percentages with SOI1 fixed at  $-60^{\circ}\text{CA ATDC}$ . A single-peak heat release process is observed and remains unaffected with the split percentage ranged from 20% to 50% for the reaction of the lean mixture from split fuel suppressed by EGR. As split percentage reaches 65%, the equivalence ratio of the premixed charge is up to 0.3, which is so reactive that some of the premixed charge occurs to be compressed-ignited before the main combustion process has happened; thereby significant changes are emerging in the heat release profiles. As the fuel split percentage is further increased to 80%, SOC is put forward obviously and a prominent double-peak heat release is noticed, while the equivalence ratio of premixed charge arrives at 0.37, so a smooth combustion process is achieved consequently.

MPRR for various SOI1s and split percentages are given in Figure 5. Under the single-injection case, fuel and air are

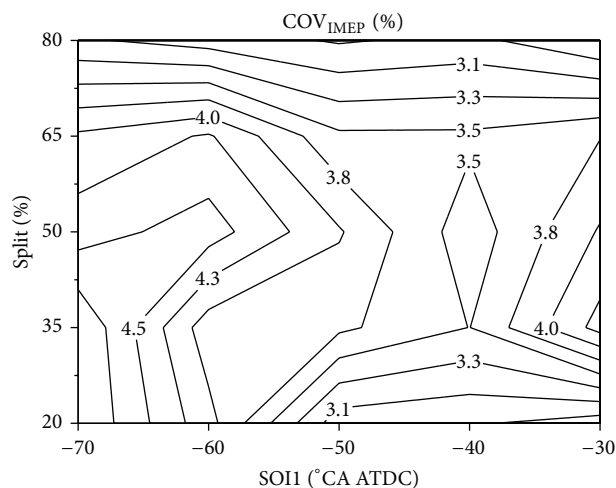


FIGURE 6:  $\text{COV}_{\text{IMEP}}$  as a function of SOI1 and split percentage.

well premixed prior to combustion, whereas there is less time interval between end of the second injection event and SOC with double-injection strategy, resulting in mixture stratification. For this reason, the burning rate is greatly alleviated and instantaneous HRR is reduced by the partial overlap of the second injection and combustion. So it is figured out that the region with MPRR below the threshold value of engine knock is pretty broad. Moreover, the increase in split percentage helps improve the fuel stratification. However, the earliness of the first injection provides more time interval for uniform mixing of fuel with air, which is supposed to play a more important role in MPRR as compared to SOI1. Nevertheless, the mixture stratification may also be weakened by excessively low fuel quantity in the second injection; namely, the split fuel accounts for most of the total fuel, resulting in higher MPRR as well.

The influence of SOI1 and split percentage on coefficient of variation of IMEP ( $\text{COV}_{\text{IMEP}}$ ) is presented in Figure 6. Compared with single-injection strategy, the combustion stability of the double-injection strategy, indicated by  $\text{COV}_{\text{IMEP}}$ , declines apparently in terms of the lean mixture caused by the first injection but still within the stable combustion range. Clearly, the lower  $\text{COV}_{\text{IMEP}}$  is observed in the regions with higher split percentage and the combination of lower split percentage and later SOI1, which can be attributed to the following reasons: as split percentage exceeds 65%, the equivalence ratio of the premixed charge is sufficient to initiate combustion reaction before the following injection event as mentioned previously;  $\text{COV}_{\text{IMEP}}$  becomes less sensitive to SOI1. On the other hand, with split percentage less than 65%, the ignition delay period for the split fuel is so long that the lean mixture is more likely to be disturbed by the in-cylinder airflow with advanced SOI1, thereby increasing cycle-to-cycle variations. The maximum  $\text{COV}_{\text{IMEP}}$  appears at the regions with earlier SOI1 and lower split percentage, which delivers superior MPRR level accordingly. Therefore, from the view of combustion control, applying higher split percentage has the capability of achieving simultaneously

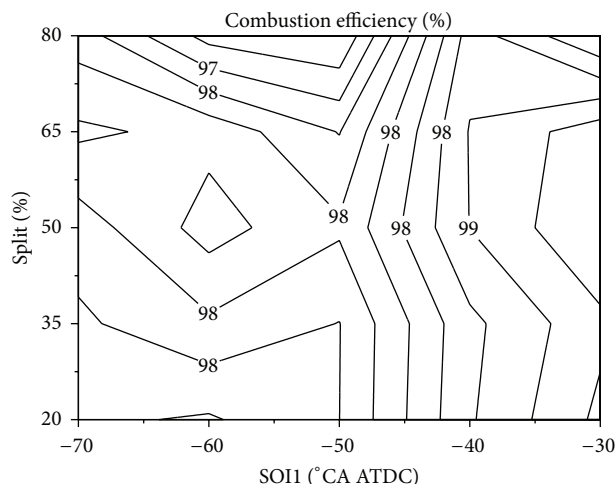


FIGURE 7: Combustion efficiency as a function of SOI1 and split percentage.

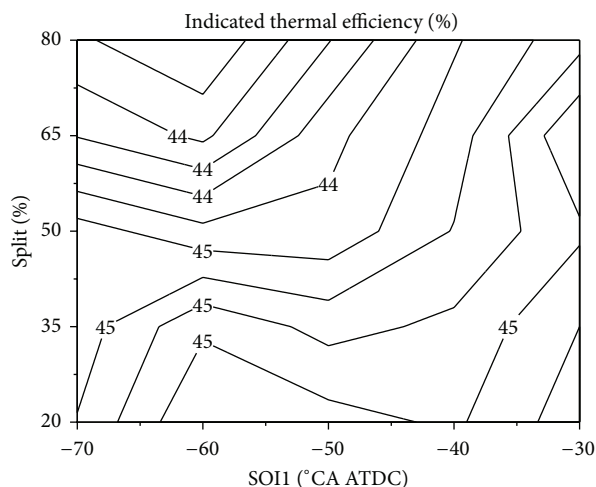


FIGURE 8: Indicated thermal efficiency as a function of SOI1 and split percentage.

lower MPRR and  $COV_{IMEP}$ , which are the indications of the successful operation range expansion of gasoline LTC.

Figure 7 shows the effects of SOI1 and split percentage on combustion efficiency. Overall, the flame quenching in lean premixed charge resulting from advancing SOI1 usually elevates the level of incomplete combustion products to a certain degree, which typically leads to a slight decrease in combustion efficiency. In addition, with the increase of split percentage, the combustion efficiency is reduced further. The detailed relationship between injection parameters and emissions will be discussed in the next section. Owing to the fixed CA50, approximately the same indicated thermal efficiencies under the operation condition are attained, basically between 44% and 45%, while suffering a little from the lower combustion efficiency in the region with earlier SOI1 and higher split percentage, as shown in Figure 8.

The normalized indicated specific  $NO_x$ , soot, CO, and THC emissions for various SOI1 and split percentage combinations using double-injection are given in Figures 9(a), 9(b), 9(c), and 9(d), respectively. From Figure 9(a), generally more fuel in the first injection means less  $NO_x$  emission, so it is clear that the regions with  $NO_x$  emission below 0.4 g/kWh are fairly broad under the test condition. Based on the previous analysis, the reduction of  $NO_x$  is mainly due to the locally lower combustion temperature of the lean mixture resulting from the first fuel injection. On the other hand, SOI1 has a relatively small impact on  $NO_x$  emission, which exactly corresponds to the previous HRR results. Therefore, the amount of the first injection plays a key role in subduing  $NO_x$  emission.

As seen in Figure 9(b), with the advancement of the first injection, soot emission declines gradually due to the enhanced premixing of the split fuel with air, while an increase tendency is observed with more fuel in the first injection. This is mainly because the earliness of SOI1 leads to serious fuel wall-impingement, and the fuel may stick to the engine parts, for example, cylinder wall and piston head, forming an oil film, where more particulates are emitted from the combustion with extremely high equivalence ratio. Meanwhile, in order to keep CA50 fixed, SOI2 is closer to TDC with higher fuel split percentage, thereby mixing period of the second injection is not sufficient; thus the increased diffusion combustion delivers a higher local equivalence ratio, which also leads to soot decortication. Therefore, in order to obtain ideal soot level, the fuelling strategy with the combination of earlier SOI1 and lower split percentage should be employed. Nevertheless, considering the previous results, the regions emitting lower soot emission exactly correspond to those generating higher MPRR and  $COV_{IMEP}$ . Therefore, it is stated that the in-cylinder charge stratification to some extent is necessary for alleviating burning rate, while there could be a price to pay in terms of soot emission. Namely, there exists a trade-off relationship between MPRR and soot with double-injection strategy in the load expansion of gasoline LTC.

As pointed out in Figure 9(c), the relationship between SOI1 and CO emission is dramatically different divided by SOI1 of  $-50^\circ CA$  ATDC. If SOI1 is located after  $-50^\circ CA$  ATDC, the split fuel undergoes longer ignition delay period prior to SOC with SOI1 advancing, so the local mixture gets even leaner, resulting in lower combustion temperature that proved to be an obstacle for the conversion of CO to  $CO_2$ . Therefore, CO emission is strongly influenced by SOI1 but largely unaffected by split percentage. On the other hand, the phenomena become much more complicated. With SOI1 advanced ahead of  $-50^\circ CA$  ATDC, the minimum value of CO emission is obtained with the split percentage of about 50%, while CO emission is increased whether the split percentage is higher or lower. As split percentage exceeds 50%, the locally leaner mixture cannot generate sufficient temperature for the oxidation of CO. Besides, the SOI2 has to be put forward to keep CA50 fixed as a result of the low split percentage, which also decreases the local equivalence ratio. These two factors combined together result in the special distribution of CO emission.

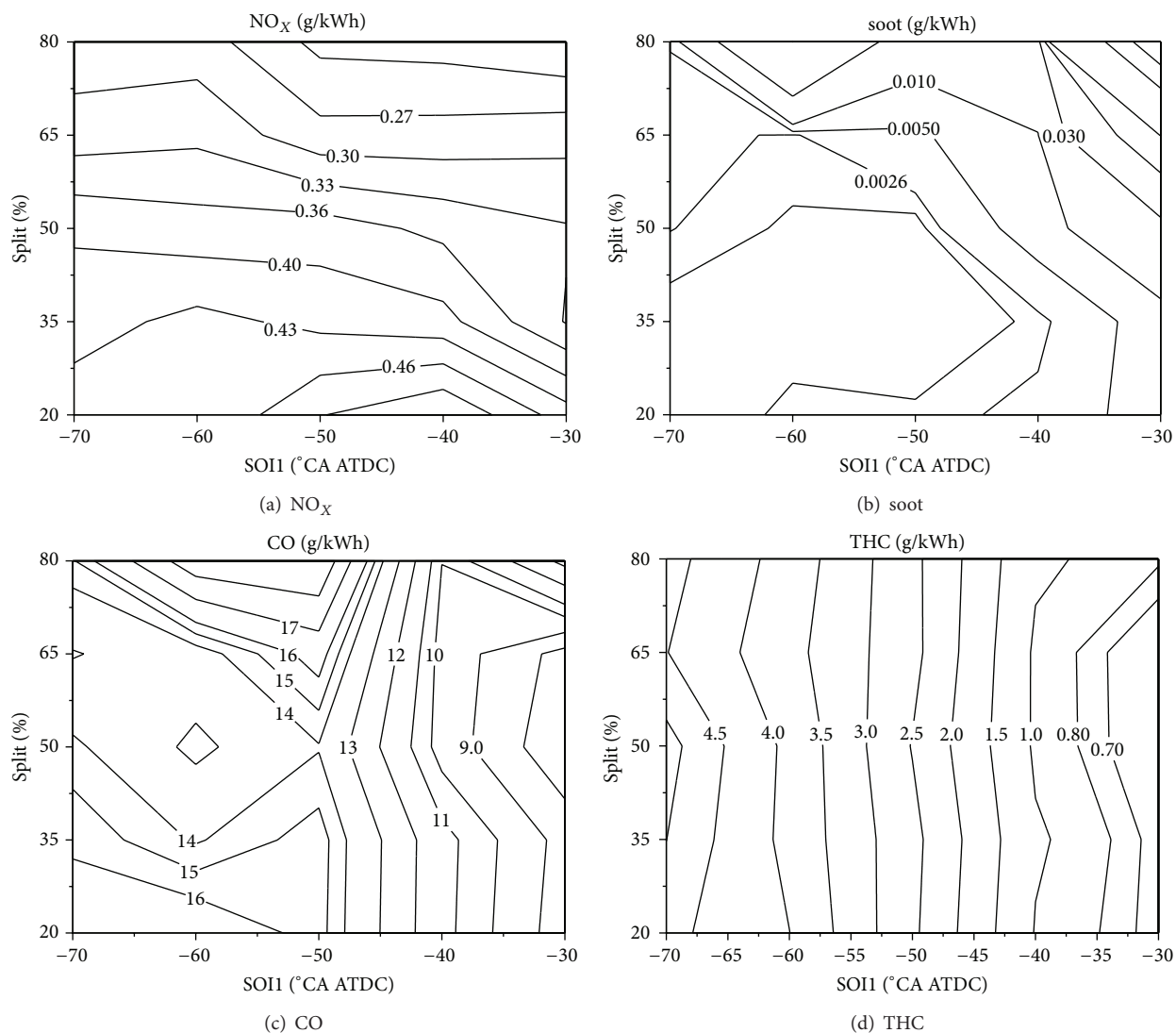


FIGURE 9: Emissions as a function of SOI1 and split percentage.

As Figure 9(d) shows, THC emitted from the double-injection strategy depends monotonically upon SOI1 in general. By applying earlier split injection under the running condition previously described, the spray penetration is increased due to the lower in-cylinder gas densities early in the compression stroke, so the split fuel is likely to cause serious spray impingement on combustion chamber wall surface, or enters into the crevice volume. Thus, gasoline LTC with double-injection strategy produces more THC with earlier SOI1 mainly due to partial flame quenching near cylinder wall, or unburned HC remains in the crevice volume and then is released during the exhaust stroke consequently. Meanwhile, the distributions of CO and THC emissions fully illustrate the change of combustion efficiency with SOI1 and split percentage as well.

**3.2. The High Load Performance for Single- and Double-Injection Strategies.** Based on the previous results, it was decided to investigate the capability of operating range

expansion of the double-injection strategy, while the experiment performed with single-injection strategy had been added as a reference. Euro VI emission regulation and engine design were adequately considered to determine the criteria. The values of  $\text{NO}_x$  and soot emissions were both within the Euro VI regulation. The limits of MPRR and maximum cylinder pressure ( $P_{\max}$ ) were set to  $1.2 \text{ MPa}/^\circ\text{CA}$  and  $16 \text{ MPa}$ , respectively, preventing mechanical damage to the test engine. In addition, the  $\text{COV}_{\text{IMEP}}$  of each test point should be less than 5% for stable combustion. During the experiments, the fuel mass was gradually increased until one or more of the following criteria were violated.

- (i)  $\text{NO}_x < 0.4 \text{ g/kWh}$ ;
- (ii) soot  $< 0.01 \text{ g/kWh}$ ;
- (iii)  $\text{MPRR} < 1.2 \text{ MPa}/^\circ\text{CA}$ ;
- (iv)  $\text{COV}_{\text{IMEP}} < 5\%$ ;
- (v)  $P_{\max} < 16 \text{ MPa}$ .

TABLE 3: Parameters of maximum load for different injection strategies.

Injection strategies	Double	Single
SOI1 ( $^{\circ}$ CA ATDC)	-43	—
SOI2 ( $^{\circ}$ CA ATDC)	-23.5	-27.3
Split percentage	30%	—
CA50 ( $^{\circ}$ CA ATDC)	10	10
EGR	45%	45%
Injection pressure (MPa)	50	50
Indicated thermal efficiency	44.1%	44.6%
Combustion efficiency	97.3%	98.4%
IMEP (MPa)	1.204	1.11
MPRR (MPa/ $^{\circ}$ CA)	1.23	1.18
$P_{\max}$ (MPa)	12.84	12.66
NO <sub>x</sub> (g/kWh)	0.17	0.32
soot (g/kWh)	0.98	0.76
CO (g/kWh)	1.80	1.10
THC (g/kWh)	1.16	0.40

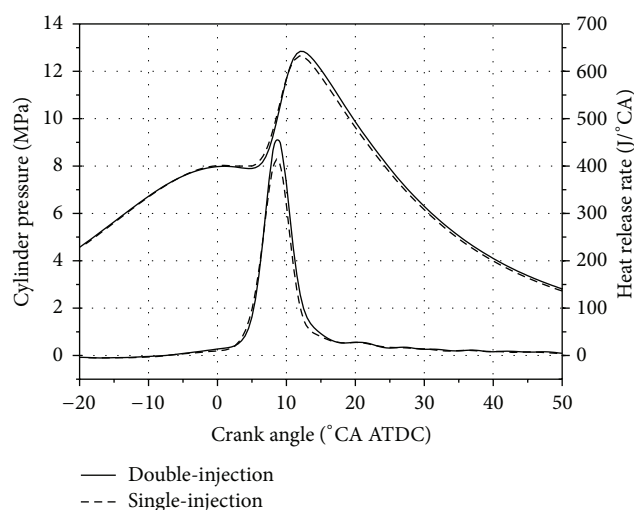


FIGURE 10: Cylinder pressure and heat release profiles of single- and double-injection strategies.

As mentioned in the previous section, the combination of advanced SOI1 and increased split percentage often generates unacceptable MPRR as well as soot deterioration. These two key factors had to be taken into account carefully during the load expansion, while maintaining relatively high combustion efficiency. Thus, the strategy with later SOI1 coupled with lower split percentage was applied for better comprehensive performance; the first injection was placed at  $-43^{\circ}$ CA ATDC with a split percentage of 30%. During the process of operation range expansion, the combustion is configured to provide a CA50 of approximately  $10^{\circ}$ CA ATDC through adjusting injection timings. Further details of the test condition are documented in Table 3.

Figure 10 compares the cylinder pressure and heat release profiles of the single- and double-injection strategies. They both exhibit single-peak heat release pattern under the test

condition. The original engine equipped with a selective catalytic reduction (SCR) exhaust catalyst is enough to approach Euro IV emission standard even at the full load with IMEP of 1.8 MPa. In the effort of optimizing injection parameters, the maximum IMEP of gasoline LTC is extended from 1.11 MPa to 1.204 MPa as figured in Table 3. This indicates that applying fuel double-injection strategy is totally feasible to extend operation range covering the low and medium load conditions commonly used, along with NO<sub>x</sub> and soot levels below Euro VI emission standard without posttreatment system. But the combustion efficiency is slightly decreased because of split injection, and consequently the indicated thermal efficiency declines to some extent. Through the enhanced mixture stratification in the double-injection strategy, MPRR can be held within acceptable level and  $P_{\max}$  is far below the engine design limit.

In the aspect of main emissions, NO<sub>x</sub> emission of the double-injection strategy is further reduced by approximately 50% due to the leaner mixture from split fuel as compared to the single-injection case. It is suggested that NO<sub>x</sub> emission could be well controlled by either the single- or double-injection strategy with sufficient boost and EGR. The fuel double-injection delivers slightly higher soot emission, which is mainly attributed to partial overlap between the second injection and combustion under the parameter settings. Furthermore, as shown clearly in Table 3, the increase of IMEP is limited due to the violation of soot criteria rather than others with increasing total fuel mass. Therefore, similar to MPRR, soot emission is also turned out to be a major factor determining the operation range, and they are related in a trade-off relationship as discussed previously in the double-injection strategy of gasoline LTC. Not surprisingly, the double-injection strategy emits more CO and THC emissions than the single-injection strategy mainly due to the lower in-cylinder combustion temperature and flame quenching near cylinder wall, respectively. The penalty of CO and THC is supposed to be one of the major reasons for the decreased combustion efficiency and indicated thermal efficiency.

## 4. Discussions

Overall, due to the trade-off relationship between MPRR and soot emission, it is difficult to accomplish high-efficiency and clean combustion with pure gasoline over the whole operation range of the original engine. During the optimization study on fuel properties in LTC, researchers have paid much emphasis on bio-fuels, for example, alcohol fuels. Applying alcohol fuels with excessively high oxygen content, and free from aromatic hydrocarbon and sulfur, has been identified to be an effective pathway for solving the issue existing in the load expansion of gasoline LTC due to the remarkable effect of innate oxygen on soot reduction. Butanol, as a competitive alternative fuel, has several advantages over the conventional alcohol alternative fuels for the engine applications [17]. In the four butanol isomers, n-butanol with the unique molecular structure and decomposition reaction shows the least potential to produce polycyclic aromatic hydrocarbons (PAHs), which is usually

considered to be the soot precursor [18]. Therefore, superior engine performance and emissions can be attained using either neat n-butanol [19, 20] or its blend with conventional fossil fuels [21]. However, how to achieve well-organized combustion with n-butanol needs much more studies in the future.

## 5. Conclusions

In the present work, experimental study has been conducted to investigate the effect of fuel injection strategies on the engine performance, emissions, and load expansion capability on a single-cylinder CI engine. The conclusions that can be withdrawn from this paper are as follows.

- (1) With the fixed CA50, the peak HRR is reduced by advancing SOI1 and increasing split percentage.
- (2) Higher indicated thermal efficiency, as well as lower MPRR and  $COV_{IMEP}$ , can be achieved simultaneously with later SOI1 and higher split percentage.
- (3) As split percentage increases,  $NO_x$  emission decreases but soot emission increases. CO and THC emissions are increased by advancing SOI1, resulting in a slight decrease in combustion efficiency.
- (4) Compared with the single-injection strategy, the double-injection strategy enables successful expansion of high-efficiency and clean combustion region, covering the commonly used engine loads. But soot, CO, and THC emissions are increased with the double-injection strategy at high loads, slightly declining the combustion efficiency and indicated thermal efficiency.
- (5) MPRR and soot emission are thought to be the predominant constraints to the load expansion of gasoline LTC, while they are related to their trade-off relationship.

## Nomenclature

ATDC:	After top dead center
CA:	Crank angle
CA50:	The combustion phase of 50% accumulative heat release
CI:	Compression ignition
CO:	Carbon monoxide
$CO_2$ :	Carbon dioxide
COV:	Coefficient of variability
EGR:	Exhaust gas recirculation
FSN:	Filter smoke meter
$H_2$ :	Hydrogen
HCCI:	Homogenous charge compression ignition
HRR:	Heat release rate
IMEP:	Indicated mean effective pressure
LHV:	Lower heating value
LTC:	Low temperature combustion
MPRR:	Maximum pressure rise rate
$NO_x$ :	Nitrogen oxides
PAHs:	Polycyclic aromatic hydrocarbons

PCCI:	Premixed charge compression ignition
PM:	Particle matter
PPC:	Partially premixed combustion
RON:	Research octane number
rpm:	Revolutions per minute
SCR:	Selective catalytic reduction
SOC:	Start of the combustion
SOI1:	Start of the first injection
SOI2:	Start of the second injection
THC:	Total hydrocarbon.

## Conflict of Interests

The authors declare that there is no conflict of interests regarding the publication of this paper.

## Acknowledgments

The research is sponsored by Natural Science Foundation of China through the project of Outstanding Young Scholarship Award (Grant no. 51125026) and Natural Science Foundation of China through its project (Grant no. 51176140).

## References

- [1] M. Yao, Z. Zheng, and H. Liu, "Progress and recent trends in homogeneous charge compression ignition (HCCI) engines," *Progress in Energy and Combustion Science*, vol. 35, no. 5, pp. 398–437, 2009.
- [2] W. L. Hardy and R. D. Reitz, "A study of the effects of high EGR, high equivalence ratio, and mixing time on emissions levels in a heavy-duty diesel engine for PCCI combustion," SAE Paper 2006-01-0026, 2006.
- [3] M. Alriksson, T. Rente, and I. Denbratt, "Low soot, low  $NO_x$  in a heavy duty diesel engine using high levels of EGR," SAE Paper 2005-01-3836, 2005.
- [4] S. Kook, C. Bae, P. C. Miles, D. Choi, and L. M. Pickett, "The influence of charge dilution and injection timing on low-temperature diesel combustion and emissions," SAE Paper 2005-01-3837, 2005.
- [5] D. Turner, G. Tian, and H. Xu, "An experimental study of diesel combustion in a direct injection engine," SAE Paper 2009-01-1101, 2009.
- [6] A. Weall and N. Collings, "Investigation into partially premixed combustion in a light-duty multi-cylinder diesel engine fuelled with a mixture of gasoline and diesel," SAE Paper 2007-01-4058, 2007.
- [7] B. Johansson, "High-load partially premixed combustion in a heavy-duty diesel engine," in *Proceedings of the Directions in Engine Efficiency and Emissions Research Conference (DEER '05)*, 2005.
- [8] V. Manente, B. Johansson, and W. Cannella, "Gasoline partially premixed combustion, the future of internal combustion engines?" *International Journal of Engine Research*, vol. 12, no. 3, pp. 194–208, 2011.
- [9] L. Hildingsson, G. Kalghatgi, N. Tait, B. Johansson, and A. Harrison, "Fuel octane effects in the partially premixed combustion regime in compression ignition engines," SAE Paper 2009-01-2648, 2009.

- [10] G. T. Kalghatgi, P. Risberg, and H.-E. Ångström, "Partially pre-mixed auto-ignition of gasoline to attain low smoke and low NOX at high load in a compression ignition engine and comparison with a diesel fuel," SAE Paper 2007-01-0006, 2007.
- [11] R. Hanson, D. Splitter, and R. Reitz, "Operating a heavy-duty direct-injection compression-ignition engine with gasoline for low emissions," SAE Paper 2009-01-1442, 2009.
- [12] S. Ciatti and S. N. Subramanian, "An experimental investigation of low-octane gasoline in diesel engines," *Journal of Engineering for Gas Turbines and Power*, vol. 133, no. 9, Article ID 092802, 2011.
- [13] H. Yang, S. Shuai, Z. Wang, and J. Wang, "Fuel octane effects on gasoline multiple premixed compression ignition (MPCI) mode," *Fuel*, vol. 103, pp. 373–379, 2013.
- [14] J. B. Heywood, *Internal Combustion Engine Fundamentals*, McGraw-Hill, New York, NY, USA, 1988.
- [15] Afton Chemical Corporation, *HiTEC 4140 Performance Additive*, 2009.
- [16] W. D. Ojeda, P. Zoldak, R. Espinosa, and R. Kumar, "Development of a fuel injection strategy for partially premixed compression ignition combustion," SAE Paper 2009-01-1527, 2009.
- [17] C. Jin, M. Yao, H. Liu, C.-F. F. Lee, and J. Ji, "Progress in the production and application of n-butanol as a biofuel," *Renewable and Sustainable Energy Reviews*, vol. 15, no. 8, pp. 4080–4106, 2011.
- [18] H. Jin, Y. Wang, K. Zhang, H. Guo, and F. Qi, "An experimental study on the formation of polycyclic aromatic hydrocarbons in laminar coflow non-premixed methane/air flames doped with four isomeric butanols," *Proceedings of the Combustion Institute*, vol. 34, no. 1, pp. 779–786, 2013.
- [19] X. Han, M. Zheng, and J. Wang, "Fuel suitability for low temperature combustion in compression ignition engines," *Fuel*, vol. 109, pp. 336–349, 2013.
- [20] M. Zheng, T. Li, and X. Han, "Direct injection of neat n-butanol for enabling clean low temperature combustion in a modern diesel engine," *Fuel*, vol. 142, pp. 28–37, 2015.
- [21] B. Yang, M. Yao, W. K. Cheng, Z. Zheng, and L. Yue, "Regulated and unregulated emissions from a compression ignition engine under low temperature combustion fuelled with gasoline and n-butanol/gasoline blends," *Fuel*, vol. 120, pp. 163–170, 2014.